Investigations of physical processes in polar firn through modeling and field measurements

Christopher Stevens

A dissertation

submitted in partial fulfillment of the

requirements for the degree of

Doctor of Philosophy

University of Washington

2018

Reading Committee:

Ed Waddington, Chair

Howard Conway

Michelle Koutnik

Program Authorized to Offer Degree:

Earth and Space Sciences

University of Washington

Abstract

Investigations of physical processes in polar firn through modeling and field measurements

Christopher Stevens

Chair of the Supervisory Committee:
Professor Ed Waddington
Department of Earth and Space Sciences

Evolution of firn on the polar ice sheets is important for several applications in glaciology, including interpreting climate records from ice cores and correcting ice-sheet-elevation change measurements from altimetry for changes in the amount of air in firn. I have developed the Community Firn Model (CFM), a modular model framework that can simulate numerous physical processes in firn, including densification, air transport, heat diffusion, and grain growth. In this dissertation, I use the CFM and measurements from Greenland to investigate firn densification, gas transport in firn, and uncertainty within firn models.

First, I have coupled a firn-air model to a firn-densification model. I use this new model to investigate air transport in the lock-in zone and show that the lock-in zone could be created by impermeable layers, or it could be caused by differences between the advective and diffusive

timescales of air transport. I also show that δ^{15}N and δ^{40}Ar data from the GISP2 ice core can be better explained than previously by including transient firn thickening during rapid climate-change events. Additionally, I explore the effects that impermeable layers in the firn have on gas records. I conclude that including transient firn evolution is essential to modeling gas transport correctly during climate changes, but limited knowledge of the microstructure of firn limits our ability to model firn-air transport accurately in the past.

Next, I intercompare 11 firn-densification models and test their sensitivities to initial and boundary conditions at Summit, Greenland. I show that there is no 'best' firn model, and that there are numerous sources of uncertainty in firn models. The uncertainty in predicting the depth-integrated porosity of the firn is ~10%, and the uncertainty in predicting the depth and age of the firn-ice transition is greater than 10%. Uncertainties in surface boundary conditions, including the climate forcing and surface density, as well as model parameterizations contribute to model uncertainties.

Finally, I present firn-compaction data from Greenland and compare firn-densification-model predictions to those data. I use the firn-compaction data to derive a new firn-densification equation for Summit. I show that performance of firn densification models varies by site and by depth in the firn. At Summit, several models can predict the compaction rate to within 10%, but at EastGRIP, all models have an RMS error greater than 20%. My results indicate that the models do not yet represent physical processes correctly; I identify future research that is needed to help improve the models.

TABLE OF CONTENTS

LIST OF FIGURES

LIST OF TABLES

ACKNOWLEDGEMENTS

I have been fortunate to have been surrounded by many wonderful people during my time as a graduate student.

I am grateful to my primary advisor, Ed Waddington, for his continued support for the past eight years. Besides being a brilliant scientist, he is also one of the most caring individuals I have ever met. I think every graduate student goes through a period when s/he is ready to quit, and Ed is remarkably good at spinning that energy so that somehow you walk out of his office excited to explore some new idea. I must in particular thank Ed for allowing me to chart my own journey, whether that be taking months off to canoe in the Yukon or pursuing side projects that were fun research but not necessarily pushing me to graduate sooner.

Countless thanks to my second advisor, Twit Conway, as well. Twit has brought me along to Antarctica numerous times, so I am eternally grateful to him for those experiences. Working with him has been an absolute pleasure. Twit has a remarkable way of having serious scientific conversations without seeming too serious at all and making you feel like your thoughts are valuable. His abilities and work ethic in the field (and out of it too) are inspiring.

Thank you to Michelle Koutnik for serving me well as a committee member and for many great conversations about research (and life). The best word I can think of to describe Michelle's insights is 'wise'.

Thank you to Becky Alexander for serving as my GSR on my committee.

I have been lucky to participate in six field campaigns, and many thanks to all of the folks who I worked side-by-side with in sometimes-terrible conditions, and also who happily shared their whiskey and stories each night when the work was done: Twit Conway, Michelle Koutnik,

Maurice Conway, Paul Winberry, David Lilien, David Clemens-Sewell, Elizabeth Morton, Mike Waszkiewicz, Mike MacFerrin, Achim Heilig, Baptiste Vandecrux, Tasha Snow, Aleah Sommers, Liam Colgan, Babis Charalampidis, Shane Grigsby, and Darren Hill.

The graduate student cohort in ESS has made the last 8 years much more fun than it would have been otherwise. Officemates David Lilien, Dave Shean, Emily Newsom, Kristin Poinar, Laura Kerhl, Aurora Burd, Taryn Black, Annika Horlings, Brita Horlings, and very occasionally Twila Moon and Brooke Medley made each day much more fun. The Kinderegg crew, David Lilien, Todd Anderson, Julia Kelson, and Shelley Chestler, in particular made the last 2 years extra fun.

Thanks also to the great community of friends outside of UW and ESS that I am fortunate to have: I moved to Seattle knowing a few people, and those people helped me gain a network of lifelong friends that have helped me make Seattle a home and with whom I have shared unforgettable experiences: Eric Lamanna, Tom Lamanna, Bridget Tanner, Ben Lee, Tyler Thirloway, Jess Castello, Andrew Marsters, Dylan LeValley, and Ben Landsman.

My family has always been very supportive of me, and I thank them for continuing that through my time here. Having Tucker and Sara and Adeline and Ingrid down the road meant the world to me, and though my parents live far away, I thank them for visiting often and helping me along through this journey.

Finally, so many thanks and more to Shelley, without whom I would have probably taken another two years to finish.

DEDICATION

To my parents, Don and Della.

Chapter 1. INTRODUCTION

I began my journey as a glaciologist before I could speak in full sentences. My dad would build snow caves for my brother and me, and I would just stand in them contentedly marveling as the time passed. Eventually, after many years investigating the ideal density of snow for skiing, I found myself as a graduate student at the University of Washington, and so perhaps it is appropriate that I ended up studying and becoming an expert on firn.

The Oxford English Dictionary defines firn as "snow above the glaciers which is partly consolidated by alternate thawing and freezing, but has not yet become glacier-ice", but in the glaciological sense this is an incomplete definition. In the accumulation zone of glaciers and ice sheets, more snow falls each year than melts away. The material near the surface, that has "not changed much since it fell" (Cuffey and Paterson, 2010 p. 11) is referred to as snow. Snow that has begun to transform into glacial ice is called firn. On glaciers and ice sheets where there is melt the transition from snow to firn is clearly defined: firn is the snow that has lasted through a melt season, and this transition is easy to find in a snow pit. In areas of the ice sheets that do not experience melt, this transition is not so clear. But, for many of the questions of interest to glaciologists this delineation is not so important as the mechanisms that are at work to transform the material to ice, which almost certainly operate on a continuum, so perhaps it appropriate to have a slightly fuzzy definition of firn. In this work, I generally use the term firn broadly to include snow. The transition from firn to ice is easier to define: when all of the pore space in the firn becomes sealed from the atmosphere, which typically occurs at a density around 830 kg m^{-3}, the firn has become glacial ice.

My research during my graduate tenure has focused on firn, and more specifically what firn models can (and cannot) tell us. I have been able to work on problems spanning the breadth

of firn-model applications: my first graduate work was with the ice-core community, and more recent work has been with the ice-sheet mass balance community. This experience has given me a unique expertise in the glaciological community. I do not pretend to be a world leader in using delta-age calculations to interpret ice cores, nor in producing estimates of firn thickness change for mass balance calculations, but I can confidently say that I am a firn-model expert. My expertise spans the disciplines mentioned above, and this expertise allows me to understand the applications and limitations of firn models better than I would have had my research been focused in one discipline. My combination of experience and skills has positioned me as a leader in the area of modeling firn properties for either group. My expertise extends beyond being able to produce firn model outputs; throughout my research I have used nearly all of the firn-densification models published since 1980. Through this work I have become a leader in knowing the nuances of each firn-densification model, and much of my work has focused on assessing the uncertainty in firn-model outputs.

I have been fortunate to participate in numerous field campaigns during my graduate tenure, which has also made me a leader in measuring firn properties, especially firn compaction, in the field. Some of my field-work knowledge is practical (e.g. efficiently measuring density on a core), learned through making many mistakes and occasionally getting things right. But, the combination of modeling and field work positions me uniquely in the glaciological community. I know of what data are needed to improve firn models, and I also know how to collect those data.

Collectively, the work I present in this dissertation is a significant contribution to the glaciological community. The CFM has been adopted by several research groups internationally in both the ice core and mass balance communities, including Lancaster University and the Centre for Ice and Climate at the University of Copenhagen, and I have been invited to collaborate on

projects with researchers at numerous institutions, including the University of Colorado and GEUS in Denmark.

1.1 MOTIVATION

Knowledge of the physics of firn evolution is important for two primary applications in glaciology. First, mass loss of the polar ice sheets is a significant contributor to sea-level rise, but the magnitude of this contribution is still uncertain (Shepherd and others, 2012; Stocker and others, 2013). Satellite- and airborne-altimetry methods precisely measure surface elevation changes of the ice sheets. However, altimetry methods measure volume change, and a firn-densification model is required to convert surface-elevation change to mass change (Reeh, 2008). Estimating the sea-level rise contribution from an ice sheet depends on having an accurate firn-densification model to calculate changes in firn air content over time.

Calculating the ice sheets' mass balance also requires knowledge of the amount of surface melt and the fate of the meltwater. This is especially important in Greenland, where both the areal melt extent and number of days with melt have increased over the last decades (Mernild and others, 2011). Harper and others (2012) suggested that the firn could buffer the additional melt by acting as a sponge-like reservoir, thereby delaying the associated sea-level rise. However, Machguth and others (2016), found thick ice layers in the high-melt areas of the accumulation zone; they posited that these ice layers were spatially extensive enough to prevent meltwater percolation into deep firn, and that as a result, melt would therefore run off into the oceans. Firn models are now being adapted to include meltwater percolation, refreezing, and runoff.

The second primary application of firn-densification models is to aid in the interpretation of paleoclimate records from ice cores. Understanding the Earth's climate system and making future climate predictions relies on knowing how climate has changed in the past; climate records

from ice cores are an important data set for investigating these historical changes. The bubbles of air trapped in ice are a direct sample of past atmospheric composition, and stable isotopes of water measured from the ice itself provide a proxy for past temperature. Because young gasses can move relatively freely in the open porosity of the old firn, the gasses that become trapped in a bubble are younger than the ice that holds the bubble; the age difference is called delta age. Accurate calculations of delta age are essential to deduce the chronology of past climate change events (e.g. timing between temperature change and atmospheric CO_2 change). A firn-densification model is used to estimate the ice age (typically hundreds to thousands of years) when bubbles become trapped. A firn-air model is used to estimate the mean age of the gasses in the bubbles (on the order of several decades) as well as the distribution of gas ages. Firn-air models can also be used to predict the thermal and gravitational fractionation of stable isotopes, which can be used as an independent estimate of past firn depth and temperature change (Severinghaus and Brook, 1999).

1.2 BACKGROUND

Interest in firn densification has existed at least since 1931, when Ernst Sorge suggested that the depth-density profile in the dry-snow zone of Greenland is invariant in time (Sorge, 1935). Bader (1954) developed this idea mathematically by showing how an observed change in density with depth can be related to a change in density with time. This treatment of the problem, i.e. the steady-state assumption, has been used numerous times since: many models use measured depth-density profiles to find model coefficients, thus invoking Sorge's Law.

Firn is broadly divided into two zones based on the dominant mechanisms of densification. In zone 1, where densities are less than 550 kg m^{-3}, the primary mechanism is thought to be grain boundary sliding. In zone 2, ranging from 550 kg m^{-3} to the bubble close-off-density (~830 kg m^{-}

^{3}), firn densifies by sintering processes. Numerous works (cf. Blackford, 2007 and references therein) have investigated the physics operating at a microstructural scale.

Morris and Wingham (2014) identified two approaches to modeling firn densification: the microscale approach and the macroscale approach. In the microscale approach, firn densification is considered at the grain scale through descriptions of the microphysics such as grain boundary sliding (Maeno and Ebinuma, 1983; Alley, 1987), dislocation creep (Wilkinson, 1988), and lattice diffusion (Coble, 1970). The model operates at a larger scale by assuming that the properties of a single grain also apply to ice aggregates of many grains. The macroscale approach uses a bulk constitutive relationship that ostensibly encompasses all of the microstructural mechanisms. In this dissertation, I focus on models that take the macroscopic approach.

In 1980, Herron and Langway proposed a model for firn densification based on measured depth-density profiles in Greenland and Antarctica. The model has become something of a benchmark and is still in use today, especially in the ice-core community. They proposed a model form relating the change in density ρ with time t to an Arrhenius term with activation energy Q, the ice density ρ_i, the accumulation rate $\dot{b}$, and a scaling constant k:

$$\frac{d\rho}{dt} = k\, e^{\left(-\frac{Q}{RT}\right)}(\rho_i - \rho)\dot{b}. \tag{1}$$

This basic model form has since been used frequently to develop other firn densification models. To this point, these models include Barnola and others (1991), Li and Zwally (2002, 2004, 2011), Helsen and others (2008), Arthern and others (2010), Ligtenberg and others (2011), Simonsen and others (2013), Morris and Wingham (2014), and Kuipers Munneke and others (2015). I also assume this form for the model I derive in Chapter 4 of this thesis.

Many of these firn-densification models have relied on measured depth-density profiles for calibration, which inherently invokes the steady-state assumption. Predicting firn-thickness

changes in order to interpret ice-sheet mass-balance changes must account for spatial and temporal variability in accumulation rate and temperature. In addition, delta age changes through time as the firn changes with climate. It is not known if models derived using Sorge's Law can be generalized successfully for these transient scenarios without the addition of data collected during transient changes. A central theme to my work presented here is testing firn models' abilities to predict observations from the real world.

1.3 ORGANIZATION

This dissertation is split into six chapters, including this introduction. Broadly, I address questions related to physical processes in polar firn. I approach these questions primarily from a modeling perspective. Central to the work I present in this dissertation is the Community Firn Model (CFM), whose development I spearheaded over the past 8 years. The CFM began as a project motivated by the ice-core community to have open-source firn-densification and firn-air models for delta-age calculation, and it evolved to include features of interest to other fields, such as water-isotope diffusion and meltwater percolation and refreezing. I strived to make the model as modular and user-friendly as possible. A description of the CFM is included as Chapter 5.

In Chapters 2, 3, and 4, I describe three distinct applications of the CFM. Each of these three chapters is in preparation for submission to journals. Chapter 2 describes a coupled firn-densification/firn-air model within the CFM framework and several applications. This is the first time, to my knowledge, that a firn-air model has been coupled to a transient-firn densification model. The main question that I address is: How does transient firn densification affect the gasses trapped in ice? I address this question through model experiments investigating how an impermeable ice lens affects the $\delta^{15}N$ profile in an ice core and how transient firn thickening alters the δ^{15}N and δ^{40}Ar records during rapid climate changes.

Chapter 3 is an extension of a journal article where I am a co-author (Lundin and others, 2017). In that article we compared the responses of nine firn models to synthetic climate changes. In Chapter 3, I investigate the model responses to output from regional climate models at Summit, Greenland. The chapter focuses on the questions: When forced with the same climate data, how well do firn models agree? How sensitive are firn models to initial and boundary conditions?

Chapter 4 features firn observations (density, temperature, and strain rate) from three Greenland field expeditions (2015, 2016, and 2017) that I participated in. I compare those data to model output and use them to derive a firn-densification model for Summit, Greenland. The chapter investigates the question: How well do firn models predict observed compaction rates, temperatures and densities?

Chapter 6 contains a summary, broad conclusions, and outlooks for future research.

Chapter 2. MODELING AIR TRANSPORT IN EVOLVING FIRN

2.1 ABSTRACT

Air trapped in ice cores provides a record of Earth's climate history; past air becomes trapped in bubbles after the air diffuses and advects through the porous and permeable upper layer of an ice sheet known as firn. To this point, models simulating firn-air transport have assumed that the firn is in steady-state. We have coupled a firn-air model to a firn-densification model in order to simulate firn-air transport in conditions when the firn is not in steady state. We present the model and demonstrate its utility in addressing three problems: (1) firn and gas-transport processes that create the lock-in depth; (2) the effect of firn-thickness changes on noble-gas-isotope ratios; and (3) the effect of a non-permeable ice layer on gas concentrations observed in ice cores. Including transient firn evolution is essential to modeling the gas transport correctly during climate changes, but limited knowledge of the microstructure of firn limits our ability to model firn-air transport accurately in the past.

2.2 INTRODUCTION

Ice cores from polar regions have provided an 800,000-year history of the Earth's climate (EPICA members, 2004), and it is likely that future efforts will yield an even-longer record. These records help us to understand past climate and the mechanisms that force past climate change. However, uncertainties in methods used to interpret ice-core records can limit our ability to understand past climate change. One such source of uncertainty is due to modeling densification of firn and diffusion of air through firn, the porous upper layer of ice sheets.

Bubbles of air trapped in ice provide direct measurements of past atmospheric composition. The ice itself provides other information; for instance, water isotopes are a proxy for past

temperature. The air in bubbles is not the same age as the surrounding ice; the difference between the two is called ‘delta age’. An accurate estimate of delta age is essential to constraining timing of past climatic changes and determining causal relationships of those climatic changes.

The age difference between air in bubbles and the surrounding ice is a result of the process of snow transforming into ice. In glaciated regions, snow falls to the ground at densities between about 100 and 300 kg m^{-3} (Cuffey and Paterson, 2010). As more snow falls, older snow is buried and begins to densify. Snow that does not melt or sublimate is called firn. Firn continues to densify due to the increasing overburden stress, and some of the porosity becomes closed, i.e. isolated from the atmosphere and from interconnected pore space. Within the open porosity (i.e. the porosity that is interconnected and connected to the atmosphere), gasses can move relatively freely. At the bubble-close-off (BCO) density, which is typically around 830 kg m^{-3}, all of the porosity is closed and air transport relative to the ice ceases. The firn has become bubbly glacial ice. The BCO depth ranges from ~50 m at relatively warm, relatively low-accumulation sites to ~120 m at cold, high-accumulation sites. The BCO age can range from ~100 years at warm sites to >2000 years at very cold sites. The air that becomes trapped is younger than the ice that it is trapped within because the diffusive timescale for air transport in firn is on the order of decades, which is much shorter than the densification timescale. Knowing the age of both the firn and the air at bubble close-off, as well as the bubble close-off depth, is essential for delta-age calculations and thus for accurate interpretation of ice-core records. One method of estimating these ages is to use a firn-densification model and a firn-air model.

We have coupled a firn-air model to a transient firn-densification model to allow studies of firn-air transport in a firn column whose depth and tortuosity change through time. In this paper we first present the new model and then demonstrate its utility through several model experiments:

in the first, we investigate the properties of the firn that create the lock-in zone; in the second we examine the effects of transient firn thickening on stable isotope fractionation in the firn, and in the third we look at the effect of a downward-moving, non-permeable layer on the gas record.

2.3 FIRN MODELING

2.3.1 Firn-densification models

Numerous models have been developed to simulate the firn-densification process. Other works (e.g. Lundin and others, 2017) discuss these models in detail; here we provide a brief overview. These models often divide the firn into three zones of compaction defined by firn density. Zone 1 spans from the surface (where density is typically ~350 kg m^{-3} in polar regions) to the 550 kg m^{-3} density horizon. Densification in this zone is due primarily to grain boundary sliding. Zone 2 spans from 550 kg m^{-3} to the BCO density, and densification occurs by sintering processes. From the BCO density to the pure ice density, density increases as bubbles are compressed and eventually forced into clathrates. Most firn-densification models are concerned with densification in zone 1 and zone 2, and most have been formulated using measured depth-density profiles to parameterize the physics of the densification process. Because of these parameterizations, most models simulate bulk-depth density profiles but not small-scale processes such as microstructural evolution or layering.

2.3.2 Firn-air models

Atmospheric gasses move through the firn pore space at all depths above bubble close-off. Gas transport in firn is commonly divided into three zones by dominant transport mechanisms (which are different than the three zones of densification). Near the surface is the convective zone, which may be from 0 to ~20 m thick. In this zone, convective mixing due to wind pumping and buoyancy

dominates gas transport and keeps the air well-mixed (Kawamura and others, 2006). Below the convective zone is the diffusive zone, where gas transport is driven primarily by diffusion along chemical-concentration gradients. Additionally, isotopic fractionation occurs in the diffusive zone due to gravitational and thermal effects: heavier isotopes become enriched (i.e. their relative abundance increases) at depth due to gravity and at the cold end of a temperature gradient.

Near the firn-ice transition is the lock-in depth (LID), which has traditionally been defined as the depth at which gravitational fractionation and diffusion effectively cease (Buizert and Severinghaus, 2016). Below the lock-in depth is the lock-in zone (LIZ), which terminates at the BCO depth. Despite the fact that there is no diffusion within the LIZ, there is still open porosity. Recent work by Buizert and Severinghaus (2016) suggested that gasses still flow in the LIZ through dispersion driven by barometric pressure changes.

Firn is also continuously advecting downward, carrying gas with it in the pore space. Near the BCO depth the gas pressure increases as pore space closes. As a result, air advects downward slower than the firn itself; in a Langrangian framework, the air has relative-upward motion.

Numerous firn air models have been developed (see e.g. Buizert and others, 2012) to simulate these physical processes. Unlike the various firn-densification models, which do not have an agreed-upon set of physics, firn-air models solve some variation of the firn-air equation (Severinghaus and Battle, 2006):

$$\frac{DC}{Dt} = \frac{1}{\phi_{op}} \frac{D}{Dz} \left[\phi_{op}(t) D_{eff}(t,z) \left(\frac{dC}{dz} - \frac{\Delta m g}{RT} + \Omega \frac{dT}{dz} \right) \right] + w_{air}(z) \frac{\partial C}{\partial z} \qquad (2.1),$$

where C is the concentration or delta value of a gas species, $\phi_{op}(t)$ is the open porosity, Δm is the isotopic mass difference, T is the temperature, and Ω is the thermal-diffusion sensitivity, $D_{eff}(t,z)$ is the effective diffusivity, and $w_{air}(z)$ is the advection rate of the air within the pore matrix. As porosity of firn decreases, molecules must take a longer and more tortuous path in order to diffuse;

the effective diffusivity accounts for this by scaling the free-air diffusivity, D_{FA}, with the tortuosity, τ, of the firn (Buizert and others, 2012): $D_{eff} = \frac{D_{FA}}{\tau}$. In this work, the term diffusivity is taken to mean effective diffusivity.

Equation 2.1 is written in terms of the total (material) derivative, and so advection air due to downward air of firn is implicit. In a stationary reference frame, Equation 2.1 also includes a firn-advection term.

Commonly, firn-air models are designed to simulate firn-air transport at a particular site for modern day in order to interpret measurements of gas concentrations in the modern firn; for these purposes the effective diffusivity profile is tuned to match measurements using an inverse method (Buizert and others, 2012). If the effective diffusivity is not known, it can be estimated using a parameterization. Several diffusivity parameterizations have been published. These parameterizations determine the diffusivity as a function of either the total or the open porosity.

2.3.3 The Community Firn Model

Previous work considered firn densification and firn-air transport separately from a modeling perspective; that is, firn-air models have assumed steady-state firn depth-density and effective-diffusivity profiles. We have added a firn-air module to the Community Firn Model (CFM; Stevens et al., in prep), which allows us to simulate gas transport while simultaneously modeling evolution of firn depth and density in a transient climate.

The CFM is a modular firn-evolution model framework. It allows users to choose from a variety of firn-densification physics (e.g. Herron and Langway, 1980; Barnola and others, 1991; Goujon and others, 2003; Ligtenberg and others, 2011). The modularity of the model allows the user to choose which physical processes to include in a model run; the options include temperature

evolution, grain growth, water-isotope diffusion, meltwater percolation, and firn-air diffusion. The model is designed so that additional physics can be easily integrated.

The CFM firn-air module solves the firn-air equation (2.1) on a Lagrangian grid, which results in the downward advection of gasses being handled without an additional advection term in Equation 2.1. In this framework, air should be advected upward relative to the downward-moving grid because the densification of the firn increases the air pressure in the open porosity. Previous Lagrangian firn-air models have ignored this effect (Trudinger and others, 1997); the CFM has the option to ignore it or to include it through the description provided by Buizert (2011).

The CFM also allows the user to choose which parameterization for diffusivity to use. As of the time of writing, the CFM includes the diffusivity parameterizations published by Schwander and others (1988), Battle and others (1996), Severinghaus and others (2001), Freitag and others (2002), Witrant and others (2012), and Adolph and Albert (2014).

Modeling the diffusivity and the close-off physics requires knowing the BCO depth. To find the close-off density, the CFM uses the relationship published by Martinerie and others (1992):

$$\bar{\rho}_{co} = \left(\frac{1}{\rho_{ice}} + 6.95 * 10^{-7} T - 4.3 * 10^{-5}\right)^{-1}. \quad (2.2)$$

Bubbles close off over a range of densities (and therefore depths), and Equation 2.2 predicts the mean close-off density (and thus mean close-off porosity ϕ_{co}). The density of full bubble close off, ρ_{CO}, where ϕ_{op} is zero, will be slightly greater than $\bar{\rho}_{co}$, and its depth z_{co} slightly deeper than $z(\bar{\rho}_{co})$.

Equation 2.1 also requires knowing the ϕ_{op}. The CFM uses the parameterization for closed porosity ϕ_{cl} as a function of total porosity ϕ_{tot} presented in Goujon and others (2003):

$$\phi_{cl} = 0.37 * \phi_{tot} \left(\frac{\phi_{tot}}{\phi_{co}}\right)^{-7.6}. \quad (2.3)$$

Finally, the CFM has an option to specify the lock-in depth. In this case, the diffusivity below the specified lock-in depth is set to zero. The lock-in density is determined by subtracting 14 kg m^{-3} from $\bar{\rho}_{co}$ (Blunier and Schwander, 2000).

The CFM does not include certain features that some firn-air models include, such as bubble trapping rate, bubble pressure, total air content, dispersive mixing in the LIZ, and the mean and distribution of gas ages in the closed porosity (Buizert and others, 2012). For now, we assign a gas age of 15 years to the gasses at the lock-in depth. These features will be integrated into future releases of the CFM. Despite these current shortcomings, the CFM's strength is the coupled firn-air firn-densification model, which we demonstrate the utility through several different model experiments described in Sections 3, 4, and 5.

2.4 AIR TRANSPORT AT THE LOCK-IN DEPTH

The physical processes driving gas transport and firn densification in the lock-in zone are not well known. It is surprising perhaps that diffusion and isotopic fractionation cease despite the fact there is still open porosity. This curiosity has led to two hypotheses. First, some research has suggested that the lock-in zone is a result of layering in the firn (e.g. Kobashi and others, 2008; Mitchell and others, 2015). That is, high-density layers become impermeable at shallower depths compared to lower-density layers, thereby effectively restricting air transport between the open pore space in the upper firn and the open pore space deeper than the high-density layer(s). Hence, the depth of the first high-density layer determines the lock-in depth, and the lock-in zone represents the depths between the lock-in depth and the close-off depth. Recent work by Birner and others (2017) using

a 2D firn-air model suggested that layering alone cannot cause isotopic fractionation to cease, but stopping fractionation is possible if pressure-driven dispersion also occurs in concert with layering.

Second, other work has shown that the thickness of the lock-in zone has a positive correlation with the accumulation rate (Witrant and others, 2012), suggesting that the lock-in zone may be a result of advective versus diffusive timescales. As firn advects downward, it carries air with it. Air can also diffuse through the open porosity, and through much of the firn column the diffusive time scale is shorter than the advective time scale by several orders of magnitude. However, at the lock-in depth the tortuosity has become sufficiently low that the diffusive timescale is comparable to the advective timescale. Under this hypothesis, the positive correlation between accumulation rate and LIZ thickness results from the firn's faster advection rate at higher-accumulation sites: there is a thicker zone over which the diffusive timescale is long relative to the advective timescale, whereas that zone in thinner at a low-accumulation site where the advection rate is slow.

Landais and others (2006) suggested that there are thick lock-in zones at high-accumulation sites because those sites have layering with higher density contrasts than at low-accumulation sites. Hörhold and other (2011) showed that there is indeed more variability in firn density (in the vertical direction) near the lock-in depth at warmer, higher accumulation rate sites. Interestingly, there is less density variability near the surface at warmer, high-accumulation sites than at cold, low accumulation sites (Li and Zwally, 2004; Hörhold and others, 2011), suggesting that the longer firn-densification timescale at colder sites gives the firn more time to approach a homogenous state; i.e. microstructural properties have more time to approach an equilibrium. It is expected that these properties will evolve more quickly at a warmer site, but warmer sites generally have higher

accumulation, meaning that the firn will advect downwards faster than at low accumulation site, giving the firn less time near the surface to equilibrate.

We examine these hypotheses in two ways. We first use scale analysis to compare the characteristic timescales for diffusion an advection in the LIZ. We then use the coupled firn-air and firn-densification modules in the CFM to simulate air transport in layered and unlayered firn at high- and low-accumulation sites.

2.4.1 Scale Analysis

Firn at the lock-in depth is nearing the ice density, so in steady state the downward advection rate is approximately the long-term accumulation rate (ice-equivalent) for that site. This may be ~5 cm ice equivalent (i.e.) a^{-1} at a low accumulation site and ~30 cm i.e. a^{-1} at a high accumulation site. By nondimensionalizing the diffusion equation, we get the diffusive timescale $\tau = \frac{L^2}{\kappa}$, where L is the characteristic length and κ is the diffusivity. We assume that the timescale of gravitational fractionation is approximately the same as the diffusive timescale (Equation 2.1 shows that they are both affected by the open porosity and effective diffusivity). Adolph and Albert (2014) measured effective diffusivity on a core from Summit, Greenland and reported a minimum diffusivity of ~8 m^2 a^{-1} in the lock-in zone. Buizert and others (2012) tuned diffusivity profiles to get firn-air models to reproduce measurements; the tuned diffusivities at the lock-in depth were ~0.3 m^2 a^{-1}, and the models predicted a diffusivity within the lock-in zone of ~0.06 m^2 a^{-1}. We assume a characteristic diffusivity of 0.1 m^2 a^{-1}, which is in the range of the modeled values. We also consider the timescales if the diffusivity is 8 m^2 a^{-1} We assume a characteristic length scale equal to the thickness of an annual layer.

For a low accumulation site ($\dot{b} = 0.05$ m i.e. a^{-1}), the characteristic diffusive timescale (with L = 0.05 m) is 0.025 years, or 9 days, suggesting that diffusive transport dominates at low-accumulation sites. For a high accumulation site ($\dot{b} = 0.3$ m i.e. a^{-1}; L = 0.3 m) the characteristic time scale is ~1 year, which is the same as the advective timescale. This gives support to the advective/diffusive timescale hypothesis. However, for a characteristic diffusivity of 8 m^2 a^{-1}, the diffusive timescale is ~0.01 year, or 4 days. This discrepancy underscores the need for a better understanding of the physical properties of firn near the BCO depth.

Alternatively, we can approach the problem by asking what the diffusivity needs to be so that the diffusive and advective timescales match. We set τ to 1 year so the length scale is the ice-equivalent accumulation rate. For our theoretical low-accumulation site ($\dot{b} = 0.05$ m i.e. a^{-1}), the diffusivity would be 2.5×10^{-3} m^2 a^{-1}, which is much smaller than published values; diffusivities higher than this lead to diffusive processes being much faster than advective processes, implying that diffusion continues to be the dominant transport mechanism. For the $\dot{b} = 0.3$ m i.e. a^{-1} site, the diffusivity for equal timescales would be 0.09 m^2 a^{-1}, which is on the order of published estimates of diffusivity in the lock-in zone. This implies that at high-accumulation sites, advective transport may begin to dominate over diffusive transport near the lock-in depth.

If we instead assume that the lock-in zone is created by an impermeable layer sealing the firn below, we can consider the horizontal extent of a layer that would effectively prohibit a molecule from being transported around it by diffusion. If the impermeable layer is L m wide horizontally, and negligibly thin vertically, a molecule must first travel L/2 m sideways, downward and then back L/2 m, for a total distance of L m. Using a timescale of 1 year, and assuming a diffusivity of 0.1 m^2 a^{-1}, the characteristic length a molecule can travel in a year is 0.31 m. The result is that any layer that is greater than 0.31 m in horizontal extent will block air travel. Note

that this calculation is independent of the downward advection rate, though in reality the impermeable layer would have some thickness that would add to the distance the molecule would travel. Therefore, the 0.31 m horizontal extent is an upper bound. Measurements of horizontal layering in polar firn are scarce, but work by Proksch and others (2015) showed numerous layers with spatial extents of several m and thicknesses of several cm. Our analysis suggests that impermeable layers could be responsible for cutting off gravitational fractionation at the LID. Inherent in this argument is the assumption that impermeable layers could form between permeable layers.

2.4.2 Modeled lock-in zone

We used the CFM to run several model experiments investigating gas transport in the lock-in zone.

In the absence of measurements used to tune a diffusivity profile, firn models must use a parameterization for the diffusivity profile. A problem arises in that the predicted diffusivity profile does not necessarily predict the lock-in depth. To circumvent this problem, firn modelers have used a variety of strategies (e.g. see Buizert and others (2012) and references therein). One option is to specify a lock-in density based upon a (parameterized) close-off depth; for example, Schwander and others (1997) used a lock-in density that was 14 kg m^{-3} less than the close-off density. Using this lock-in depth/density, one can set the diffusivity in the model to become zero or very small at the lock-in depth, which effectively shuts off gravitational fractionation. Other models set gravity to zero in the LIZ or include dispersion within the LIZ in an additional "eddy diffusivity" term in Equation 2.1 that does not include gravitational fractionation.

We follow Witrant and others (2012) with the goal of having the model predict the lock-in depth – that is, gravitational enrichment of heavy isotopes will cease at the correct depth because the model physics are correct, rather than explicitly prescribing the LID.

2.4.2.1 Advective- vs. diffusive-dominated transport

First, we tested the hypothesis that advection becomes the dominant mechanism of gas transport at the lock-in depth by forcing the CFM using the mean temperature (-28.9 °C) and accumulation rate (22 cm i.e. a^{-1}) for the North Eemian (NEEM) ice-core site in northern Greenland. We held surface density constant at 350 kg m^{-3} and used the six parameterizations for diffusivity discussed above.

Figure 2.1 shows the results of the model runs. The solid colored lines are the δ^{15}N profiles predicted by the CFM using each of the diffusivity parameterizations, and the dashed lines are the corresponding diffusivities. The black dots are measurements from NEEM (Rasmussen and others, 2013). The measured lock-in depth at NEEM is 63m, and the full bubble close-off depth (i.e. zero open porosity) is 79 m (Buizert, 2012); these depths are plotted with vertical black lines. The colored dots show the model-predicted $z(\bar{\rho}_{co})$.

Figure 2.2 shows the diffusivity profiles where the diffusivity (as predicted by the parameterization) becomes zero. For all of the parameterizations except the Witrant and others (2012), diffusivity remains relatively high and then decreases sharply to zero, and diffusion remains the dominant transport mechanism. With the Freitag, Severinghaus, and Adolph parameterizations, the diffusivity becomes zero at $z(\bar{\rho}_{co})$ in order to disallow any diffusion beyond the COD. The exception among the diffusivity parameterizations is that of Witrant and others (2012), which maintains a small but non-zero diffusivity beyond the predicted lock-in depth; it is small enough that advection does become dominant.

The CFM air module has the option to include relative-upward air movement due to increased bubble pressure from reduced porosity. We performed model runs with this feature included and excluded. For all parameterizations except Witrant, the results did not change; the

effect of the upward advection is too small to make a difference because of the high diffusivity. For the Witrant parameterization, the low diffusivity at the LID makes inclusion of the upward advection cause a small change in the result.

The Severinghaus, Schwander, and Witrant parameterizations all predict similar diffusivities within the diffusive column, and the model predicts δ^{15}N close to the observations in that zone. The Severinghaus parameterization leads to higher-than-observed values of δ^{15}N beyond the LID because the diffusivity remains relatively high (order 10^1 m^2 a^{-1}) beyond the observed lock-in depth. The Witrant and Schwander parameterizations predict a LID close to the observed depth, leading to predicted δ^{15}N close to, but slightly lower than, the observed values. The Schwander diffusivity falls off gradually through the diffusive column then sharply to zero at LID, leading to a sharp break in slope in the predicted δ^{15}N at the lock-in zone. The Witrant parameterization, on the other hand, drops to zero more gradually because it follows a sigmoid curve, leading to a more rounded slope change as the transport mechanism transitions from diffusion to advection dominated. The Witrant δ^{15}N values level off too quickly, leading to lower-then-observed values beyond the lock-in depth. This may be due to the parameterization predicting the diffusivity drop (i.e. the center of the sigmoid curve) at too shallow a depth, or the CFM may not correctly model the relative upward advection of air. The latter could be caused by incomplete or inaccurate descriptions of the physical processes within the model; for example, the upward flux is controlled by the permeability of the firn, which is not well constrained (Adolph and Albert, 2014).

The Battle parameterization predicts much higher diffusivity than the others through the diffusive column, leading to prediction of higher δ^{15}N values than observed through the firn column. Its diffusivity becomes zero at ~61 m, which does result in it predicting δ^{15}N values

beyond the lock-in depth reasonably well. The Adolph and Freitag parameterizations predict lower diffusivity through the diffusive column, resulting in lower-than-observed δ^{15}N in both the diffusive zone and below the lock-in depth. Both of these models predict an abrupt change in slope in δ^{15}N as the diffusivity becomes zero.

We ran the same experiments for South Pole conditions, and the results are shown in Figure 2.3. Again, the solid colored lines are the $\delta^{15}N$ profiles predicted by the CFM using each of the diffusivity parameterizations and the dashed lines are the corresponding diffusivities. The black dots are measurements from South Pole; the decrease in measured δ^{15}N is due to instrument error (Severinghaus and Battle, 2006). The measured lock-in depth at South Pole of ~115 m (Severinghaus and others, 2001; Severinghaus and Battle, 2006) and close-off depth of 123 m (Buizert, 2011) are plotted with vertical black lines. The results are qualitatively similar to those for NEEM conditions, although for South Pole conditions none of the parameterizations predict the lock-in particularly well. The Battle parameterization again predicts high diffusivity through the diffusive zone, but it predicts diffusivity dropping to zero at a depth such that the δ^{15}N value past lock-in is the same as the Witrant parameterization.

For South Pole conditions, the Witrant parameterization again predicts a gentler rounding off of the δ^{15}N profile, and the modeled δ^{15}N in the LIZ lower than the measurements. As for NEEM conditions, the diffusivity is non-zero through the lock-in zone. The 'round off' in this case is much more gradual; the model has a more gradual shift from diffusion- to advection-dominated transport. This appears counter to the observations that the LIZ is thinner at low-accumulation sites. Again, possible reasons for this discrepancy are that the model is not simulating relative upward motion correctly, or the parameterization does not accurately predict the diffusivity near the LID.

For both NEEM and South Pole, the model results do not clearly support the hypothesis that advection becomes the dominant transport mechanism in the lock-in zone, but neither does it disprove it.

2.4.2.2 High- and low-density layers

We also used the CFM to investigate the effect of layers on the lock-in depth. We forced the CFM with the NEEM accumulation and temperature, but where previously we held the surface density constant at 350 kg m^{-3}, we now varied the surface density. We created a surface density time series by randomly drawing a value from the normal distribution with mean 350 kg m^{-3} and standard deviation 50 kg m^{-3}. Each model run (i.e. with the six different parameterizations) used the same surface-density time series to enable direct comparison. The results of this experiment are shown in Figure 2.4.

The results are similar to those shown in Figure 2.1; the density variability does not make a significant difference in the mean δ^{15}N profile beyond the close-off depth, but it does add a small (1-2 per mil) amount of variability to the modeled profile beyond the mean LID because the layers do alter the LID slightly through time. The various diffusivity parameterizations show different sensitivities to the variable density: The Battle parameterization is quite sensitive; the Freitag and Adolph parameterizations are rather insensitive, especially at depth. The Witrant parameterization is completely insensitive at depth because it not dependent on porosity (open or total) beyond the critical depth. The density layering does not affect the δ^{15}N profile in most of the diffusive column because the diffusivity within the denser layers is still high enough for diffusion to occur readily.

2.4.3 Discussion

The model results do not clearly support one hypothesis of the physics around the LID, which may be due to a limited knowledge of the firn around the lock-in depth. We use an empirical firn

densification model to provide the porosity, and then we calculate the open porosity using a parameterization. We then use that to parameterize the diffusivity. Even though firn-density models can predict a bulk density profile accurately, they cannot describe small-scale properties. It may not be appropriate to use parameterizations for diffusivity based on density at all because density is not the same as the permeability and tortuosity. Additionally, it is not known at what scales we need to know the permeability and tortuosity at in order to accurately predict the effective diffusivity. Unfortunately, the current understanding of microstructural evolution of firn limits the community's ability to predict tortuosity.

The results for NEEM with the Witrant parameterization support the idea that advection takes over as the dominant transport mechanism, but for South Pole it is not as clear. Additionally, at NEEM the Schwander parameterization performs just as well. Most of the parameterizations do not predict sufficiently low diffusivity at/near the lock in, so diffusion continues to dominate until diffusivity becomes zero.

It is not surprising perhaps that the Witrant and others (2012) parameterization predicts the LID relatively well: it was designed to work in concert with parameterizations for open and closed porosity and the mean close-off depth developed by Martinerie and others (1992), and those are the equations used in the CFM to predict porosity and close-off depth/density. Additionally, it is not surprising that the parameterization produces diffusivities low enough to enable advection-dominated transport because it was developed under the hypothesis that advection should become dominant at the LID. That said, of the six parameterizations, it most closely matches the tuned diffusivity profile for NEEM (Buizert and others, 2012), which also has a more gradual drop off in diffusivity, and has non-zero diffusivity through the lock-in zone.

The fact that the model with layering does not predict an LID that matches the observed LID does not negate the hypothesis that layering creates the LID. The model experiment may be problematic because firn-densification models do not predict density variability at depth well, e.g. the second maximum in density variability reported in Hörhold and others (2011), which suggests that firn models are missing descriptions of some physics. It is probable that these missing physics deal with microstructural evolution of the firn because firn-density models can predict bulk depth-density profiles well, whereas fine-scale layering is likely a function of microstructural properties such as grain size and coordination number. These properties in turn affect tortuosity, which is the actual firn property of interest for firn-air studies (i.e. it determines the permeability and effective diffusivity).

We can model firn air adequately in the modern firn because we can tune the diffusive profile to measurements, but our current understanding of the firn near the LIZ limits our ability to model firn air in the past. To rectify this problem, we first need to both model the bulk diffusivity correctly through the diffusive column, and second we need to understand microphysics of the firn in the lock-in zone. Progress is being made through lab work examining the microstructure of firn using micro-CT scanning (e.g. Adolph and Albert, 2014; Schaller and others, 2017); continued studies such as these are essential to both incorporate microstructural evolution into firn-densification models and to better understand the physics of gas transport in the LID. Ideally future studies will also target larger samples to better understand the spatial (x-y plane) heterogeneity of firn.

Although our results do not provide a clear answer for cause of the LID, we suggest that it is likely a combination of small-scale layering and competing gas transport mechanisms. The results using the Witrant parameterization for diffusivity at NEEM strongly suggest that the

timescale for diffusion becomes too long near the LID compared to the timescale for advective transport, but our scale analysis suggests that layers do not need to be spatially extensive to effectively block air transport near the LID.

2.5 ISOTOPES AND FIRN-THICKNESS CHANGE DURING CLIMATE CHANGES

Gas isotopes fractionate in firn due to gravity (heavier isotopes become enriched at greater depths) and due to thermal gradients (heavier isotopes become enriched in the colder part of the firn) (Severinghaus and others, 1998). In a steady climate, there are seasonal temperature gradients near the surface (upper ~10 m of firn), but there is not a temperature gradient in the deeper firn. As a result, there is no thermal fractionation throughout most of the firn column. During climate-change events, the surface warms or cools and creates a temperature gradient between the surface and the LID, causing thermal fractionation. Different gas species have different thermal sensitivities, and this fact can be exploited to infer the magnitude of temperature changes during rapid climate-change events. Previous work showed that the temperature at Summit, Greenland increased by ~9 C over the course of several decades during the Bølling Transition (Severinghaus and Brook, 1999) and by 5-10 C over a century during the Younger Dryas (Severinghaus and others, 1998). In both these cases, the authors examined δ^{15}N and δ^{40}Ar isotopes; δ^{15}N and δ^{40}Ar/4 will have the same gravitational fractionation. Any deviation of these species in the firn from one another is a result of thermal fractionation. The authors modeled gas isotopes to infer temperature increases, but their model did not fit the data perfectly because the model assumed a steady-state firn column and was unable to account for transient firn thickening due to an accumulation-rate increase coincident with the temperature increase; their model predicted values ~3-4 per mil less than the observed values.

We used the CFM to examine the effect of transient firn evolution on gas records in ice cores during rapid climate-change events. We ran two model simulations of the evolution of δ^{15}N

and δ^{40}Ar in the firn. Both simulations ran for ~49,000 years, which is the length of the GISP2 temperature and accumulation-rate records (Alley, 2004). We ran the model using yearly time steps, and the model domain extended to a depth of ~2200 m. The difference between the model runs was the firn depth-density profile: in the first simulation, we used a constant profile; in the second, we used a transient firn-densification model to allow the density to evolve with the climate.

For the first simulation, we used the steady-state depth-density profile predicted by the Herron and Langway (1980) model with an accumulation rate of 0.07 m i.e. a^{-1} and a temperature of -47.5°C, which are consistent with values during the Younger Dryas and leading into the Bølling Transition and those used for modeling in Severinghaus and others (1998) and Severinghaus and Brook (1999). We allowed the temperature in the firn to evolve using the CFM's temperature-evolution module; we forced the model using a temperature history derived from the GISP2 ice core (Figure 2.5; Alley, 2004). This temperature did not affect the steady-state depth-density profile, and the lock-in depth stayed constant (Figure 2.6) at ~97 m.

For the second simulation, we used the GISP2 temperature and accumulation-rate data (Figure 2.5; Alley, 2004) to run the firn-densification model in transient mode using the Herron and Langway (1980) equations. In addition to the temperature-profile evolution, this simulation allowed the firn depth-density profile to evolve, causing the lock-in depth to vary through time (Figure 2.6).

Figure 2.7 shows the results of the two simulations and the δ^{15}N and δ^{40}Ar data from Severinghaus and others (1998) and Severinghaus and Brook (1999). The horizontal axis of the plot is the gas age. The δ^{15}N and δ^{40}Ar data were converted from depth to gas-age using the GICC05 timescale (Rasmussen and others, 2014; Seierstad and others, 2014). The gas ages predicted by the model are too young compared to the data; we correct for this by adding 2% to

the modeled gas ages, which gives generally good agreement with the data at the Bølling Transition and Younger Dryas. The model is likely failing to produce the correct gas age for 2 reasons: (1) the modeled gas age is predicted by assuming a uniform gas age of 15 years at the lock-in depth, and (2) the gas age is dependent on the model-predicted age of the firn at the lock-in depth, which is not necessarily accurate (see e.g. Chapter 3.4).

For the steady-state simulations, variability in the isotope values is due only to fractionation from temperature gradients in the firn. For the transient model runs, the variability is due to both fractionation from temperature gradients and to changes in the firn-column thickness.

Much of the difference between the transient and steady-state simulations shown in Figure 2.7 can be attributed to the change in firn-column thickness. For example, at ~14,500 years before present, the peak of the δ^{15}N predicted by the transient model is about 0.02 per mil higher than the steady-state run. In this case, the increased firn thickness results in more gravitational fractionation. However, the curves are also offset from one another, because (1) the temperature gradients that form in the firn are different in the transient firn than in the steady-state firn and (2) the time scales of diffusion are slightly different; i.e. a thicker diffusive column in the firn will result in a smaller temperature gradient in that column for the same surface temperature increase, and it will also take longer for the thicker firn to come to a new equilibrium.

On the whole, the transient model matches the data better than the steady-state model, especially during the Younger Dryas and its termination. Notably, the transient model does well predicting the high values of δ^{15}N and δ^{40}Ar/4 associated with the rapid warming at the end of the Younger Dryas. These values are ~0.03 per mil higher than those predicted by the steady-state model and are consistent with the model-data misfit in Severinghaus and others (1998), who used a fixed LID. Figure 2.8 shows the model results and data zoomed in on the later part of the Younger

Dryas and its termination; in this figure we have shifted both the steady-state and transient results to zero leading into the Younger Dryas to directly compare the magnitude of the δ^{15}N and δ^{40}Ar/4 changes predicted by the models. The transient model predicts ~0.05 per mil more fractionation at the end of the Younger Dryas than the steady-state model as a result of the increased accumulation. This 0.05 per mil equates to ~10 m of firn thickening.

After the Younger Dryas, the modeled δ^{15}N drops quickly, as do the data, but the model is delayed in that reduction. This is due to a temperature decrease after the initial increase, which causes more thermal fractionation. The overall decrease in δ^{15}N (at ~11,500 years B.P. for the data and ~11,250 years B.P. for the model) does indicate that after an initial thickening due to increased accumulation, the firn is thinning due to the warmer temperature and there is less thermal fractionation as the temperature gradient in the firn is reduced under more stable climate conditions.

Figure 2.9 shows the modeled and measured δ^{15}N and δ^{40}Ar/4 zoomed in on the Bølling Transition. Again, we have shifted both the steady-state and transient results to zero leading into the Bølling Transition to illustrate the model's predicted magnitude change. The transient model matches the observed the magnitude and rate of the δ^{15}N and δ^{40}Ar/4 change much better than the steady-state model. However, there is a 0.05 per mil offset between the transient model and the data, suggesting that the model is predicting a lock-in depth that is ~10 m too shallow (~10% of the firn column thickness). This may be caused by forcing-data uncertainty: around -47°C and 0.07 m i.e. a^{-1}, the Herron and Langway (1980) model predicts a 4 m change in LID for a 1°C change in temperature and a 5 m change in LID for a 0.01 m i.e. a^{-1} change in accumulation rate change; a small uncertainty in the forcing data for either of these variables could account for the 0.05 per-mil offset. The model-data discrepancy could also be caused by model inadequacy: the

Herron and Langway (1980) model was calibrated using only two cold, low accumulation sites, so its validity in those conditions may be questionable. The model also may not be predicting a large enough temperature gradient, which could occur if the temperature increase in the forcing data was not large enough.

Despite the lingering model-data mismatch, the transient model clearly performs better than the steady-state model, and our model results during the Younger Dryas and Bølling Transition corroborate the assertion in Severinghaus and Brook (1999) that their model-data misfit is due to transient firn thickening. Our results do not change their conclusions but do provide assurance that their conclusions are sound. This experiment also demonstrates the utility of coupling a firn-air model to a firn-density model. In this case, the coupled model should allow a more accurate assessment of the magnitude of temperatures because it can account for the temperature gradient that will form in thickening firn, which is smaller than that in steady-state firn. As discussed with the previous experiment, a continuing challenge is that most firn-densification models (including Herron and Langway (1980)) were developed with a steady-state assumption and applying them to transient simulations produces additional uncertainty. This uncertainty is challenging to quantify, however, because we do not have direct observations of firn evolution during rapid climate changes.

The model has additional potential to help test hypotheses surrounding anomalies in ice core records. For example, it may help provide insights on the mismatch between δ^{15}N from the last glacial period observed in East Antarctic ice cores and the LID predicted by firn models (Landais and others, 2006). The CFM's ability to model multiple physical processes in a single framework allows us to investigate processes with different timescales. For example, a temperature change (with no concurrent accumulation-rate change) will create a temperature gradient in the

firn and also will cause the firn to change thickness, but those processes will operate on different timescales.

2.6 TRANSIENT FIRN DURING A CO_2 INCREASE

For our final model application, we used the CFM to simulate the ice-core gas profiles of CO_2 that would result from an increase of CO_2 in the atmosphere in concert with transient firn evolution. We ran the model for 2000 years, holding the CO_2 concentration in the atmosphere at 300 ppm from 0 to 800 years. Between 800 and 1000 years, we linearly increased the CO_2 from 300 to 400 ppm, and then held it constant at 400 ppm from 1000 to 2000 years.

We ran four model experiments with the CO_2 increase. All of the experiments were run using annual time steps, and we used the Schwander and others (1988) parameterization for diffusivity, which is dependent on the total porosity. We also simulated δ^{15}N in the firn during the model runs. The results are shown in Figures 2.10 – 2.15.

For the first experiment, our baseline, steady-state case, we held constant the temperature (-28.9°C), accumulation rate (0.22 m i.e. a^{-1}), and surface density (350 kg m^{-3}). The CO_2 profile in the firn and ice is 300 ppm at depth and increases to 400 ppm over depth range of ~45 m (Figure 2.10), corresponding to the 200 years of CO_2 increase (Figure 2.11). The δ^{15}N profile is constant with depth because the lock-in depth does not change (Figure 2.12).

For the second experiment, we examined the effect of density variability on gas records. We used the same constant temperature and accumulation, but we varied the surface density, which was determined at each time step by drawing a sample from a normal distribution with mean 350 kg m^{-3} and standard deviation 50 kg m^{-3}. The minimum surface density was set to 300 kg m^{-3} and maximum to 700 kg m^{-3}. The CO_2 profile does not deviate significantly from the steady-state case: high-density layers block the CO_2 diffusion temporarily at shallower depths than the mean close-

off depth, but lower-density layers allow the CO_2 signal to diffuse to a slightly deeper depth than the mean close-off depth, resulting in a stair-step pattern. The $\delta^{15}N$ signal reflects the slight variations in the lock-in depth that result from this density variability.

In the third experiment we examined the effect of an ice lens (e.g. a surface melt layer) on the gas record by holding the surface density constant except at time=850 years (1/4 of the way through the CO_2 increase), when we included at single layer with an initial density of 800 kg m^{-3}. In this experiment, the lens is not actually impermeable at the surface (according to the Schwander diffusivity parameterization) because its density is only 800 kg m^{-3}. Diffusivity is high enough in that layer that gas can still diffuse through it, and the CO_2 profile in the ice increases at the same rate as the baseline case. Eventually, the diffusivity becomes low enough in the layer that it blocks diffusion of gasses. Figure 2.14 shows the depth-density profile and Figure 2.15 shows the depth-diffusivity profile at t=900 years; the ice lens can be clearly seen in both plots as a spike in density and low in diffusivity. The CO_2 concentration in the firn below (deeper than) the impermeable layer is locked at the concentration it was at when the layer became impermeable. The firn above the blocking layer continues to be in equilibrium with the atmosphere. When the firn above the lens reaches the close-off density, bubbles of air with the atmospheric concentration of CO_2 are trapped, and the concentration of CO_2 trapped in the ice rapidly shifts (near-vertical line in Figure 2.11) because it represents a single layer transitioning from not trapping air to trapping air in one time step. If this were to occur in nature, the transition would be slightly more gradual because of density variability near the close-off depth. The $\delta^{15}N$ profile in this experiment shows similar behavior to the CO_2 profile: The ice lens effectively locks in the $\delta^{15}N$ profile below the lens, and that profile is advected downward through the firn. In the firn between the surface and the lens, the $\delta^{15}N$ profile follows the barometric line of gravitational fractionation. This

downward spike is consistent with the δ^{15}N observed near a suspected melt layer in the NEEM ice core (Dahl-Jensen and others, 2013).

For the fourth experiment, we examined the effect of transient firn on the gas records by linearly increasing the temperature by 4°C and the accumulation rate by 0.02 m i.e. during the 200-year period of increasing CO_2. We held the surface density constant at 350 kg m^{-3}. The CO_2 profile with age (Figure 2.11) is the same as with the steady-state case, but the onset of the decrease in CO_2 is deeper because of the higher accumulation. In this experiment the δ^{15}N values initially increase because the increased accumulation rate causes the firn to thicken. Then, the δ^{15}N decreases because the warmer temperature causes the firn to densify faster, which results in thinner firn. This illustrates two time scales on which firn densification can operate: firn has an immediate reaction to an accumulation rate because it affects the surface, whereas there is a longer response time to temperature change because the change must be diffused and advected through the firn.

This model application again demonstrates the utility of a coupled firn-air-firn-densification model. In this case, the model provides insight into the effect of an ice-lens on the gas record in an ice core. A single impermeable ice lens during a linear increase of CO_2 is an idealized scenario, but future work includes more sophisticated model experiments to test hypotheses stemming from ice-core observations.

2.7 CONCLUSIONS

We have coupled a firn-air model to a firn-densification model. We demonstrated the utility of this coupled model, especially for understanding firn-air records in the past and during climate changes when the firn is changing, through three model applications and evaluations of the model. In the first application, our results suggested that the lock-in depth can at least in part be explained by low diffusivity that allows advection to dominate transport, thus effectively stopping

gravitational fractionation. Small-scale layering in the firn also may play a role in creating the lock-in zone, but current firn-densification models are not able to resolve firn structure at fine-enough resolution. Our second application demonstrated that the coupled model can predict records of isotopes in ice cores better than a firn-air model that uses a steady-state firn density profile. Our third application showed the effects of an ice lens on gas records preserved in ice cores.

All three applications showed that including firn evolution is essential to modeling gas transport correctly. These applications are all limited by our understanding of the microstructure of firn and its effects on gas transport. Future work investigating the evolution of firn microstructure, and how the microstructure influences gas transport, is essential. The coupled model can also help us understand where models are failing, and these understanding these deficiencies can help to drive research directions needed for model improvement.

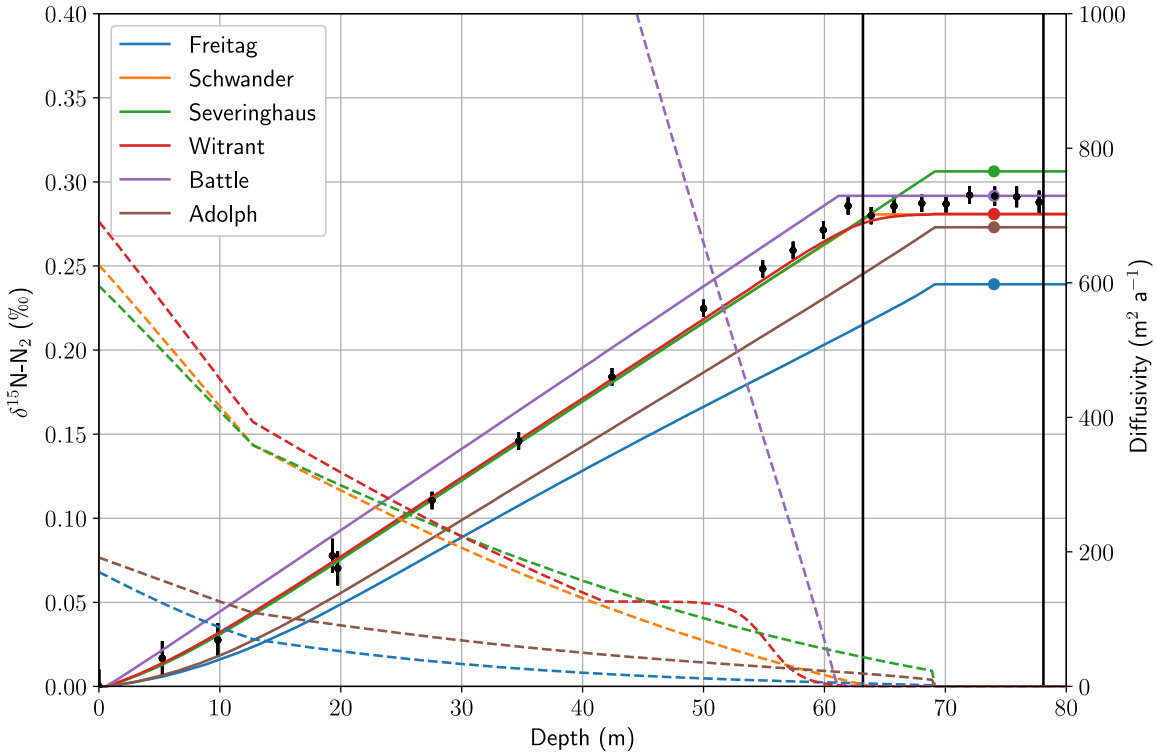

Figure 2.1. Measured and modeled δ^{15}N profiles and parameterized diffusivity for NEEM. Solid lines are the δ^{15}N profiles predicted using each of the diffusivity parameterizations. Dashed lines are the diffusivity profiles predicted by the parameterizations. Colored dots indicate the model-predicted bubble close-off (zero-porosity) depth. Vertical black lines show measured lock-in depth and close-off depth at NEEM. Black markers show δ^{15}N measurements with error bars from the EU borehole at NEEM (Buizert and others, 2012).

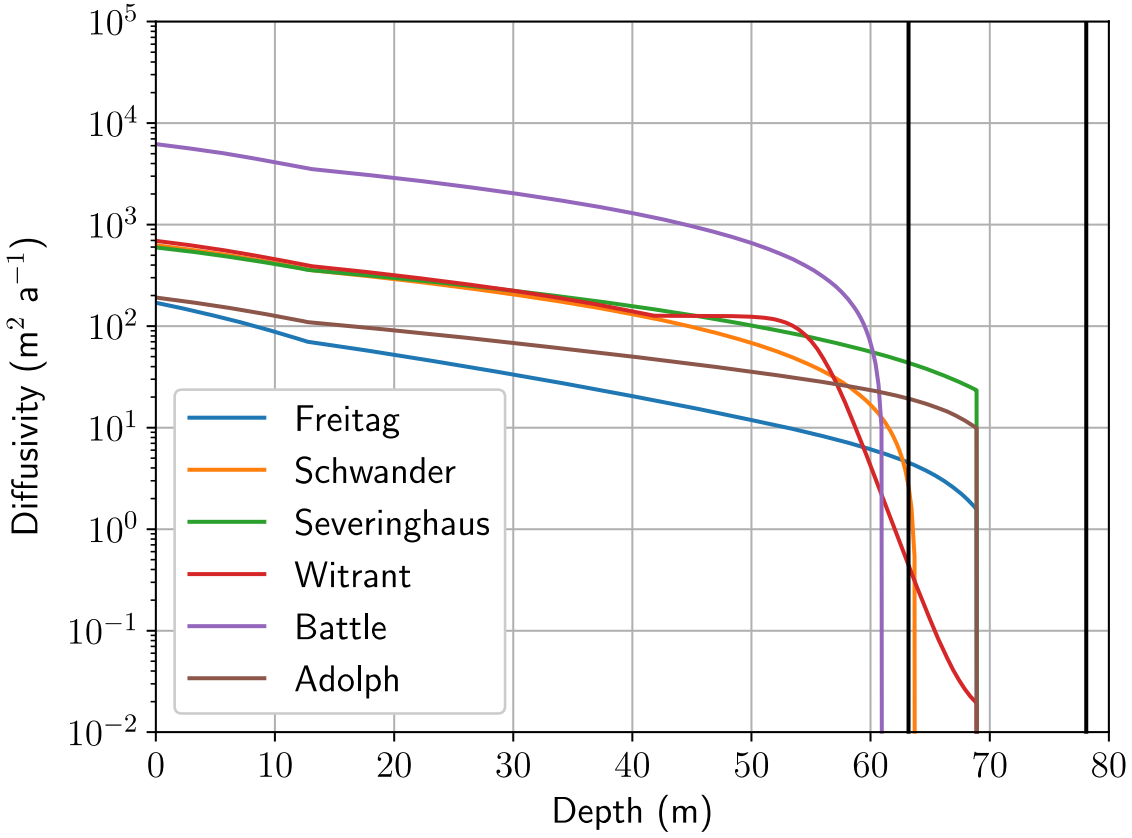

Figure 2.2. Diffusivity vs. depth predicted by the six diffusivity parameterizations for NEEM. Vertical black lines show measured lock-in depth and close-off depth at NEEM.

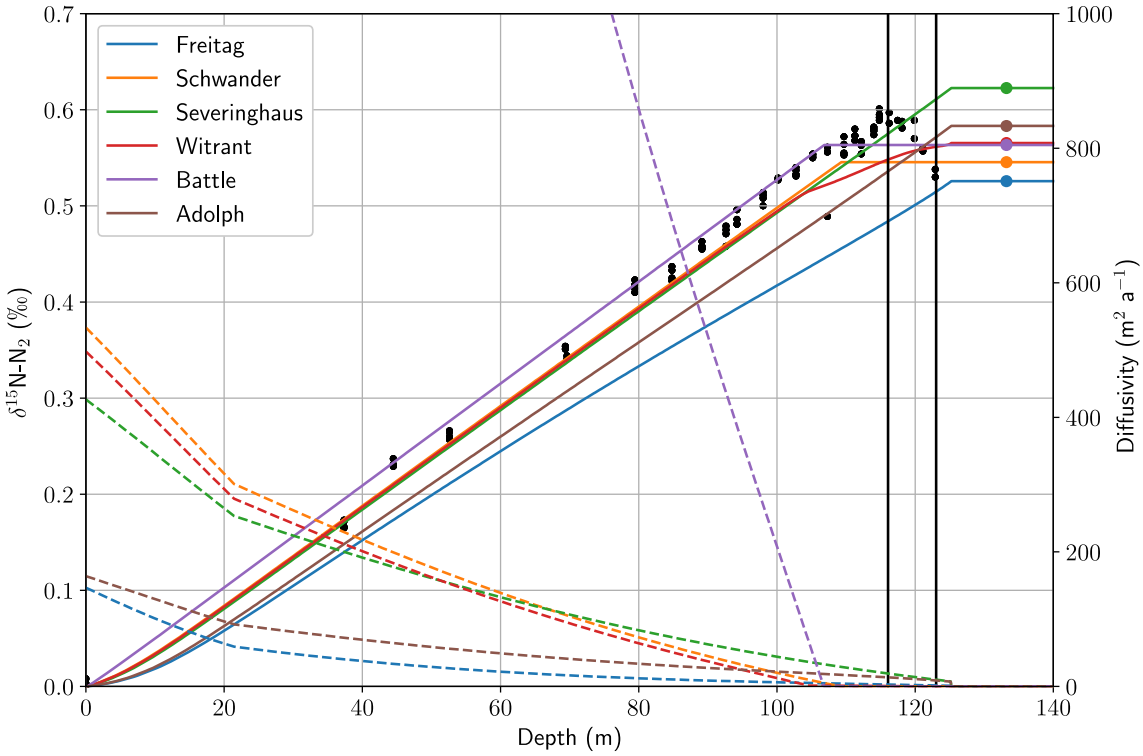

Figure 2.3. Measured and modeled δ^{15}N profiles and parameterized diffusivity for South Pole. Solid lines are the δ^{15}N profiles predicted using each of the diffusivity parameterizations. Dashed lines are the diffusivity profiles predicted by the parameterizations. Colored dots indicate the model-predicted bubble close-off (zero-porosity) depth. Vertical black lines show measured lock-in depth and close-off depth , and black dots show δ^{15}N measurements at South Pole (Severinghaus and Battle, 2006).

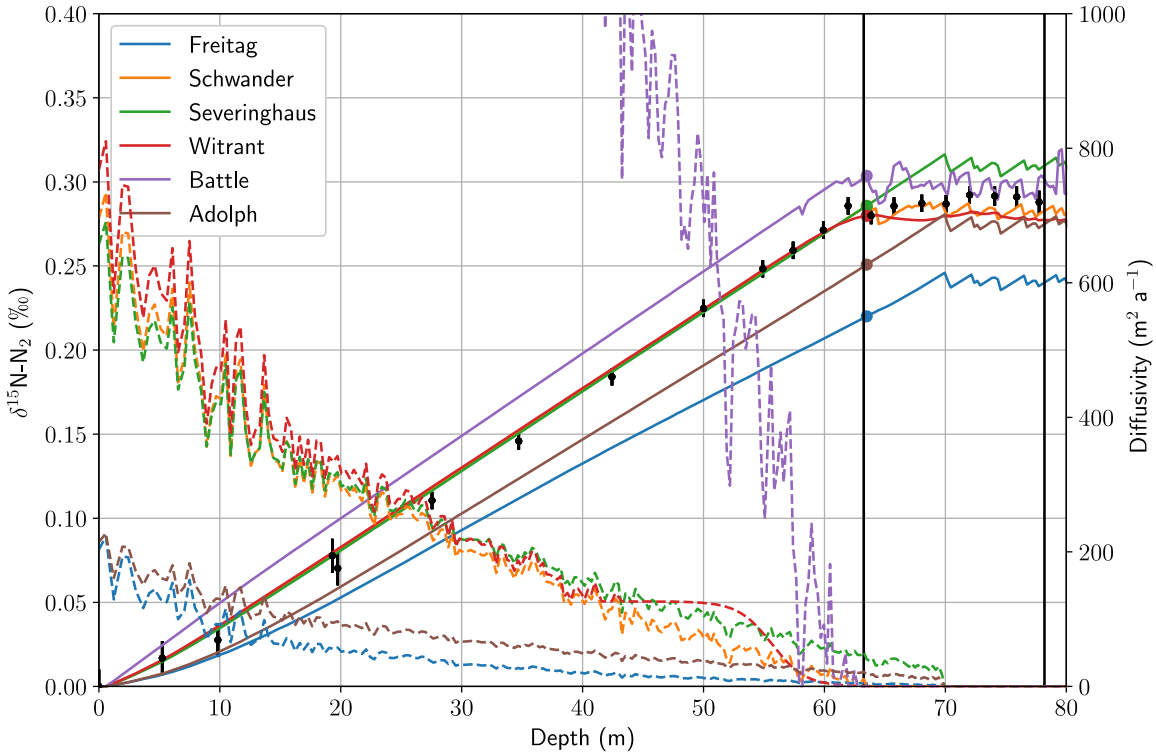

Figure 2.4. As in Figure 2.1, but with added surface-density variability. Solid lines are the δ^{15}N profiles predicted using each of the diffusivity parameterizations. Dashed lines are the diffusivity profiles predicted by the parameterizations. Colored dots indicate the model-predicted bubble close-off (zero-porosity) depth. Vertical black lines show measured lock-in depth and close-off depth at NEEM. Black markers show δ^{15}N measurements with error bars from the EU borehole at NEEM (Buizert and others, 2012).

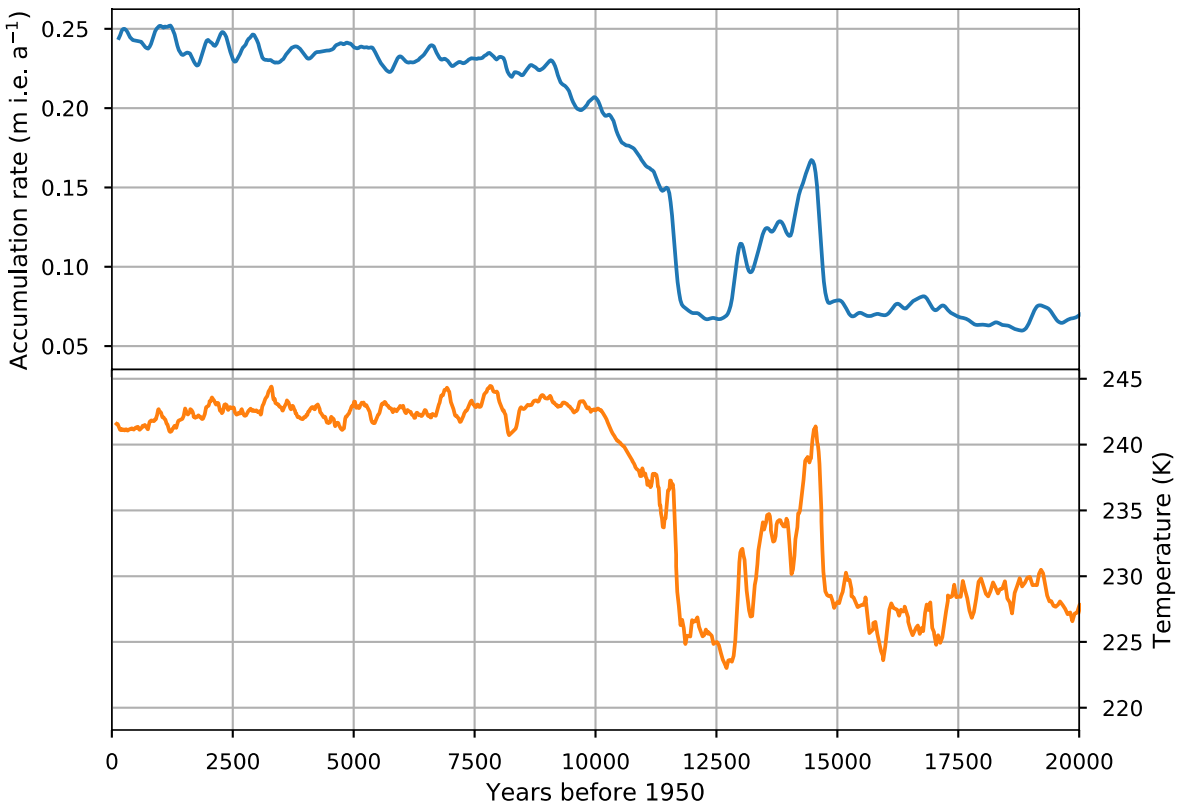

Figure 2.5. Accumulation-rate and temperature histories derived from the GISP2 ice core and used to force the CFM for the analyses in Chapter 2.5 (Alley, 2004).

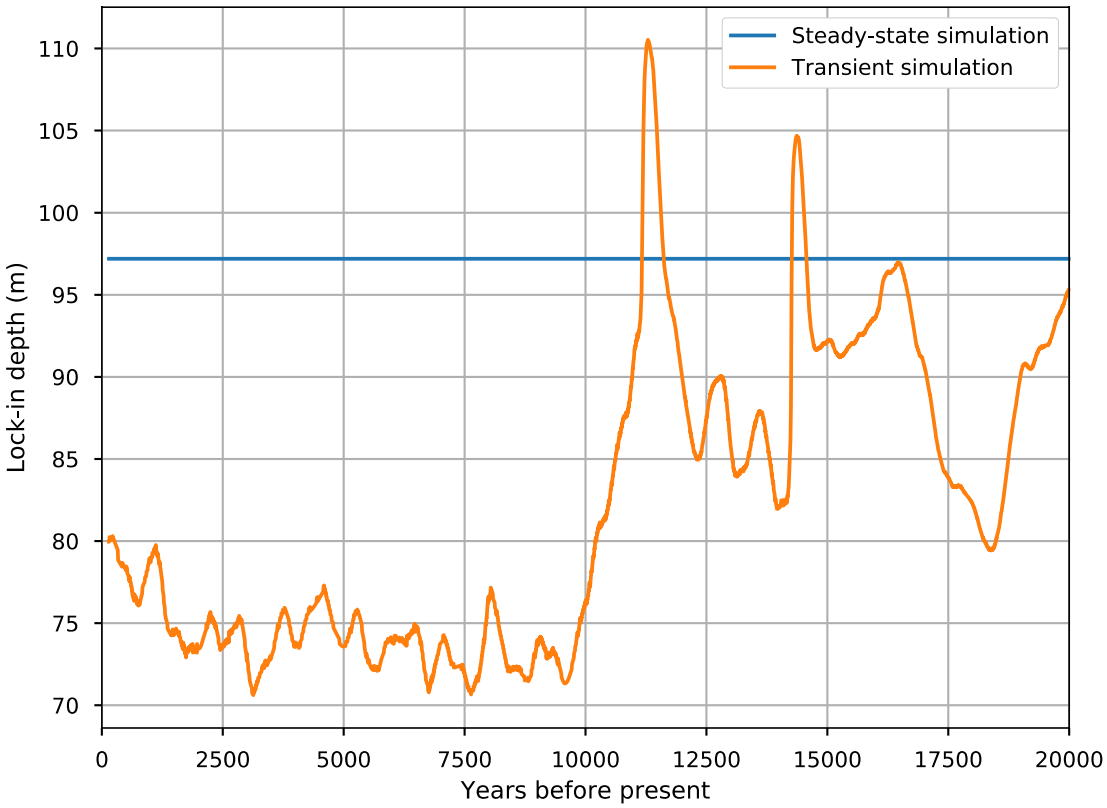

Figure 2.6. Lock-in depth predicted by the steady-state and transient model simulations in Chapter 2.5. The LID for the transient simulation is determined by running the CFM with the climate shown in Figure 2.5, and the LID for the steady-state simulation is that predicted by the Herron and Langway (1980) model with accumulation rate = 0.07 m a^{-1} ice equivalent and mean annual temperature = -47.5°C.

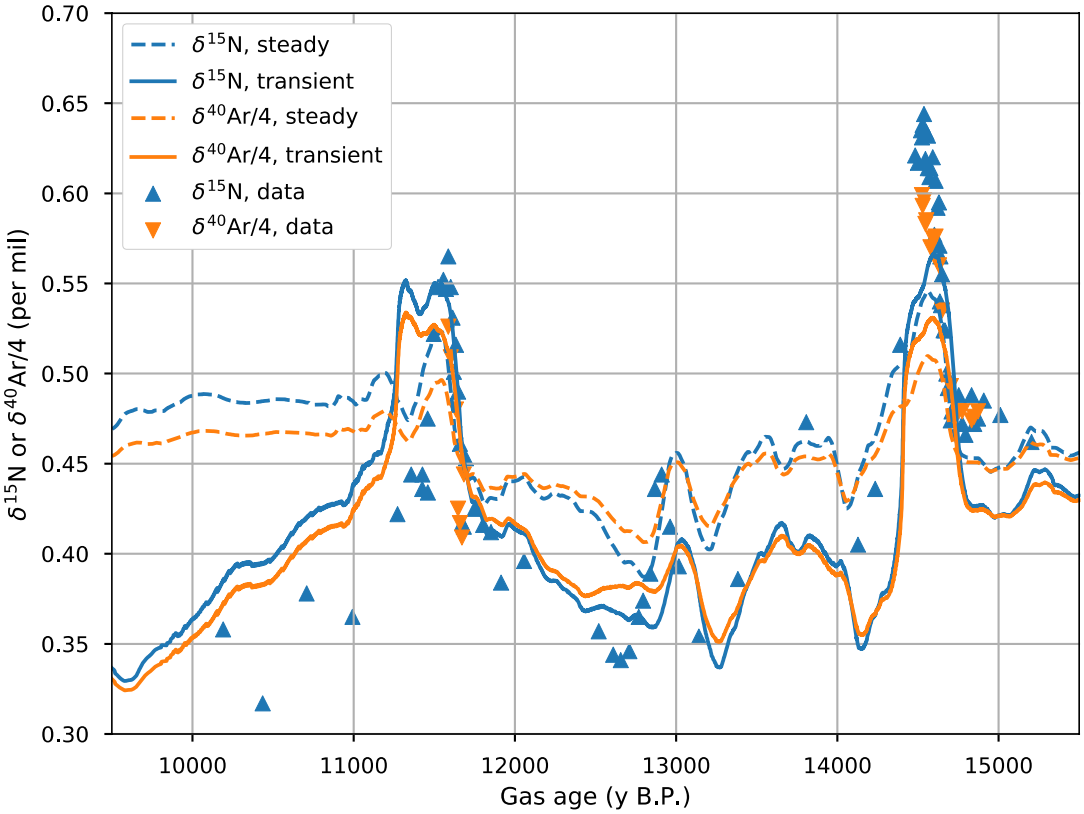

Figure 2.7. Measured and modeled δ^{15}N and δ^{40}Ar profiles. Data are from Severinghaus and others (1998) and Severinghaus and Brook (1999). We add 2% to the modeled gas to fit the timing of the modeled gas ages to the data.

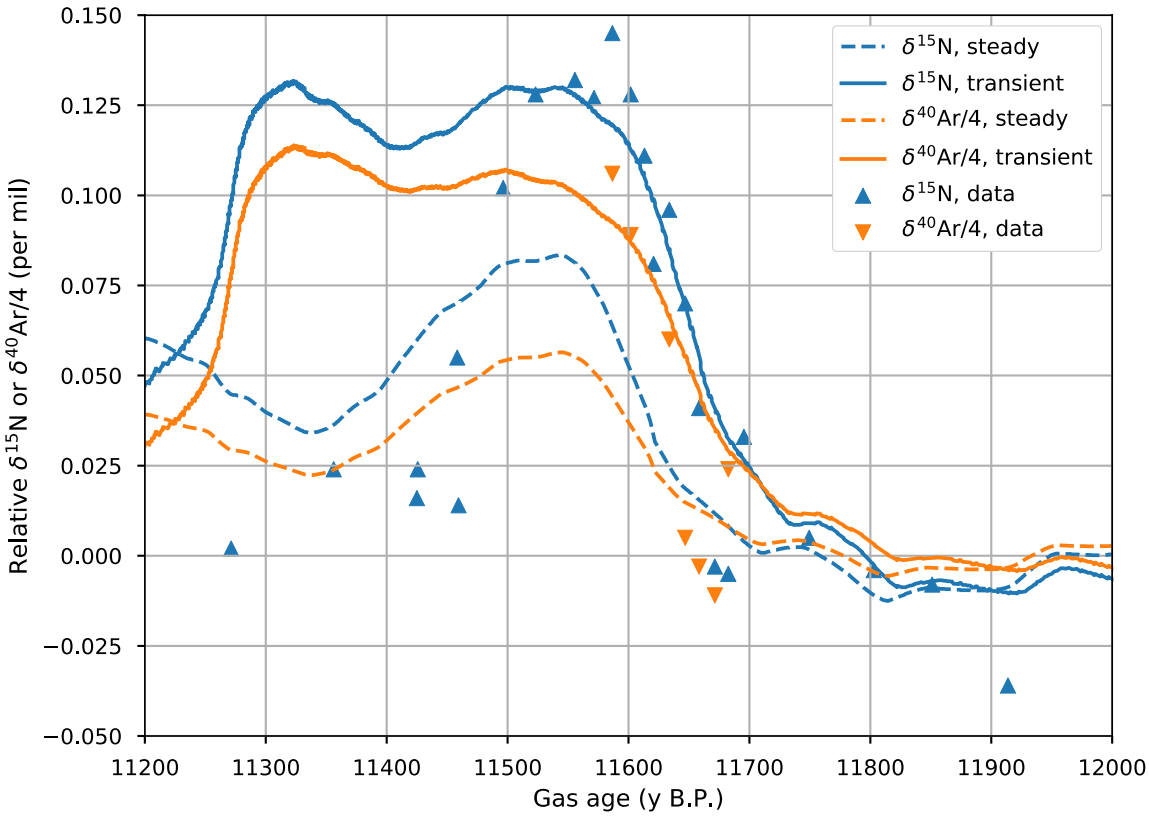

Figure 2.8. As in Figure 2.7, but zoomed in to the Younger Dryas. We have shifted the y axis to match the transient and steady-state simulation results leading into the Younger Dryas to highlight the magnitude of the modeled changes compared to the data.

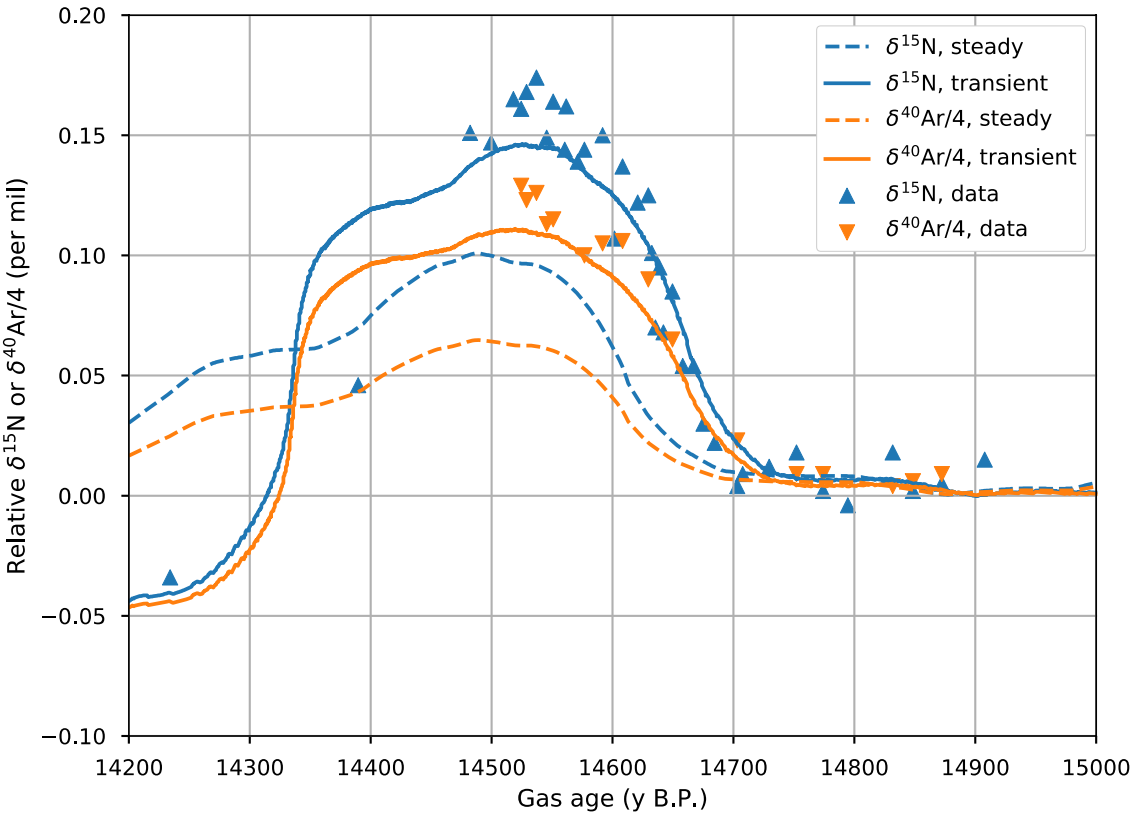

Figure 2.9. As in Figure 2.7, but zoomed in to the Bølling Transition. We have shifted the y axis to match the transient and steady-state simulation results leading into the Bølling Transition to highlight the magnitude of the modeled changes compared to the data.

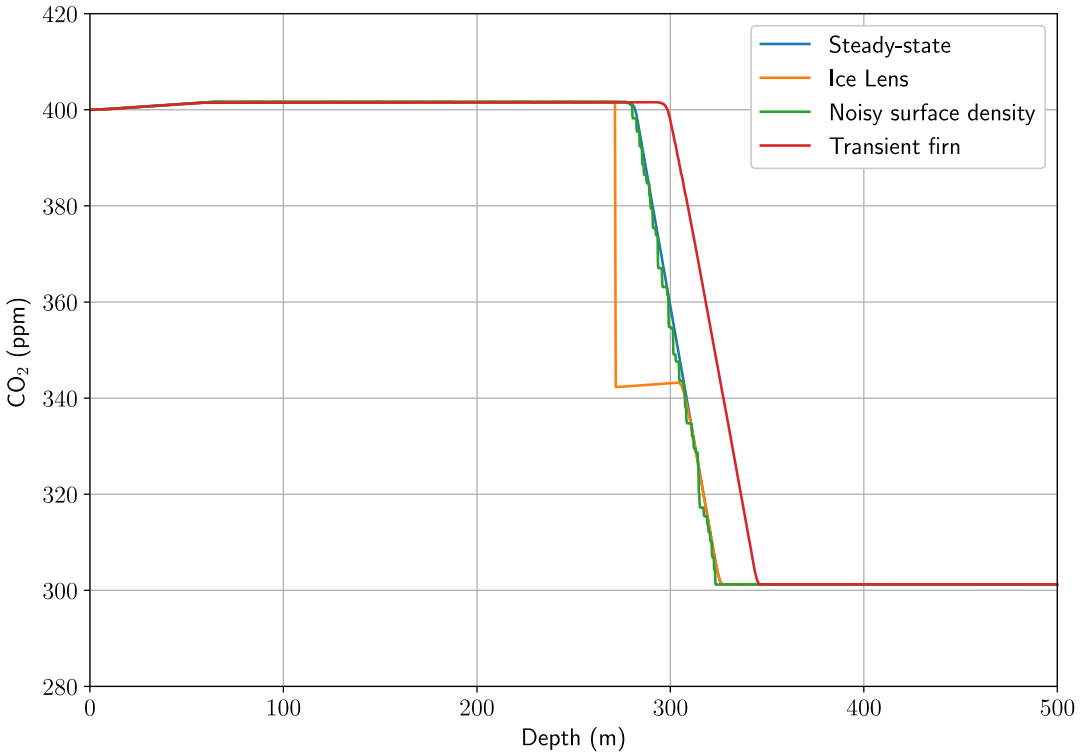

Figure 2.10. CO_2 concentration in the firn and ice vs. depth at the end (t=2000 years) of the model runs described in Chapter 2.6.

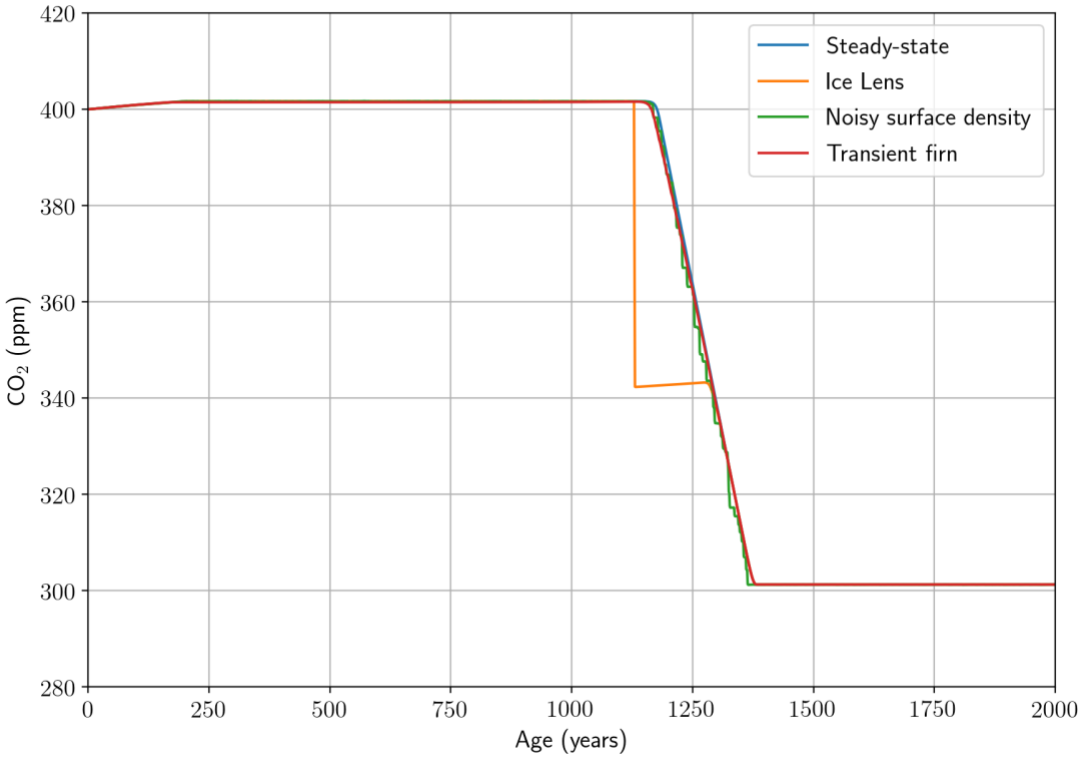

Figure 2.11. CO_2 concentration in the firn and ice vs. age at the end (t=2000 years) of the model runs described in Chapter 2.6.

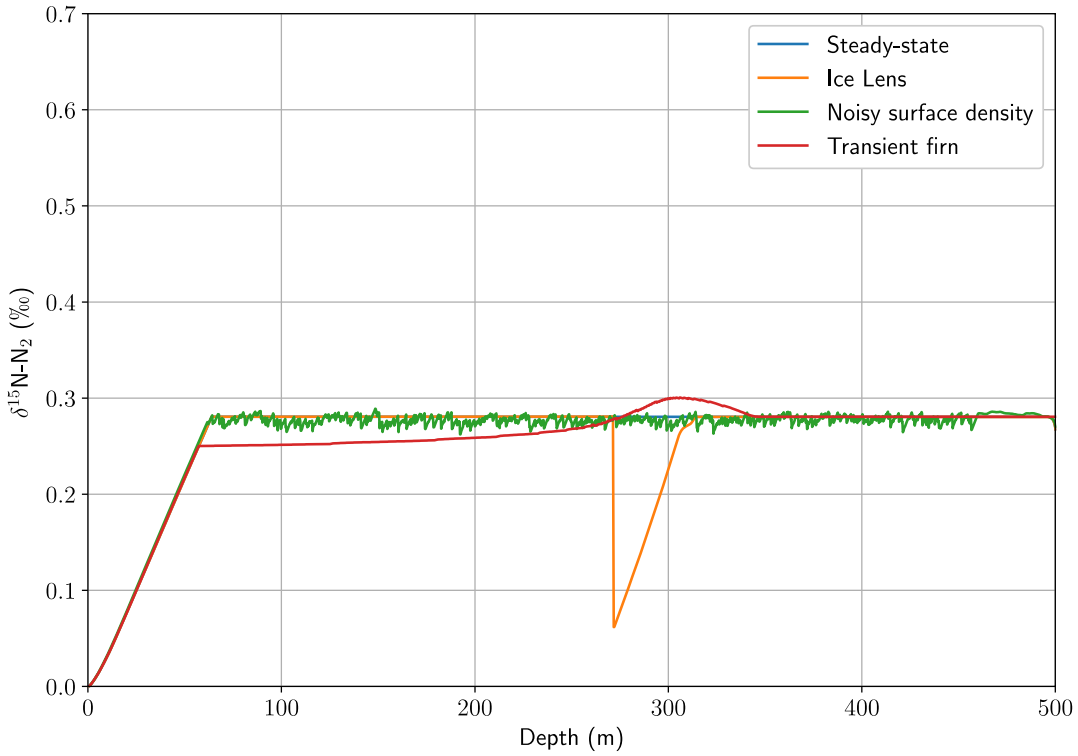

Figure 2.12. δ^{15}N concentration in the firn and ice vs. depth at the end (t=2000 years) of the model runs described in Chapter 2.6.

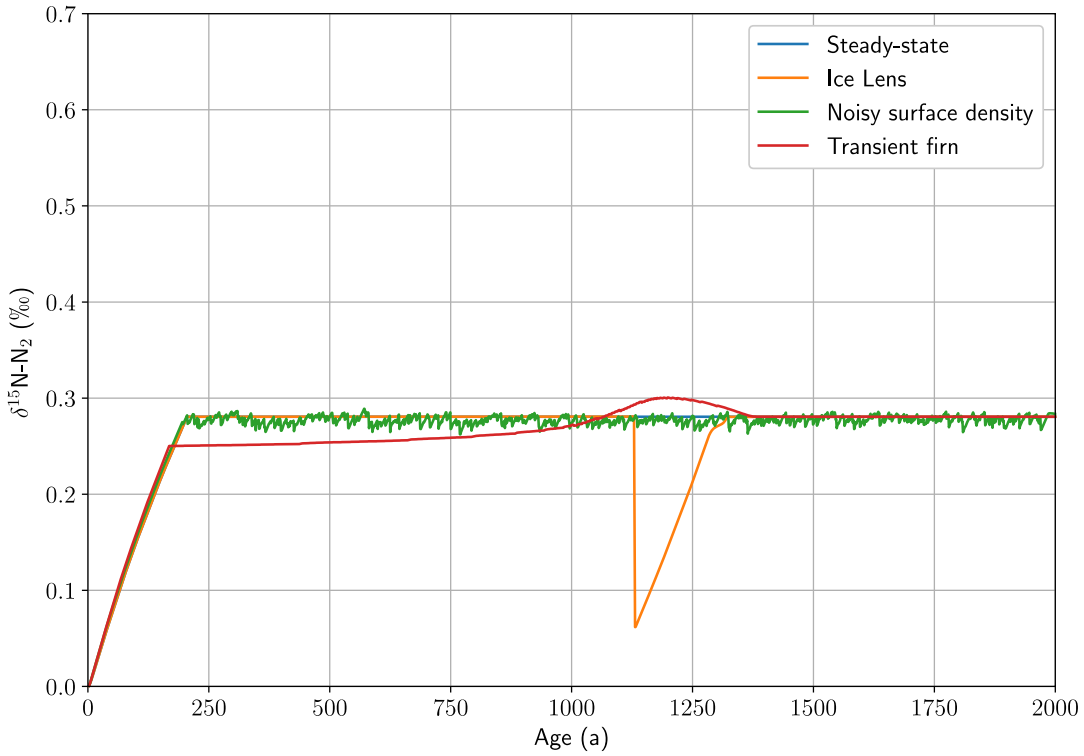

Figure 2.13. δ^{15}N concentration in the firn and ice vs. age at the end (t=2000 years) of the model runs described in Chapter 2.6.

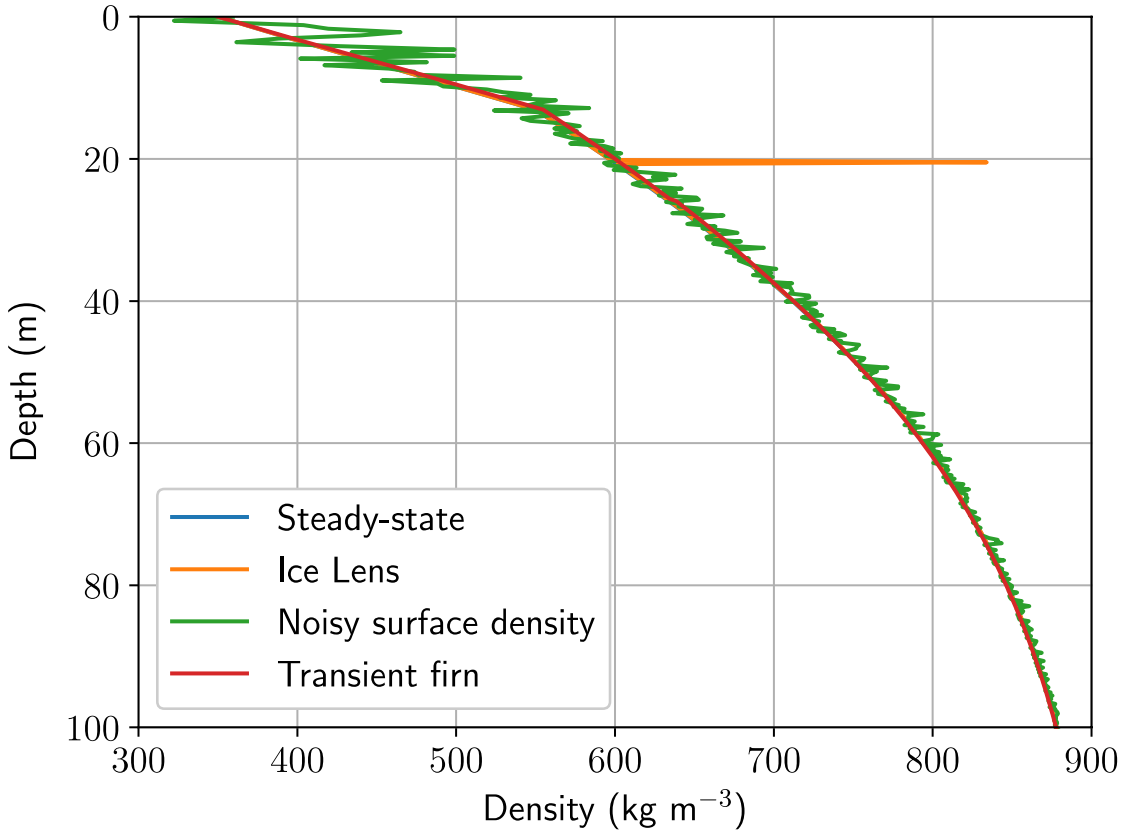

Figure 2.14. Depth-density profile at t=900 years in the model runs described in Chapter 2.6.

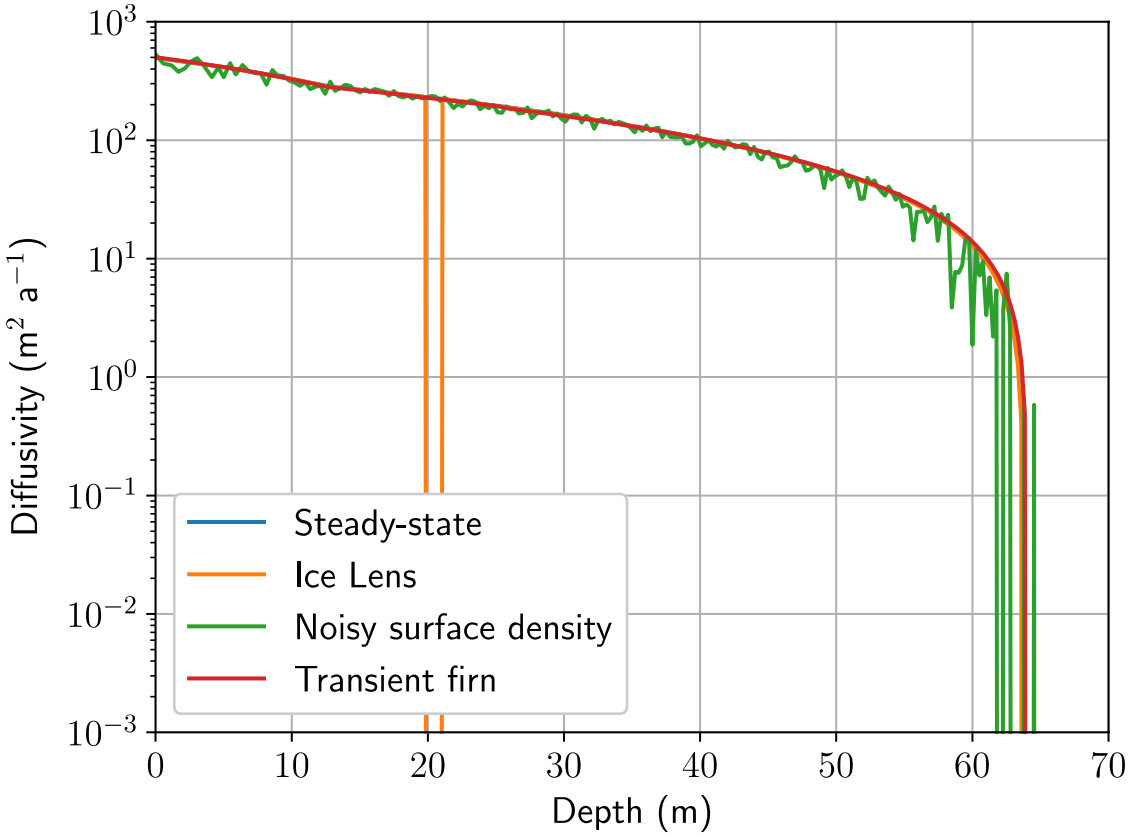

Figure 2.15. Depth-diffusivity profile at t=900 years in the model runs described in Chapter 2.6

Chapter 3. FIRN-MODEL PERFORMANCE AT SUMMIT, GREENLAND USING THE COMMUNITY FIRN MODEL

3.1 ABSTRACT

Firn-densification models are used to (1) correct ice-sheet mass-balance estimates for firn mass changes and (2) to determine the gas-age-ice-age difference (delta age) in ice cores. These models are often based upon a steady-state assumption and are tuned to match depth-density profiles at a number of sites using local accumulation and temperature estimates. Studies that use a firn-densification model often use an a priori assumption that the physics contained in the model are correct, and therefore estimates of uncertainty from firn models is not well known. Previous work has illustrated differences between firn models when those models were forced with synthetic climate data. Here we examine how different models' outputs compare when forced with reanalysis data for Summit, Greenland and how those results compare to measurements. The choice of firn model makes a large difference when predicting the total porosity of the firn and depth of the firn-ice transition, but only a small difference when examining the interannual variations in the porosity. Uncertainties associated with the choice of climate forcing data and surface density are of similar magnitude to those due to firn-model choice. The results shown here can be extended to better quantify error, and sources of that error, in firn-model predictions.

3.2 INTRODUCTION

Snow that falls on ice sheets transitions to ice through an intermediate stage called firn. Knowledge of the physics of firn densification has several applications in glaciology. Ice-core studies require knowledge of the age of the firn at the depth where bubbles of air become trapped in order to determine the difference between the age of air in the bubbles and the firn itself (delta age; Blunier

and Schwander, 2000). Studies of ice-sheet mass balance using altimetry methods require knowing the mass, and mass changes, of the firn to estimate the contribution of the ice sheets to sea-level rise (Shepherd and others, 2012). Both of these applications require a firn-densification model.

Firn is commonly divided by density into three zones based on the dominant physics of densification. The first zone is defined to include the firn from the surface density (often assumed to be ~350 kg m^{-3} in polar regions) to 550 kg m^{-3}. In zone one, densification is usually considered to be due to grain boundary sliding and settling. Zone 2 spans the densities between 550 kg m^{-3} and ~830 kg m^{-3}, and densification occurs due to sintering processes. Around a density of 830 kg m^{-3}, bubbles of air become trapped and further densification is due to deformation of ice around the bubbles, which become compressed and eventually are moved into clathrates.

Various models have been developed to describe the physics of firn densification by numerous research groups. The models are constructed using a variety of methods, but commonly it is assumed that for a given site the accumulation rate is constant and the firn is in steady state. Using this steady-state assumption, known as Sorge's Law, the change in density with depth ($d\rho/dz$) can be converted to a change in density with time ($d\rho/dt$) (Bader, 1954). Using temperature and accumulation-rate data and depth-density profiles from many sites, firn-densification models can be formulated based on temperature (often through an Arrhenius term with a tuned activation energy), accumulation rate (a proxy for stress), and one or more tuning parameters. Notable exceptions to this steady-state tuning include the models of: Arthern and others (2010), who measured firn compaction rates in Antarctica using 'coffee-can' instruments (Hulbe and Whillans, 1994a); Morris and Wingham (2014), who inferred firn-compaction rates from high-resolution density logs; and Arnaud and others (2000), which built upon grain-scale work by Alley (1987) and Arzt (1982), and was further developed by Goujon and others (2003).

The microstructure of firn controls the evolution of its density, but most current firn models are forced at the surface boundary just by the accumulation rate, temperature, and surface density. These fields can come from a regional climate model (RCM), e.g. the Regional Atmospheric Climate Model (RACMO2.3; Noël and others, 2015), Modèle Atmosphérique Régional (MAR; Fettweis and others, 2017), or HIRHAM (Christensen and others, 2007); in-situ weather stations such as the Greenland climate network (GC-Net; Steffen and Box, 2001), or ice-core data (e.g., Buizert and others, 2015). The surface density can be assumed to be constant through time or can be predicted, for example, by using a parameterization based on temperature (e.g. Kuipers Munneke, Ligtenberg, Noël, and others, 2015). Firn models can be coupled to a surface-energy-balance model, but the firn model itself needs only the fields listed above. Firn models have generally continued to use just these forcings, and not more, for two reasons: (1) firn models tuned to the temperature and accumulation rate do a good job of simulating reality despite their simplicity; and (2) historically there has been a dearth of firn microstructure data from polar regions concurrent with full-depth firn cores. Modern instruments such as microCT scanners are changing this paradigm by allowing researchers to view the microstructure of firn in great detail (e.g. Lomonaco and others, 2011; Linow and others, 2012). However, even if the physics of the evolution of some microstructural property are known, a realistic initial condition of that property must still be known in order to model its evolution.

As ice-sheet monitoring and ice-core science progress, firn-densification models are being used to provide high-resolution outputs to explain centimeter-scale changes in surface elevation (Krabill and others, 2002; Shepherd and others, 2018) or decade-scale chronologies in ice cores (Buizert and others, 2015). Both these applications require (1) firn models that can reliably

simulate firn processes at these scales; and (2) a more thorough understanding of the uncertainties associated with firn-densification model outputs.

Here, we focus on answering the following questions: For any location in the dry-firn zone in Greenland or Antarctica, how well do existing firn-densification models agree? How much uncertainty does the use of a firn model introduce into an application, whether that be ice-sheet mass-balance studies or ice-core research? We choose Summit, Greenland as a study location because of the relatively abundant firn data that exist for that site. We do not consider errors due to regional climate model uncertainties or biases; that question has been addressed elsewhere (e.g. Vernon and others, 2013).

To investigate these questions, we use the Community Firn Model (CFM), an open-source model framework developed at the University of Washington, to force a suite of published firn-densification models with regional-climate-model (RCM) data. We examine the variability in model outputs that arises from choice of initial conditions, boundary conditions, and model choice using the metrics of depth-integrated porosity (DIP) and bubble-close-off (BCO) depth. We both intercompare the models (i.e. compare the models' outputs to each other) and compare the model outputs with data from Summit (i.e. compare each model's output with observation).

3.3 METHODS

This work follows the Firn Model Intercomparison Experiment (Lundin and others, 2017), which compared the responses of eight firn models to synthetic temperature and accumulation-rate step changes. Here, we expand upon that work by comparing model outputs from 11 different firn-densification models forced by RCM data. Using the CFM allows us to compare the model physics without the concern of artifacts associated with different numerical methods (e.g. grid size, finite element vs. finite difference, etc.).

An alternative option for our intercomparison would be to use weather-station data from Summit to force the models to test which model can best reproduce the observations; however, most areas of Greenland and Antarctica do not have weather-station data available. Continent-scale calculations of ice-sheet mass balance require an estimation of the DIP over the entire area of the ice sheet, and RCMs are the only means of estimating the climate over the entirety of the ice sheets. Thus, this our results include model uncertainty that is inherent using fields from RCMs.

3.3.1 The Community Firn Model

The CFM is an open-source, modular firn model coded in Python and developed at the University of Washington. The model and its documentation are hosted on GitHub and can be freely downloaded at https://github.com/UWGlaciology/CommunityFirnModel. The CFM includes both firn-physical-property evolution and firn-air models; this work focuses on the firn-evolution model. The core physics of the model track evolution of the firn density and temperature on a Lagrangian grid. The CFM also includes modules to simulate meltwater percolation and refreezing, water-isotope diffusion, firn-air diffusion, and layer thinning due to high horizontal-strain rates. The CFM is forced using surface-temperature, surface-density, and accumulation-rate data. In the wet-firn zone, the model also uses melt data.

The CFM is designed so that additional modules with different physics or processes can be easily integrated. This modular nature allows the user to choose which firn-densification physics to use; what model outputs to save; and which other model physics to include. The firn-densification models available in the CFM and used in this study are those described by Herron and Langway (Herron and Langway, 1980; abbreviated in this study as HL), Barnola and others (1991; BAR), Goujon and others (2003; GOU), Helsen and others (2008; HEL), Arthern and others (2010; ART), Li and Zwally (2011; LZ), Ligtenberg and others (2011; LIG), Vionnet and others

(2012; a.k.a. Crocus, CRO), Simonsen and others (2013; SIM), and Kuipers-Munneke and others (2015; KM). The model abbreviations are also listed in Table 3.1.

For complete descriptions of the models, see the original works, as well as Lundin and others (2017). All of the densification equations have tunable parameters, but most of those parameters are not meant to be altered for a particular model run. Several models have parameters that must be specified for a particular model run; details of the implementation of those model physics in the CFM for this study are in the appendix. Arthern and others (2010) describe two implementations of their model: a complete dynamical model including grain growth, which we refer to as Arthern transient (ART-T), and a model derived from the ART-T using a steady-accumulation assumption, which we refer to as Arthern steady (ART-S). Although the model includes this steady-state assumption, we still run the model in the CFM's transient framework.

3.3.2 Experimental Setup

For all our model experiments, we forced the CFM with monthly output from the RCMs RACMO2.3p2 (Noël and others, 2018) and MARv3.5.2 (Fettweis and others, 2017; ERA-40 and ERA-Interim forcings). RACMO data span the years 1958 to 2016, and MAR data span the years 1958 to 2015.

In order to run a firn-densification model, the model must first be "spun up" to an appropriate initial condition. Here, this initial condition is firn depth-density-temperature profiles for the start of the year 1958. The firn during spin up does not reach true steady state because there is climatological variability in the spin-up forcing data, but the firn does reach a state where the variability in its properties (e.g. porosity) is consistent with a steady-state climate with natural variability. For all of our experiments, we spun up the model for 1000 years, which was long

enough to refresh the entire firn column and also to ensure that the firn had come to thermal equilibrium. Our model domain spanned the surface to ~220 meters depth.

Ideally, the spin-up process would produce a firn density profile that was the true value of the profile in 1958; that is not possible, so the goal is to create an initial condition that is representative of the firn at that time. To do this, we need a climate history for the 1000 years prior to the start of the model run. We generate temperature and accumulation histories for years 958 to 1957. Following Kuipers Munneke and others (2015), we assume that the climate prior to 1978 was in steady state and is representative of the climate for the previous 1000 years. Then, we then use the 1958-1977 period as the climate baseline for model spin up.

One aim of this work is to understand how much uncertainty is derived from the assumption that our initial condition is an accurate representation of the 1958 firn. We ran each of the 11 models with a number of different spin-up climates to test the sensitivity of the models to the initial conditions. Additionally, we ran the models with different climate forcings and surface densities to test model sensitivities to those boundary conditions. All of the model runs were conducted using monthly time steps except for one set of runs that used daily time steps. The model runs and the spin up procedures are described here.

3.3.2.1 Spin-up routines

3.3.2.1.1 Looping-climate spin up

We generated two spin-up climate histories by looping the 1958 to 1978 RACMO temperature and surface mass balance data. For the first, we repeated the 20-year history for 1000 years. We refer to model runs using this spin up as ‘loop20’. For the second, we take the 20-year history and then reverse it to create a 40-year history. That 40-year history is repeated for 1000 years. We refer to these model runs as ‘loop40’. We note that the ‘loop20’ method is how the commonly-used firn

densification model IMAU-FDM (Kuipers Munneke, Ligtenberg, Noël, and others, 2015) is spun up. We then created parallel spin-up histories using the MAR data.

3.3.2.1.2 Monthly constant

We also ran the models using a spin-up climate history in which the values for each month of the spin up were the 1958-1978 mean accumulation rate and temperature for that month; i.e. every January from 958 – 1957 has the same accumulation rate and temperature. We refer to this spin up routine as 'mocon'.

3.3.2.1.3 Ensemble runs

We ran each model 100 times with random spin-up climates. To generate the random climate history, we found the mean and standard deviation of the 1958 – 1978 temperature and surface mass balance for each month and used those values to create normal distributions. We generated temperatures and SMBs for each month 958 – 1957 by randomly drawing a value from those normal distributions. We consider the mean of the model outputs from these ensemble runs, referred to as 'ensmean'.

One deficiency of this method is that temperature is not coupled to accumulation rate, which in reality it is (Alley and others, 1993; Berkelhammer and others, 2016), and one month is not coupled to the next (so it is unlikely for there to be colder-than-average winter, for example). We do not examine the possible biases of this deficiency here. An improved method could randomly choose a temperature, and then randomly choose an accumulation rate from a distribution based upon the temperature. However, the goal of this experiment is to test the sensitivity of the models to the initial conditions, and each of the 100 spin ups does produce a unique 1958 firn profile.

3.3.2.2 Variable surface density

Most of the model runs were done using a constant surface density of 350 kg m^{-3}. To investigate the effect of variable surface density on the model outputs, we ran the models using several different schemes to set the surface density.

For the first variable-surface-density scheme, we used the temperature-dependent parameterization for snow density presented in Kuipers Munneke and others (2015):

$$\rho_s = 481.0 + 4.834T$$

where ρ_s has units kg m^{-3} and T has units ℃. These model runs are referred to as 'param'.

We also generated a time series of surface density for the years 958 to 2016 C.E. by randomly choosing a density from a normal distribution with mean 350 kg m^{-3} and standard deviation 25 kg m^{-3}. These model runs are referred to as 'noise'. Although this method is less physically realistic than the parameterization because it does not couple the surface density to any climatology, it is a useful experiment to examine the sensitivity of the models to the surface density.

For both variable-surface-density scenarios, we initialized each of the models using the 'loop20' spin-up scheme and forced them with RACMO2.3p2 RCM output and added the variable surface density as an additional boundary condition. We did not include the Goujon and others (2003) model in these experiments because the description of that model specifies that the top two meters of firn should be held at a constant density.

To further investigate the effect of different mean surface densities and surface density history, we performed ensemble runs using the Kuipers Munneke and others (2015) model. We ran the model 90 times as described above for the 'noise' scenario with random surface density at each time step drawn from normal distributions (30 runs with mean 350 kg m^{-3} and standard

deviation 25 kg m^{-3}, 30 runs with mean 340 kg m^{-3} and standard deviation 25 kg m^{-3}, and 30 runs with mean 360 kg m^{-3} and standard deviation 25 kg m^{-3}).

3.3.2.3 Daily time steps

We also compared the model outputs when they were forced using daily time steps instead of monthly time steps. These runs were initialized using the 'loop20' spin up and forced with RACMO2.3p2 RCM output. The surface density was held constant at 350 kg m^{-3}.

3.3.3 Model comparison metrics

We compare the model results using several metrics. The depth-integrated porosity, DIP(z), is the air content within the a m^2 firn column (in meters) above depth *z*, given by:

$$\mathrm{DIP(z)} = \int_0^z \phi(z')\, dz' = \int_0^z \frac{\rho_i - \rho(z')}{\rho_i} dz',$$

where ϕ is the porosity, $\rho(z)$ is the density at z, and ρ_i is the density of ice, taken as 917 kg m^{-3} in this work. DIP is the key parameter used to convert volume-change measurements (e.g. surface elevation from altimetry) into mass change for mass-balance calculations. DIP is also referred to in the literature as firn air content (FAC).

When reporting the DIP predicted by a model, it is important to also report the maximum depth (and the corresponding density) to which the firn was modeled, especially if the bottom of the model domain is shallower than the transition to ice, because there could be additional porosity beyond the model domain. It is also important to report the value that is used for pure ice density.

In this study, we consider the DIP in the top 15 m and top 80 m of firn as well as the total DIP through the full depth of the modeled firn; the bottom of our model domain is ~223 m (the depth can vary because the CFM's Lagrangian framework uses a set number of model nodes rather than a set grid), and the firn at that depth was ~916 kg m^{-3}. There is ~5 cm of additional DIP

between the bottom of our domain and the transition to the ice density (917 kg m^{-3}). We use the term DIP throughout our results to describe the total DIP to the bottom of the model domain unless otherwise specified.

We also consider the change in DIP predicted by the models since 1958 and since 2000, which is calculated by subtracting the total DIP at time=1958.0 and time=2000.0 from the total DIP at each time step after 1958.0 and 2000.0.

The bubble-close-off (BCO) depth is the depth at which all porosity becomes closed (versus open and interconnected) and air is occluded in bubbles, and the bubble close-off age is the corresponding age of the firn at the BCO depth. The BCO age is of interest to the ice-core science community, as BCO age is a key parameter for determining delta age. The BCO density is commonly taken to be ~830 kg m^{-3}, but in reality, the BCO depth does not correspond to a particular density. Nevertheless, here we use the 830 kg m^{-3} density horizon for model comparisons of BCO age and depth.

3.3.4 Firn-core data

We compare the model outputs to depth-density data from a firn core retrieved near Summit, Greenland (72.58°N, -38.50°W) in 2007 (Lomonaco and others, 2011). The firn core was drilled to 109.31 m, where the density was 870 kg m^{-3}. The core was sampled at a mean vertical resolution of 7.6 cm. The core density had significant variability (sigma ~ 40 kg m^{-3} in a ~2 m window near the surface; ~ 15 kg m^{-3} at ~80 m depth); we applied a 24-point Hann window to smooth the data.

To calculate the additional DIP beyond the 109-meter depth of the firn core, we used depth-density data from the GISP2 ice core (Alley, 1999). These data begin at 94.3 m and extend to 334 m; we append the GISP2 data from 110 to 220 m to the firn core data for comparison with model output. In the zones of overlap, the GISP2 core density data are ~20 kg m^{-3} greater than the density

measured in the firn core at the same depth. This difference may be real or may be due to different measurement techniques. We do not alter the data to create a smooth transition from one data set to the next.

3.4 RESULTS

Firn-model performance can be assessed by comparing different models forced by the same conditions, or by comparing different outputs produced by the same model but given a range of plausible inputs. When comparing firn models or a models' outputs, one can consider both the differences in DIP and in total DIP. The change in DIP is the quantity of interest for mass-balance studies that need to adjust surface-elevation measurements for interannual variability in firn thickness. Uncertainty in the total DIP is less consequential for these studies. On the other hand, warming in Greenland has extended the wet-firn zone further inland to higher elevations (Abdalati and Steffen, 2001; Mernild and others, 2011); knowledge of the depth-DIP profile is of interest to determine how much meltwater the firn can absorb, or buffer (Harper and others, 2012), or if that water is likely to refreeze and create an impermeable ice slab, which can contribute to increased runoff (Machguth and others, 2016). This effect is most important in the near-surface firn because meltwater is unlikely to percolate to the full depth of the firn column in areas that are undergoing melt for the first time; the cold-content of the firn refreezes water near the surface.

3.4.1 Model Intercomparison

3.4.1.1 Depth-density and depth-DIP profiles

Figure 3.1 shows depth-density profiles and Figure 3.2 shows depth-DIP(z) profiles predicted by the various models, as well as those measured in the firn core. The model profiles plotted are those predicted for June 2007 using the RACMO2.3p2 data with the 'Loop20' spin-up routine.

Table 3.2 lists the values of DIP from the surface to depths of 15, 80, and 200 m as well as the depth and age of the 830 kg m^{-3} density horizon for all of the models. It also shows the mean and standard deviation of the models' results and the values from the 2007 firn core (in the row labeled Core). The measured BCO depth at Summit is ~80 m (Witrant and others, 2012), and the age of the firn at this depth is ~235 years (Meese, 1999). Each column in the Core row features two values: the first is the value calculated using the full-resolution core data; the second is the value calculated after smoothing the core data. The "model mean" and "model std" rows similarly have two values each: the first is the mean and standard deviation including the results from CRO; the second is these statistics excluding CRO. CRO was developed for seasonal snow, and it does not predict firn densification well in deeper firn. This is consistent with results from Lundin and others (2017), who also demonstrated that snow models do not predict densification well in deeper (zone 2) firn.

Near the surface (zone 1 densification, <~15m depth), the models generally agree with one another and match the DIP in the core to within several tens of centimeters; this behavior is expected because they all start with the same surface boundary condition (i.e. DIP(0 m) = 0; ρ_s=350 kg m^{-3}). Compared with the measurements, all models except HEL predict densities that are too high and DIPs that are too low. GOU and ART-S in particular both predict a lesser DIP/greater density than measured. This pattern is surprising considering that GOU was formulated for the cold, low-accumulation interior of Antarctica, and ART was formulated using data from relatively warm, high accumulation sites near the Antarctic peninsula.

Through zone 2, the models diverge in their predictions. All of the models except CRO predict densification that is too fast, resulting in the predicted DIP being less than observed. ART-S in particular densifies too quickly. CRO fails to densify quickly enough through zone 2, resulting

in a high predicted DIP. This behavior is perhaps not unexpected because CRO was developed as a seasonal snow model and therefore is not able to accurately predict densification of higher-density firn. Beyond 80 m CRO continues to densify too slowly, resulting in a very high DIP at 200 m and a BCO depth and age of 210 m and 774 years respectively. Excluding CRO, the models' DIP at 200 m has a standard deviation of 2.79, or roughly 10% of the total DIP.

KM matches the data best using the metrics of DIP at 200m and depth of the 830 kg m^{-3} density horizon. This is not a surprising result because KM was developed by forcing ART-S with RACMO data and adding tuned coefficients to the model to match firn-core observations from Greenland, including one core from a site near Summit.

HL best predicts the BCO age, though it underestimates the BCO depth. Other models that predict BCO age close to the observation show similar behavior; e.g. both SIM and LZ predict BCO age within 10 years of the measured age, but both have BCO depths much shallower than measured in the core. Aside from CRO, KM is the only model to predict a BCO age older than observed, though its predicted BCO depth is still shallower than observed. This consistent mismatch of BCO depths and ages suggest that the sensitivities of firn models to accumulation rate and temperature may be systematically incorrect.

In several of the modeled depth-density profiles, notably the ART-S profile, a memory of the 20-year looping spin up is still evident, though this does not significantly affect the results (Chapter 4.2).

3.4.1.2 DIP through time

Figure 3.3 shows changes in the DIP through time predicted by the models since 1958 (top panel) and since 2000 (bottom panel). The models were forced with RACMO2.3p2 data and we used the 'loop20' spin up routine.

All models predict that DIP has increased since 1958. The mean change at the end of the model run is +0.10 m, and the standard deviation is +0.046 m. LZ shows the smallest change of +0.037 m, and CRO predicts the largest change of +0.16 m.

The spread among modeled total DIPs is several meters, but the spread in the modeled DIP changes is only on the order of ten centimeters. However, the coefficient of variation, $\frac{\sigma_{DIP}}{\overline{DIP}}$, for the total DIP in 2007 is 35% (14%) with (without) CRO, while the coefficient of variation for the change in DIP 1958-2016 is 45%. This result indicates that though the magnitude of DIP changes is small, the models do not agree well with one another when predicting transient firn responses.

It is also notable that there are times at which the DIP changes since 1958 predicted by the various models have opposite signs from one another, such as in early 2014 when LZ and ART predict a negative change in DIP while the other models predict a positive change. The models are also not consistent through time relative to one another; for example, HL predicts the second-most negative change at time = 1983, but then the second-most positive change at time = 2011.

The models all predict an increase in DIP during the late 1990s. This is due to above-average accumulation for several years during this period. The increased accumulation adds more low-density firn near the surface, which results in increased DIP.

All the models except KM predict a DIP decrease from 2000 to 2016; KM predicts a very small (0.2 cm) increase (Figure 3.3, top). Most models predict a 0 – 5 cm decrease in DIP, but the HEL, LZ, and ART-T models predict decreases of 8.3, 18.2, and 21.5 cm, respectively. Similar to the predicted DIP change since 1958, there are times (e.g. mid-2010) that numerous models predict a positive change in DIP since 2000, when others predict a negative change. For example, at time=2010.7, KM predicts a net DIP change since 2010 of +4.8 cm while LZ predicts a -3.8 cm net change. This discrepancy means that at certain times, some models predict the surface-

elevation correction from firn changes should be a subtraction, while other models predict it should be an addition.

3.4.2 Model sensitivity to initial and boundary conditions

Figure 3.4 shows the DIP through time, Figure 3.5 shows the change in DIP since 1958, and Figure 3.6 shows the DIP change since 2000 predicted by the 11 models using different spin-up scenarios, surface-density parameterizations, and time-step sizes. Table 3.3 and Table 3.4 show the change in DIP since 1958 and 2000, respectively, for all of the models and spin-up scenarios.

3.4.2.1 Initial conditions

The blue line in Figure 3.4 shows the mean DIP of the ensemble runs, and the light blue is the one-sigma envelope of DIP for the ensemble runs. The one-sigma envelope shrinks through time because as time passes, a shrinking proportion of the firn column is made up of firn that was deposited prior to 1958 (the end of the spin up). That is, the DIP was different for each of the 100 ensemble runs at t=1958, but after 1958 the ensemble runs are the same, and therefore the variability in DIP is reduced. The red, green, and olive lines show the results of the 'monthly constant', 'loop40', and 'loop20' spin ups, respectively.

The choice of these spin ups makes a small difference in the total DIP. For all of the models, the standard deviation of the ensemble runs is several mm, where the total DIP is on the order of 20 m. The 'monthly constant', 'loop40', and 'loop20' results are also within several mm of the ensemble mean. When initialized with the 'loop20' and 'loop40' routines, the family of models based on the ART-S model (ART-S, KM, LIG, SIM), as well as the LZ and HEL models, all consistently predict DIP less than the ensemble mean and are occasionally outside of the 1-sigma envelope.

The differences in model-predicted change in DIP since 1958 are more substantial. Table 3.3 shows the change in total DIP since 1958 at the end of the model run (2016). KM predicts DIP increases of 12.7, 11.3, 18.7, and 15.0 m for the ensemble mean, monthly constant, 'loop40', and 'loop20' spin-up schemes, respectively. Although these are relatively small numbers, especially when compared to the total DIP (order 20 m), the 'loop40' spin up results in a 47% greater change in DIP since 1958 than the ensemble mean. Other models are less sensitive to the initial condition produced by the spin up; for example, HL's predicted DIP changes are all within 3.1 cm of each other. For all of the models, the monthly constant spin up produced predicted DIP changes less than those by the ensemble mean. For the two looping spin ups, some models predicted larger DIP change than the ensemble mean and some smaller, though for all models the predicted DIP change using the 'loop40' spin up is greater than that of the 'loop20'.

The change in DIP since 1958 through time from the various spin ups is similar to the result at the end of the model run; i.e. the various spin ups predict similar patterns of increase and decrease of DIP (Figure 3.5). There are times, however, when one model run predicts an increase in DIP since 1958 where others predict a decrease (e.g. in the mid-1990s, KM spun up with 'loop40' predicts a small positive value, but the 'ensemble mean' run predicts a small negative change; Figure 3.7, top).

Figure 3.6 shows the time series of DIP change since 2000, and Table 3.4 shows the net change in DIP 2000-2016. The four monthly-time-step spin ups all show very similar changes in DIP since 2000 because the near-surface firn, where much of the DIP variability comes from, is the same. (The firn that was deposited in 1958 is at ~23 m depth at the end of the model run.)

3.4.2.2 Variable Surface Density

The model runs discussed above had a fixed surface density of 350 kg m^{-3}. The tan and brown lines in Figures 3.4, 3.5, 3.6, and 3.7 show the results of the model runs that included a time-varying surface density. The brown line is the result of using the parameterization for temperature-dependent surface density presented in Kuipers Munneke and others (2015), and the tan line shows the results from a model run where the surface density at each time step was drawn from a normal distribution with mean 350 kg m^{-3} and standard deviation 25 kg m^{-3} (the 'noise' run). The runs with variable surface density were all initialized using the 'loop20' spin-up routine. We did not perform the variable-surface-density runs with the GOU model because that model specifies that the top 2m of firn should be held at a constant density.

For all of the models, using the temperature-dependent surface-density parameterization results in greater DIP than with the other runs. This is because the mean surface density using the parameterization is slightly lower (~347 kg m^{-3}) than the constant value. Most of the models predict 0.2 – 0.3 m more DIP using this surface-density scheme than using the constant density, with the exception of the BAR model, for which the DIP is nearly the same (Figure 3.4). When using the 'noise' surface density, the DIP through time is within a few mm of the mean of the ensemble runs; at certain times it is slightly greater and at other times it is slightly less due to the fact that the surface density at each time step is random.

The effect of the variable surface density on the predicted DIP changes varies by model. For the all of the models, the change in DIP from 1958 to ~2000 predicted by the model runs with variable surface density is similar to that predicted by the constant-surface-density model runs (Figure 3.5). For several of the models, the 'noise' model runs predict that from ~1990 to 1995 there was a net DIP decrease since 1958, where the constant-density runs predict a near-zero or positive change. This is because of red noise in the surface-density time series.

From 2000 to 2016, all of the models predict a larger DIP decrease when forced with the temperature-dependent surface-density parameterization compared to the constant density (Figure 3.6; Table 3.4). BAR and CRO predict only small changes (-0.068 and -0.055 for 'param' vs -0.048 and -0.029 for the ensemble mean.) The other models predict larger negative changes overall; for example, KM predicts a DIP decrease of -8.2 cm with 'param' vs. -0.3 cm with the ensemble mean; LZ predicts a DIP decrease of -18.2 cm with 'param' vs. -11.5 cm for the ensemble mean.

The 'noise' model runs do not consistently predict a DIP increase or decrease for 2000-2016, though the net change for each model is greater than the ensemble mean for that model. In some cases (e.g. SIM and KM), the 'noise' runs predict a positive change in DIP (4.2 and 6.3 cm), whereas the 'param' runs predict a negative change (-9.3 and -8.2 cm).

Figure 3.8 shows the mean and standard deviation of the DIP (top panel) and mean change in DIP since 2000 (bottom panel) for the 90 KM model runs with variable surface density. Figure 3.9 shows the change in DIP since 1958 and Figure 3.10 shows the change in DIP since 2000 for the variable-density ensemble runs; the bold colors are the mean of the 30 ensemble runs with mean densities 350 kg m^{-3} (red), 360 kg m^{-3} (green), and 340 kg m^{-3} (blue); the light colors are the results of the individual model runs. The bold lines in Figure 3.9 and Figure 3.10 show the same DIP time series as the matching colors in the bottom panel of Figure 3.8.

The mean of the ensemble runs with mean surface density 350 kg m^{-3}, and the mean change in DIP predicted by all three ensembles, are similar to the 'loop20' model run results because the surface-density variability averages out. The DIP predicted by the mean of the 350 kg m^{-3} ensemble is slightly greater than the 'loop20' DIP because low-density layers push DIP greater to a larger

degree than high-density layers push the DIP lesser As expected, the lower mean surface density results in greater DIP, and the higher mean surface density results in less DIP.

Although the mean DIP changes from the variable density ensembles are similar to the 'loop20' results, the changes in DIP predicted by individual runs in the ensemble are variable. While the mean DIP change since 2000 is near zero, some runs predict a net change of +10 cm, while others predict a net change of -10 cm.

3.4.2.3 Time-step size

The purple lines in Figures 3.4, 3.5, 3.6 and 3.7 show model results using daily time steps; all of the other model runs were using monthly time steps. Most of the models predict a greater DIP when forced with daily data. This is a result of heat transfer. Daily temperature data include cold days and weeks that are averaged out in monthly data. Cold firn is more conductive than warm firn, so firn temperatures modeled using daily data are slightly colder (0.3 K at 50 m depth) than when using monthly data. The magnitude of the differences in firn compaction between the daily and monthly time-step runs varies by model because the models have different temperature sensitivities and thus different responses to the colder firn.

ART-T has significantly less total DIP with the daily time steps. This is because the grain-growth term in ART-T also has a temperature dependence. The slightly colder firn results in slower grain growth. Smaller-grained firn densifies faster than larger-grained firn, and so the model predicts denser firn despite the fact that it is slightly colder. HEL shows a similar behavior because it also includes a grain-growth term; however, the DIP predicted by HEL when forced with daily data is only slightly less than DIP with the monthly data.

The daily time steps do not make a significant difference in the modeled DIP change since 1958 for any of the models. The change in DIP for daily time steps is within a few mm of the monthly ensemble mean runs; it is sometime above and sometimes below.

3.4.3 Model sensitivity to RCM forcing

Figure 3.11, Figure 3.12, and Figure 3.13 compare the model-predicted DIP, DIP change 1958-2015, and DIP change 2000-2015, respectively, when the models are forced with the different RCM products. The solid lines are the model results from using RACMO forcing data, and the dashed lines are the results from using MAR forcing data. Table 3.5 lists the mean DIP over the model run and the net DIP changes 1958-2015 and 2000-2015 for both sets of forcing data. Both sets of results were produced using the 'loop20' spin-up routine and monthly time steps.

Using the MAR data predicts a greater total DIP for all models. This is because the MAR temperature data is slightly colder than the RACMO temperature, which causes the firn to not densify as quickly, and the MAR SMB is slightly greater than the RACMO SMB, which causes the thickness of the firn to increase. These differences between the MAR and RACMO forcing data also leads to a deeper BCO depth; for example, the BCO depth predicted by KM when forced with MAR data is ~80 m vs ~74 m with RACMO forcing. The BCO age is nearly the same (246 years with MAR vs 248 years with RACMO).

Using the MAR forcing data results in a slightly lesser change in DIP since 1958 compared to RACMO forcing data (Figure 3.12). All of the models predict a net positive change in DIP since 1958 when forced with RACMO data, but five of the models predict a net negative change when forced with MAR data. The magnitude of the differences varies by model, which reflects the differences in model sensitivities to temperature and accumulation rate. The change in DIP since 1958 through time is not constant; i.e. there is not a constant offset between the lines in Figure

3.12. For example, during the late 1970s the net change is nearly the same using both types of forcing data for all of the models. The change through time predicted using MAR data is nearly always less than the change predicted when using RACMO data.

All of the models with both climate forcings predict a net decrease in DIP between 2000 and 2015 (Figure 3.13). All of the models predict larger decreases when forced with RACMO data rather than with MAR data. Similar to the 1958-2015 DIP change, the magnitude of the change varies by model. The difference is smaller (~2 cm) for the models based on ART-S (ART-S, SIM, KM, LIG), whereas the difference for LZ and HEL is ~5 cm. Unlike the 1958-2015 DIP change, there are numerous times when the change in DIP since 2000 predicted with RACMO forcing is greater than that predicted with MAR forcing, such as the year 2008.

3.4.4 Firn model uncertainty

In general, most of the models predict too low of DIP(z) throughout the depth of the firn column at Summit. Additionally, the models that predict a close-off age closest to the measured age (KP, HL, LZ) all predict too shallow of a close-off depth. Both of these results indicate that the firn models predict densification that is too fast, which is likely due to incorrect tuning of the temperature and stress dependences in the models.

Our results show that the model choice is a significant source of uncertainty when considering the total DIP. In the top 15 m, the standard deviation of the DIP predicted by the models is 7% of the mean; for the full firn column it is 14% (excluding CRO). The model choice is a relatively smaller source of uncertainty when considering the *change* in DIP. The models generally agree on interannual variability in DIP to within several cm; the measured interannual variability in surface elevation at Summit is on the order of 1 meter (Zwally and Li, 2002).

The aggregate differences in interannual DIP changes amount to slightly more uncertainty: the standard deviation of the change in DIP 2000-2016 among the models is 4.4 cm using the 'loop20' spin up; if we assume that represents the uncertainty due to model choice over a dry-snow zone of $7.7x10^5$ km^2 (De La Peña and others, 2015), the uncertainty in the change in DIP 2000-2016 for the dry-snow zone is 33.88 km^3, equivalent to 31 Gt of ice, or 1.8 Gt/year. For comparison, McMillan and others (2016) reported that Greenland lost mass at a rate of 269 +/- 51 Gt per year between 2011 and 2016.

Regardless of the model, the climate-forcing data and the surface density are significant sources of uncertainty, and these uncertainties have a magnitude similar to those associated with model choice. This underscores a general truth of any model: the model output is only as good as the data that go into the model. The size of the uncertainties that come from input data uncertainty (both surface density and climate forcings) suggests that our ability to accurately simulate firn evolution is not just limited by an incomplete understanding of the physics of firn densification. The surface density presents a unique challenge because it is not a well-known quantity; parameterizations for surface density do exist, but those are not universally accepted, and data to constrain such parameterizations are sparse. Furthermore, the variability of surface density on sub-annual timescales is known even less well.

Our results show that relatively small uncertainty in the surface density can result in a significant uncertainty in the change in DIP.

The model spin-up procedure, which provides an initial condition, makes only a small difference in the model results, and the difference will continue to get smaller in the future as less of the modeled firn will have been deposited in the pre-RCM-data years (i.e. we will have greater confidence in the accumulation-rate and temperature history of an increasing proportion of the

firn). The change in DIP through time is not very sensitive to spin up because the DIP variability is in the near-surface (high-porosity) firn, which is the same regardless of spin up. The looping-spin-up essentially adds memory into the firn, but this memory has a negligible effect on the model output that we use. Using daily rather than monthly model time steps, however, does make a significant difference in the total DIP and a smaller but notable difference in how the DIP changes through time, especially for some models. This result could be a particular nuance of the numerical implementation of the CFM, or it could be a robust result that would be predicted by any model framework.

3.5 DISCUSSION

Our modeling results demonstrate challenges that the firn-modelling community continues to face: despite the number of firn-densification models that have been proposed, no single model is widely accepted. We ran 11 models, and the models agree neither in total DIP nor in how the DIP changes through time. Lundin and others (2017) showed that firn models do not agree when predicting steady-state or transient behavior when forced with synthetic climate, and our results corroborate those results.

Our investigation focuses on a single location, Summit, Greenland, which we chose because it is a well-studied site. The fact that the models do not agree at Summit does not necessarily mean that they would not agree at other sites, but agreement is unlikely. If one model performs best at Summit, it does not necessarily indicate that that model is the "best firn model". Indeed, it may be the best model for Summit, but it may not work as well at other locations, and it is not clear where one model is better than another.

A number of arguments could be made as to why it is inappropriate to compare these models, especially at a single site in Greenland. For example, some of the models are potentially

outdated and not in use any longer, certain models were tuned for a particular place and may not be appropriately applied to Summit, and some models were intended for ice-core delta-age reconstruction rather than mass-balance corrections, or vice versa. Regardless, each of these models was at one point the state of the art, and they were all designed to simulate the same properties of the firn. If the physics are correct and complete, a firn model should be able to simulate firn evolution accurately on all time scales and all spatial scales.

We also note that LIG and KM were both developed by forcing ART-S with RACMO data (the former for Antarctica; the latter for Greenland) and tuning the model to match measured depth-density profiles, including a site near Summit; we would therefore expect KM to perform well at Summit when forced by RACMO data. It is interesting that the total DIP predicted by KM when forced by MAR data is closer to the value inferred from the firn core than when the model is forced by RACMO data.

Tuning a model using a measured depth-density profile inherently invokes a steady-state assumption, and this assumption is built into nearly all of the models here. Developing a model using a steady-state assumption is limiting because the set of parameters that can be tuned to fit a depth-density profile is not unique; for example, the fact that most models in this study are predicting too-rapid densification indicates that the models are too sensitive to temperature and not sensitive enough to stress, or vice versa. Historically, modelers have tackled this issue by using cores from a variety of temperature and accumulation-rate regimes.

Using models with an underlying steady-state assumption to simulate transient firn evolution is potentially problematic because (1) there is a non-unique set of temperature and accumulation histories that could lead to a particular firn depth-density profile and (2) a single firn depth-density profile does not provide information about how the firn evolves in a transient

climate. A transient climate in this case means a climate change over a timescale shorter than the lifetime of the firn, and we include sub-annual and interannual variability in this definition. In firn-model applications considering slow-changing climate, such as many ice-core applications, the steady-state assumption may be appropriate. In applications considering annual and seasonal variability and short-term climate change, it is not clear that the underlying physics of steady-state physics are correct.

Our results demonstrate a need to improve our understanding of firn-densification physics, which may include both validation of existing models and development of new models. Unfortunately, there is still a dearth of data that is needed for the development of a purely physically-based model; any model development in the near future is likely to necessitate a certain amount of empirical tuning. A microstructure-based firn-densification model will need empirical parameterizations for evolution of the microstructural properties. The addition of descriptions of physical processes such as grain growth to a model does not necessarily result in a better model if those physics (and the initial and boundary conditions) are not well constrained. For example, ART-T includes grain growth, but it does not necessarily produce better results.

An alternative approach is to focus modeling efforts on getting the ‘right’ answer without being concerned with whether the model represents all of the underlying physics correctly. These modelling efforts can be improved by using firn-compaction-rate data rather than just depth-density profiles (e.g. Arthern and others (2010) and Morris and Wingham (2014)), which underscores the need for field measurements.

Ultimately, research should be done to both further our understanding of the microstructural evolution and underlying physics of firn evolution as well as to improve empirical models.

3.6 CONCLUSIONS

We developed the Community Firn Model (CFM), an open source firn-model framework, and we used it to run a suite of firn-densification models to simulate firn evolution at Summit, Greenland using a variety of initial and boundary conditions. These simulations show that there are numerous sources that contribute to uncertainty in firn-model outputs. The uncertainty in predicting the total DIP of the firn is ~10%, and the uncertainty in predicting the depth and age of the firn-ice transition is greater than 10%. The uncertainty in the interannual variation in DIP is relatively small compared to the magnitude of interannual surface elevation changes and the total uncertainty of Greenland ice-sheet mass loss. Still, continued work to improve and validate firn models is necessary because the small interannual uncertainties sum to larger uncertainties over time.

This study focused on the dry-firn zone, but future work also needs to improve our understanding of how the presence of meltwater in firn affects the firn-compaction rate, especially as the region of Greenland that is subject to melt is expanding in a warming climate.

Table 3.1. The 11 models used in this study and the abbreviations used throughout the text. Note that the Arthern and others (2010) model has two formulations (see Chapter 3.3.1).

Model Name/Reference	Abbreviation
Herron and Langway (1980)	HL
Barnola and others (1991)	BAR
Goujon and others (2003)	GOU
Helsen and others (2008)	HEL
Arthern and others (2010)	ART-T, ART-S*
Ligtenberg and others (2011)	LIG
Li and Zwally (2011)	LZ
CROCUS (Vionnet and others, 2012)	CRO
Simonsen and others (2013)	SIM
Kuipers Munneke and others (2015)	KM

Table 3.2. Comparison of the model results to firn core data. The values reported here in the Core row are for the raw/smoothed data. The depth (age) of the 830 kg m^{-3} density horizon is much deeper (older) with the smoothed data because that horizon in the raw data is the first depth at which the density is greater than 830 kg m^{-3}, whereas in the smoothed data it is the depth at which the average density becomes 830 kg m^{-3}. The model mean and model std rows are with/without CRO included in the statistic.

	DIP15 (m)	DIP80 (m)	Total DIP (m)	DEP830 (m)	AGE830 (a)
Core	7.64/7.66	22.67/22.70	25.3/25.29	66.57/79.52	190/238
HL	7.42	20.47	22.91	71.83	239.50
HEL	8.08	22.06	23.56	66.96	211.08
ART-S	6.34	14.11	14.59	47.10	159.00
ART-T	7.33	17.34	18.14	55.38	181.92
SIM	6.73	16.64	17.67	56.46	190.17
LIG	7.16	18.20	19.48	61.00	203.08
BAR	6.99	19.89	20.60	68.19	226.50
LZ	7.10	19.67	21.99	69.94	235.08
GOU	6.30	17.86	19.50	62.08	209.33
CRO	7.15	24.58	45.73	210.23	774.08
KM	7.39	20.92	23.65	74.43	248.92
model mean	7.09/7.08	19.25/18.72	22.53/20.21	76.69/63.34	261.70/210.46
model std	0.51/0.53	2.85/2.35	8.18/2.92	45.03/8.54	172.02/28.12

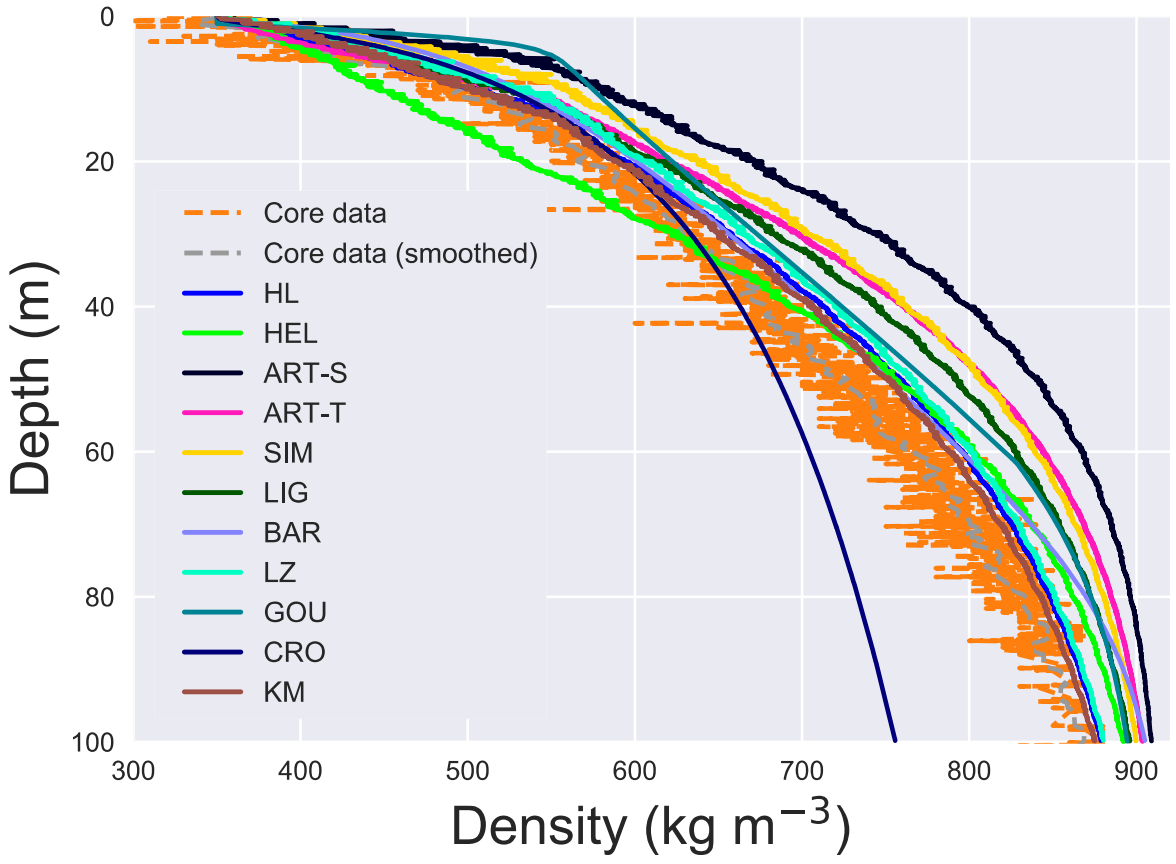

Figure 3.1. Depth-density profiles predicted by the 11 models and measured on a firn core (Lomonaco and others, 2011)

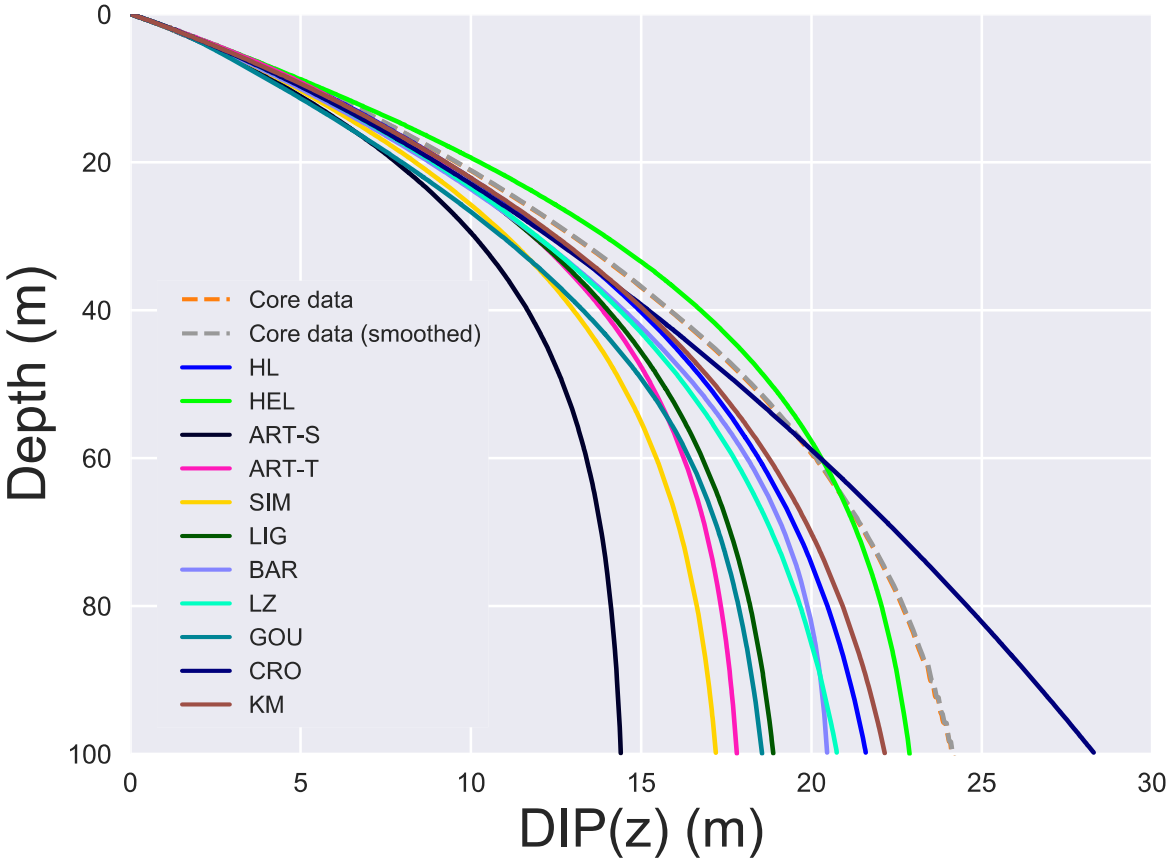

Figure 3.2. Depth-DIP(z) profiles predicted by the 11 models and measured on a firn core (Lomonaco and others, 2011)

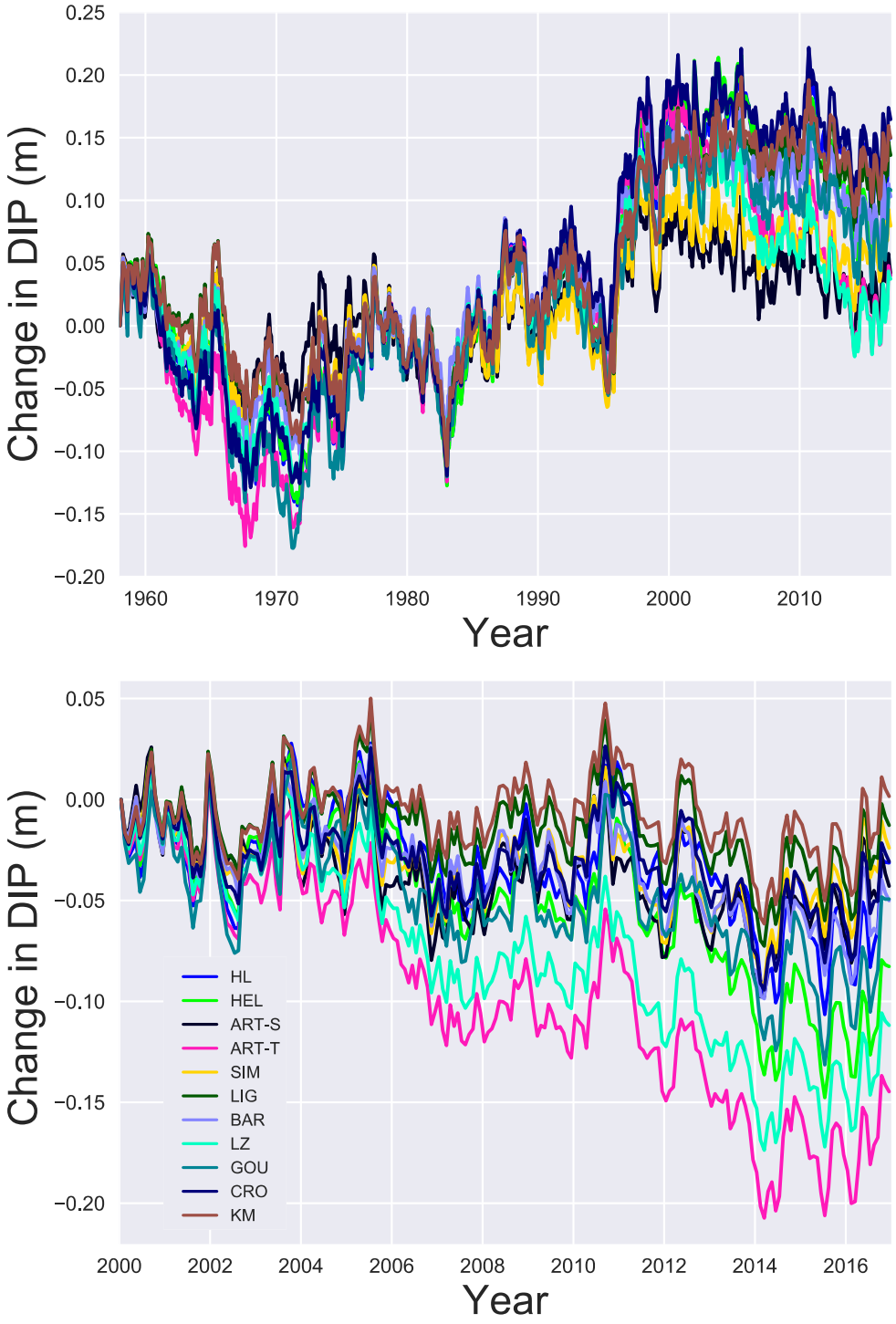

Figure 3.3. Change in DIP predicted by the models since 1958 (top panel) and 2000 (bottom panel). Note that the vertical-axis scales are different.

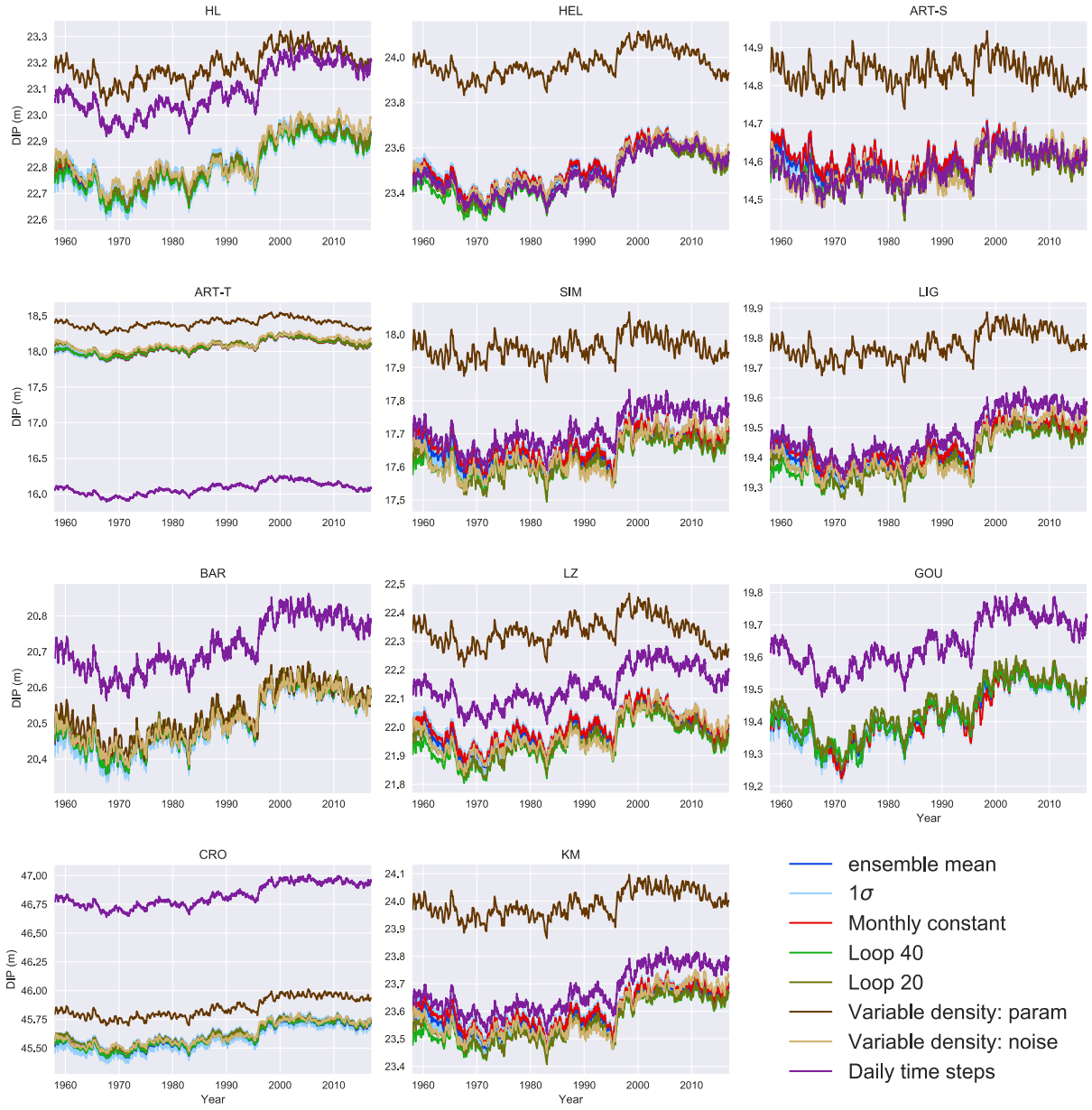

Figure 3.4. DIP through time predicted by the models using different initial and boundary conditions. The brown and tan lines use a different surface density; all other colors use the same surface density (350 kg m^{-3}) at every time step.

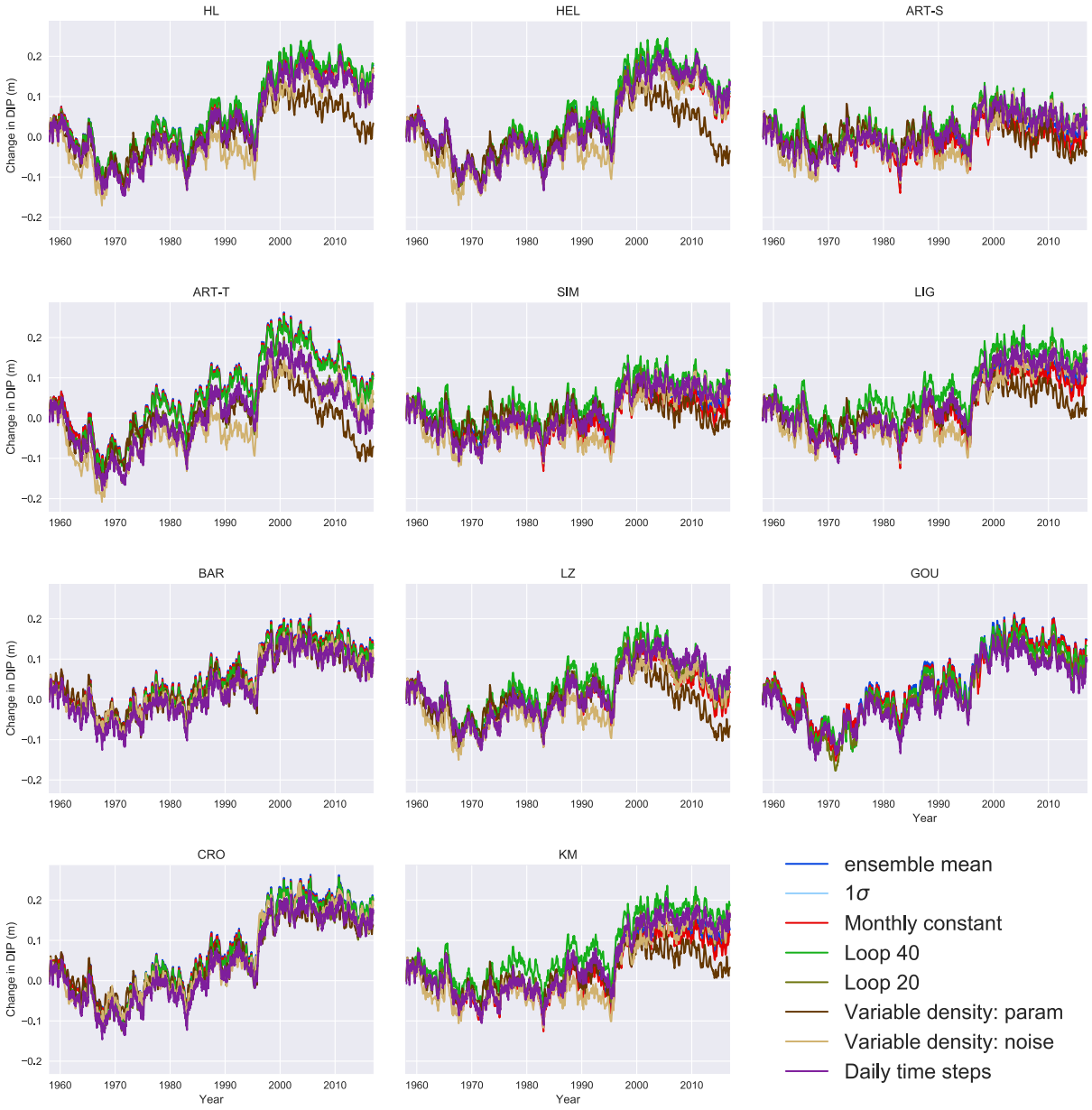

Figure 3.5. Change in DIP since 1958 predicted by the models using different initial and boundary conditions. The brown and tan lines use a different surface density; all other colors use the same surface density (350 kg m^{-3}) at every time step.

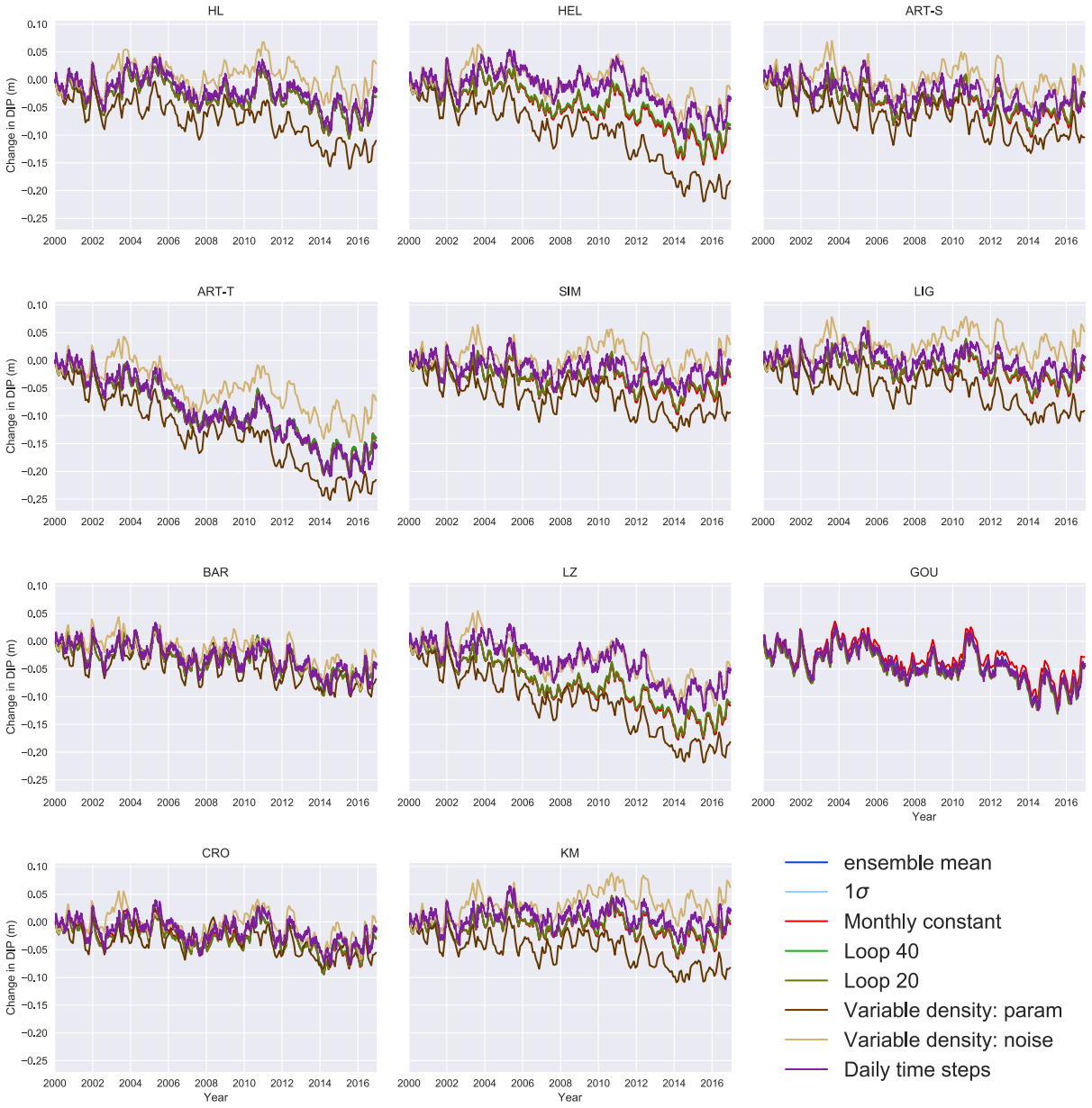

Figure 3.6. Change in DIP since 2000 predicted by the models using different initial and boundary conditions. The brown and tan lines use a different surface density; all other colors use the same surface density (350 kg m^{-3}) at every time step.

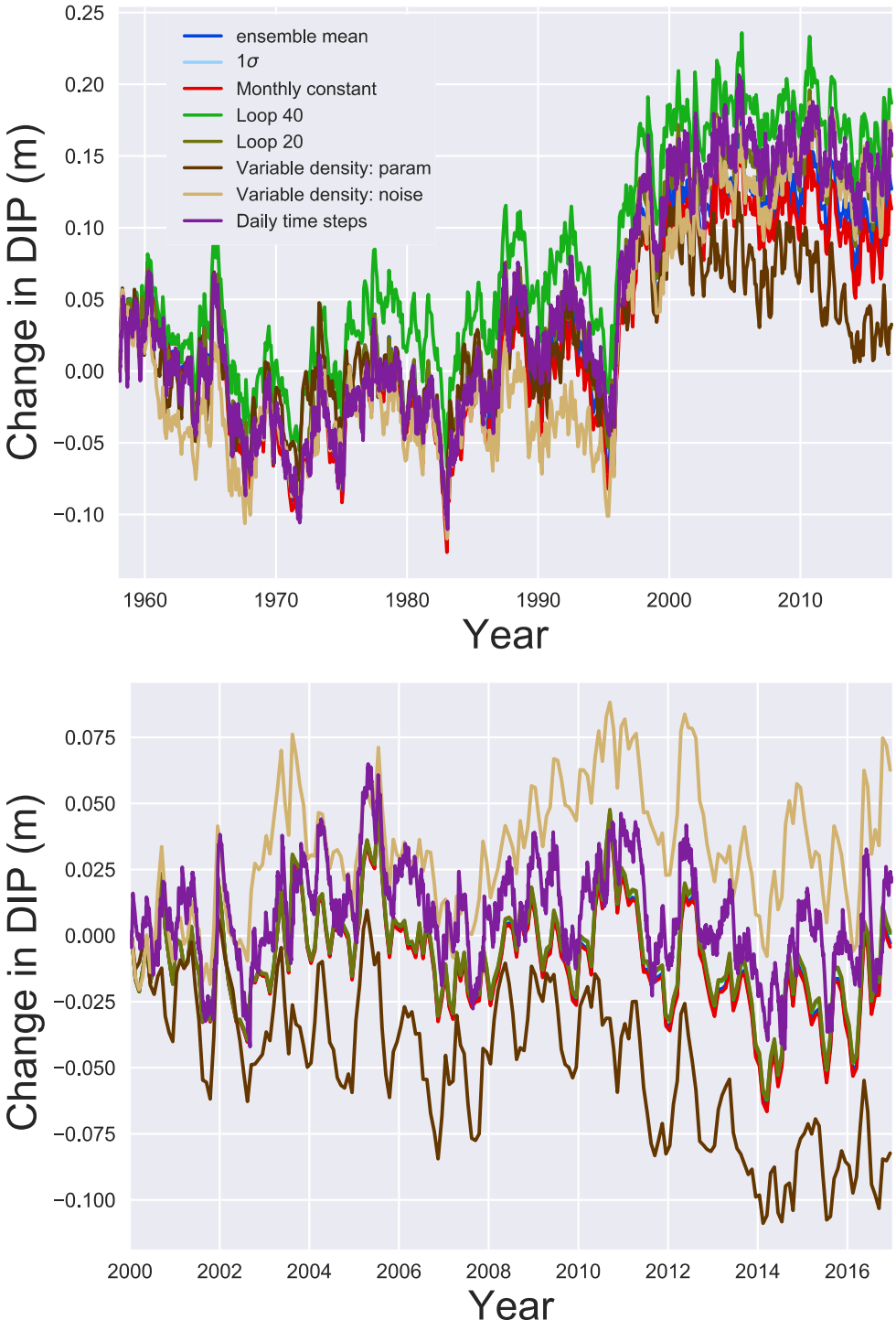

Figure 3.7. Change in DIP predicted by KM since (top) 1958 and since (bottom) 2000 using the different initial and boundary conditions. As in Figures 3.5 and 3.6, but zoomed into the KM model results.

Table 3.3. Change in DIP in meters predicted by the various models for 1958 – 2016 using the different boundary and initial conditions.

	ensmean	mocon	Loop40	loop20	param	noise	daily
HL	0.178	0.170	0.181	0.150	0.034	0.187	0.148
HEL	0.112	0.100	0.139	0.108	-0.034	0.146	0.131
ART-S	0.018	0.003	0.057	0.042	-0.038	0.075	0.050
ART-T	0.107	0.103	0.097	0.040	-0.070	0.093	0.015
SIM	0.060	0.044	0.106	0.080	-0.008	0.088	0.091
LIG	0.116	0.101	0.172	0.136	0.024	0.181	0.145
BAR	0.137	0.134	0.127	0.103	0.088	0.119	0.099
LZ	0.031	0.017	0.065	0.037	-0.066	0.081	0.077
GOU	0.149	0.147	0.133	0.108	0.023	0.073	0.095
CRO	0.203	0.198	0.200	0.165	0.138	0.187	0.171
KM	0.127	0.113	0.187	0.150	0.033	0.186	0.162

Table 3.4. Change in DIP in meters predicted by the various models for 2000 – 2016 using the different boundary and initial conditions.

	ensmean	mocon	Loop40	loop20	param	noise	daily
HL	-0.030	-0.031	-0.029	-0.031	-0.110	0.029	-0.020
HEL	-0.087	-0.089	-0.080	-0.083	-0.183	-0.017	-0.034
ART-S	-0.048	-0.049	-0.043	-0.043	-0.104	0.007	-0.024
ART-T	-0.139	-0.139	-0.140	-0.145	-0.215	-0.072	-0.156
SIM	-0.029	-0.031	-0.025	-0.024	-0.094	0.029	-0.001
LIG	-0.017	-0.018	-0.013	-0.013	-0.091	0.052	0.005
BAR	-0.048	-0.048	-0.048	-0.050	-0.068	-0.028	-0.042
LZ	-0.115	-0.117	-0.110	-0.112	-0.182	-0.045	-0.052
GOU	-0.041	-0.028	-0.046	-0.049	-0.065	-0.151	-0.045
CRO	-0.029	-0.030	-0.028	-0.031	-0.055	-0.001	-0.014
KM	-0.003	-0.004	0.001	0.002	-0.082	0.063	0.021

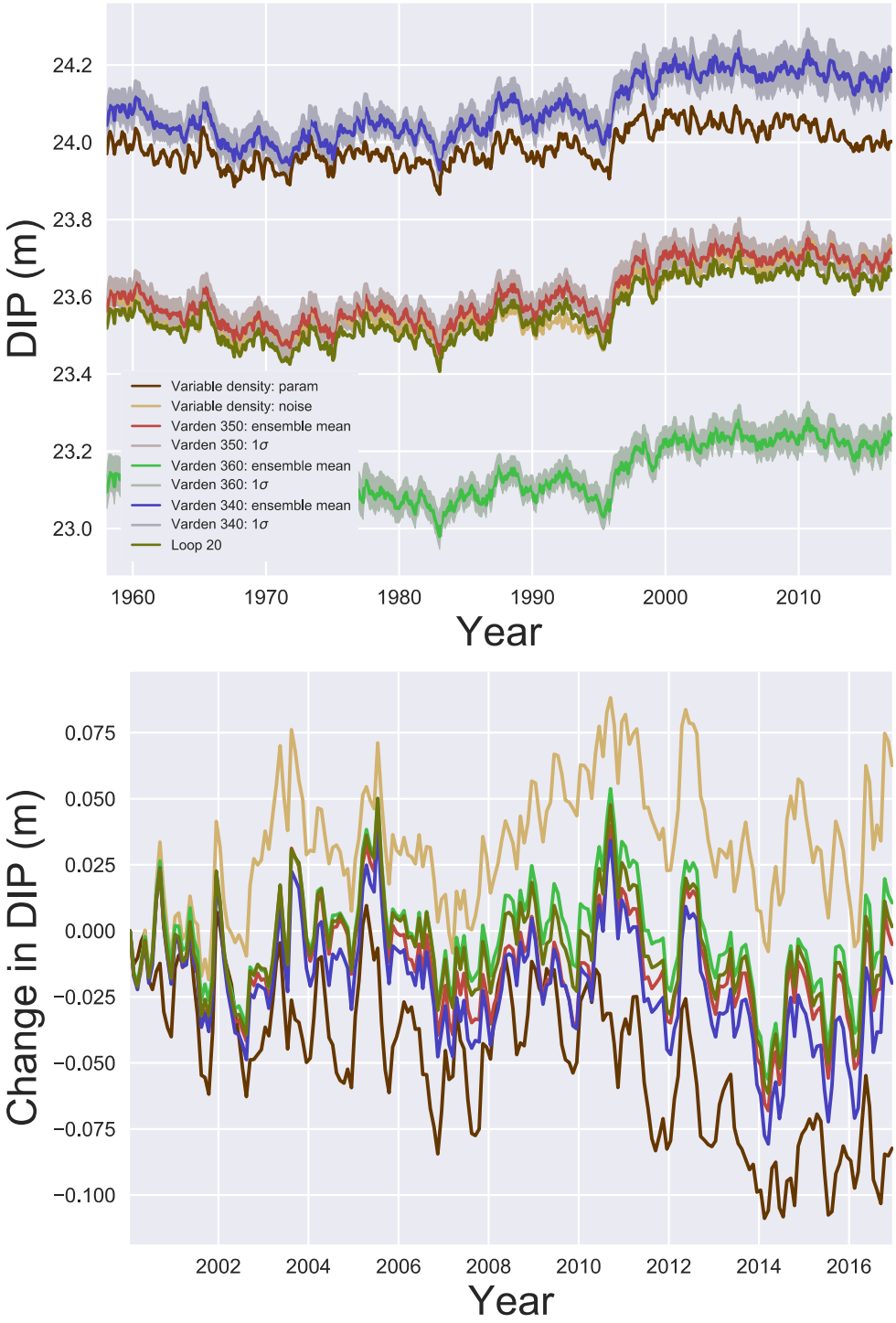

Figure 3.8. DIP (top) and change in DIP (bottom) since 2000 predicted by KM using different surface densities.

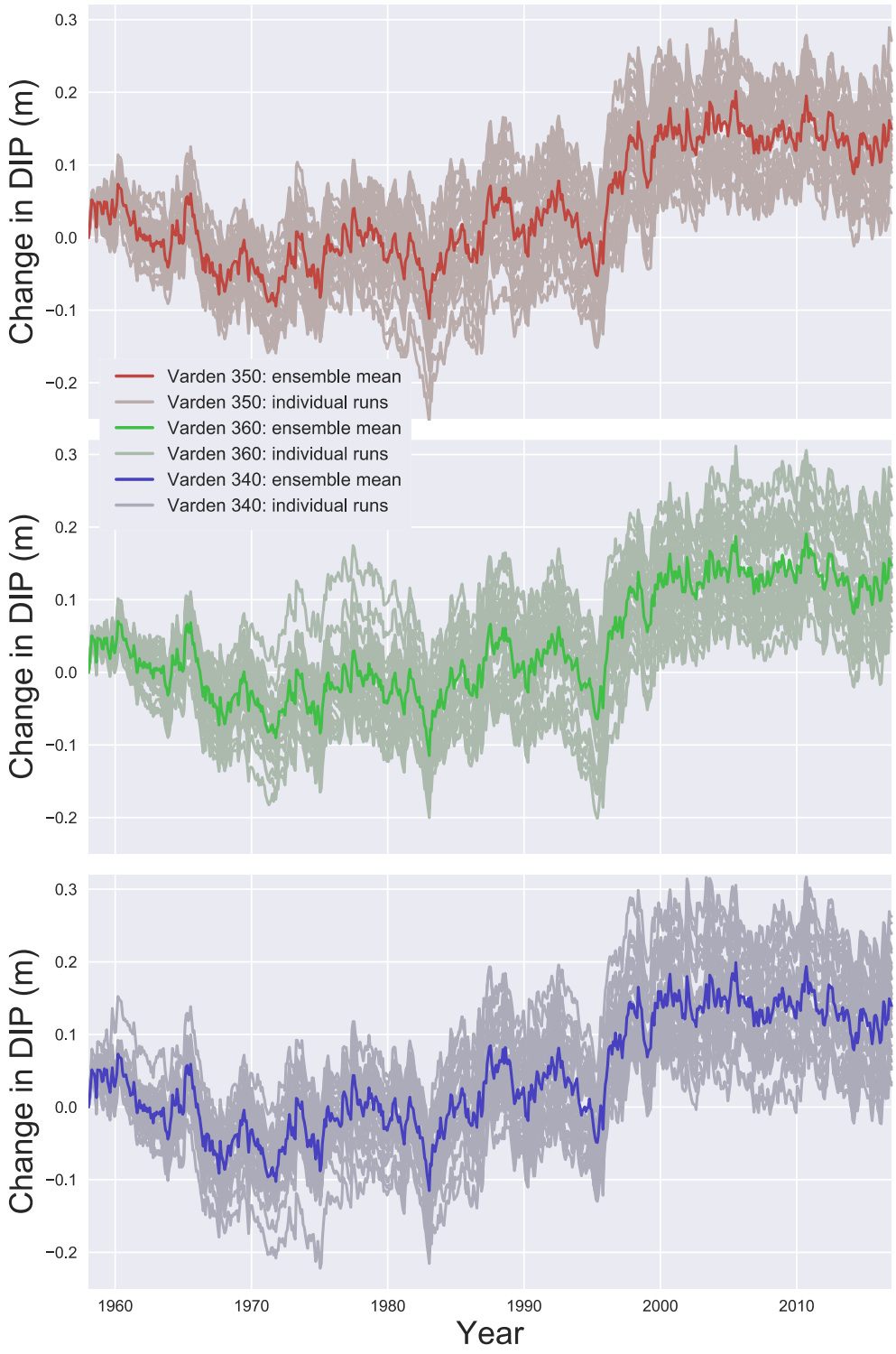

Figure 3.9. Change in DIP since 1958 predicted by KP using an ensemble of surface density forcings.

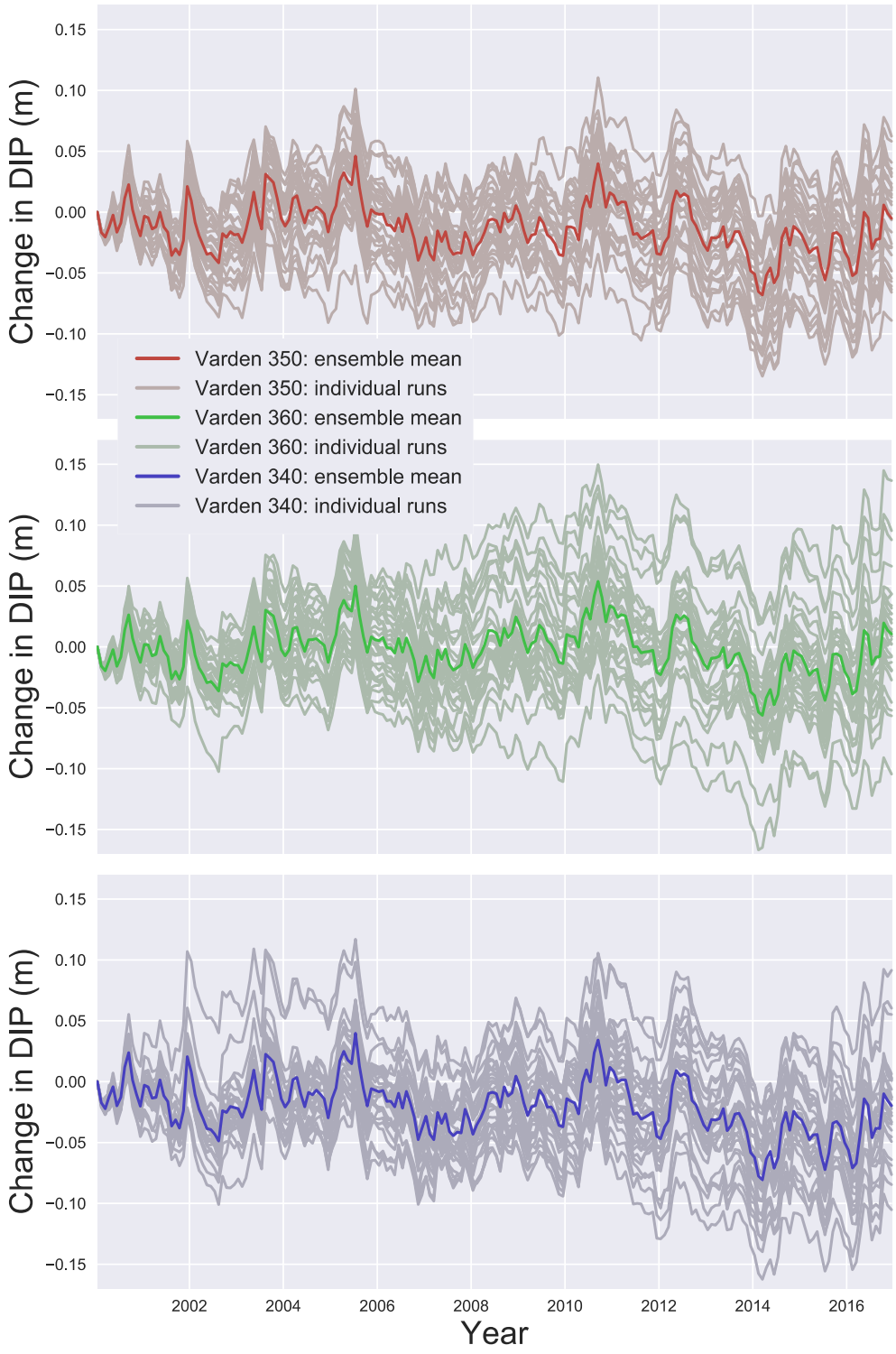

Figure 3.10. Change in DIP since 2000 predicted by KP using an ensemble of surface density forcings.

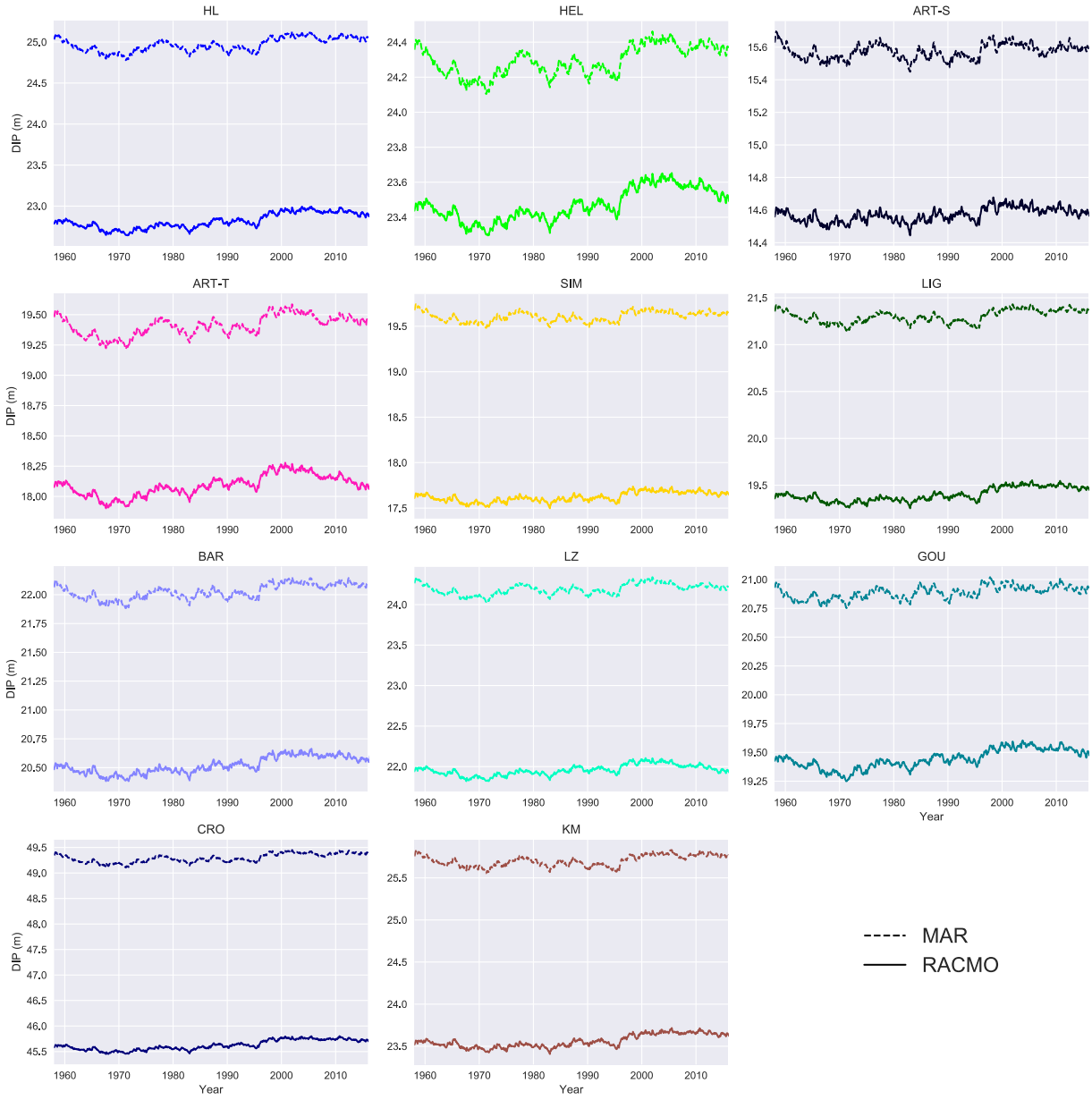

Figure 3.11. DIP predicted by the models when forced with MAR vs. RACMO fields.

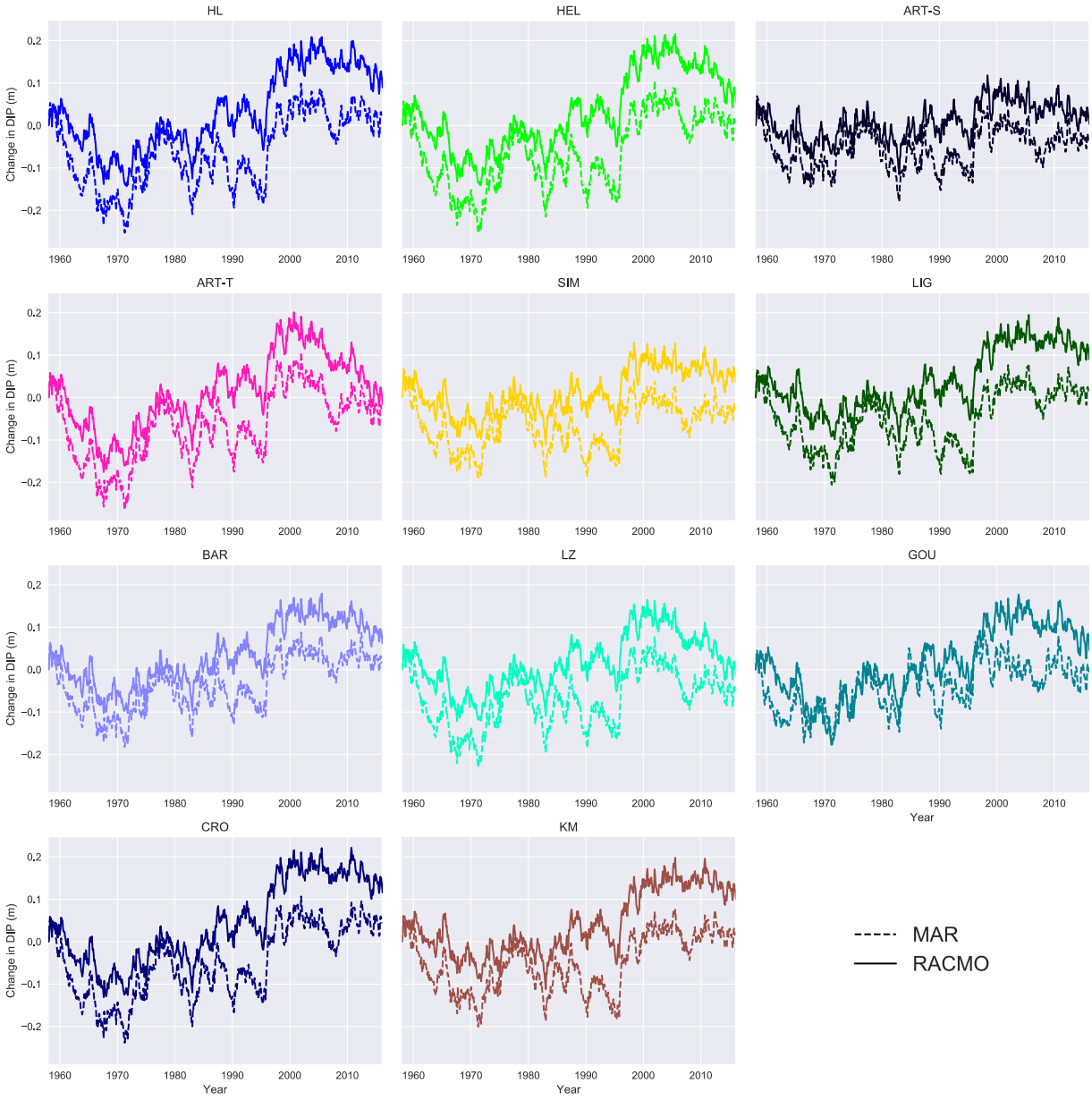

Figure 3.12. Change in DIP since 1958 predicted by the models when forced with MAR vs. RACMO fields.

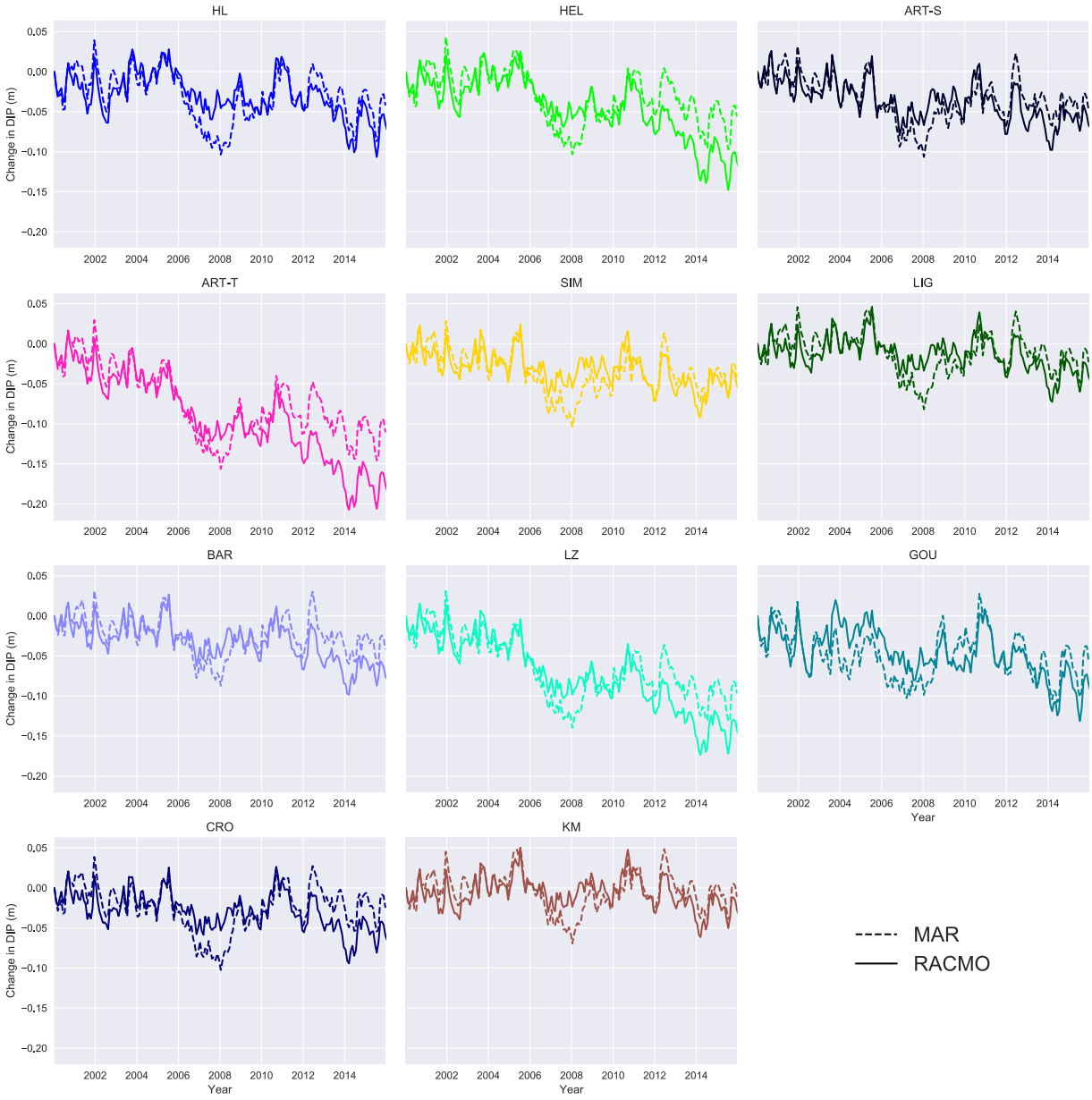

Figure 3.13. Change in DIP since 2000 predicted by the models when forced with MAR vs. RACMO fields.

Table 3.5. Comparison of model results using RACMO vs. MAR climate forcings.

	mean DIP RACMO	mean DIP MAR	dDIP 1958 RACMO	dDIP 1958 MAR	dDIP 2000 RACMO	dDIP 2000 MAR
HLdynamic	22.820	24.968	0.116	0.018	-0.065	-0.042
Helsen2008	23.472	24.293	0.078	0.006	-0.113	-0.056
Arthern2010S	14.571	15.574	0.018	-0.039	-0.067	-0.047
Arthern2010T	18.092	19.412	0.009	-0.034	-0.176	-0.111
Simonsen2013	17.624	19.608	0.051	-0.032	-0.052	-0.042
Ligtenberg2011	19.402	21.303	0.108	0.008	-0.041	-0.023
Barnola1991	20.522	22.028	0.078	0.015	-0.075	-0.042
Li2011	21.958	24.193	0.006	-0.051	-0.143	-0.097
Goujon2003	19.444	20.888	0.073	-0.006	-0.085	-0.056
Crocus	45.627	49.293	0.136	0.043	-0.060	-0.025
KM	23.563	25.704	0.120	0.015	-0.028	-0.011

Chapter 4. A COMPARISON OF MODELLED AND MEASURED FIRN PHYSICAL PROPERTIES AND COMPACTION RATES IN GREENLAND

4.1 ABSTRACT

We have measured firn compaction rates, temperatures and density at eight sites in Greenland spanning the dry and wet firn zones. We compare those observations to predictions from a suite of firn-densification models. We find that the models can predict generally predict the mass in the top 16 m of firn to within 5 to 10%, and the compaction rates to within ~15%. We use our measurements to propose a firn-densification model for Summit, Greenland and find that our results agree well with previously published estimates of the temperature sensitivity of firn. Our results have implications for estimates of ice-sheet mass change from satellite altimetry, which rely on predictions of firn air content from firn models.

4.2 INTRODUCTION

The mass balances of the polar ice sheets are of societal interest because of their control on sea level; the uncertainty in ice-sheet mass change is among the largest uncertainties in projections of future sea-level rise (Vaughan and others, 2013). Paramount to estimating ice-sheet mass changes is understanding how the firn, the porous upper layer of the ice sheets, responds to transient climate.

Firn begins as snow that accumulates on an ice sheet or glacier. Below the equilibrium-line altitude (ELA), all of the annual snowfall melts or sublimates, above the ELA, some snow remains through the year. The historical definition of firn is snow that lasts through a melt season. As more snow accumulates, overburden stress and metamorphic processes cause the snow and firn to

densify, and eventually the firn becomes glacial ice. Within the accumulation zone are several sub-zones (Benson, 1961; Cuffey and Paterson, 2010, p. 14). In the dry-firn zone, there is negligible melt and rain. Firn densifies by sintering mechanisms, and heat is transported via diffusion. At lower elevations and/or latitudes there may be a percolation zone where there is some surface melt and/or rain in the summer. Because firn is porous and permeable, this water percolates downward into the firn and can refreeze or run off. The firn in this zone can become denser rapidly by sintering processes or through the refreezing of meltwater in the pore space (Harper and others, 2012). Heat is transported through diffusion as well as through latent heat released by refreezing meltwater. At elevations and/or latitudes lower than the percolation zone is the wet-snow zone, in which all snow has reached the melting temperature and the snow may become saturated.

Interest in firn for understanding mass balance is two-fold. First is the densification problem. Satellite and airborne altimetry methods are capable of measuring ice-sheet surface elevation to centimeter-scale accuracy (Krabill and others, 2002). In order to calculate the mass and mass change associated with the (volumetric) altimetry measurements, the density must be known. Surface-elevation changes can be caused by ice-sheet thickness changes, which are mass changes, or by firn-density changes, which do not necessarily change the mass of the ice sheet.

Second interest is that the firn layer has capacity to store and refreeze meltwater. The area where annual melt occurs in Greenland has increased (Mernild and others, 2011), and in July 2012 there was melt over the entire Greenland ice sheet (Nghiem and others, 2012). As melt increases in Greenland, the area that experiences melt increases quadratically because of the hypsometry of the ice sheet (Van As and others, 2017). The fate of surface meltwater is poorly known but is of great importance to both understanding the current mass balance of the ice sheets and predicting future changes. Harper and others (2012) used measurements from southwest Greenland to suggest

that percolating meltwater would fill the firn's pore space before running off, effectively delaying the sea-level rise associated with the loss of that mass reservoir. However, Machguth and others (2016) observed several-meter thick, perched (i.e. atop porous, permeable firn) ice layers in the upper meters of the firn in the percolation zone of southwest Greenland. They hypothesized that these ice layers prevent meltwater from reaching the pore space of deeper firn, and thus runoff of surface melt becomes greater than refreezing within the firn before all of the pore space is filled. An additional water storage reservoir was recently discovered in southeast Greenland in the form of perennial firn aquifers (Forster and others, 2014), which can form where high accumulation rates allow liquid water to be insulated from the cold winter (Kuipers Munneke and others, 2014).

Firn-densification models are commonly used to estimate the total mass of the firn and to provide a correction to the altimetry products to account for elevation changes due to transient firn thickness and density changes (Zwally and Li, 2002). Some firn-evolution models also have routines to simulate percolation and refreezing of meltwater. However, many of the equations describing the physics of firn densification have been derived assuming dry-firn densification and/or calibrated using measured depth-density profiles, which inherently invokes a steady-state assumption. It is not clear that it is appropriate to apply a steady-state assumption to a time-varying scenario nor that the physics of dry-firn densification can be extended to wet firn zones. Other models have been developed for seasonal snow and extended to firn, but it is also not clear if this is a valid extension; in a recent model intercomparison, a seasonal snow model was not able to predict densification of firn under polar climate conditions (Lundin and others, 2017).

Most meltwater-percolation models use simplified physics to describe the transport of meltwater in 1-D model schemes by assuming that water percolates homogeneously through the firn's pore matrix. In reality, research has shown that water often travels through preferential flow

paths (Marsh and Woo, 1984), which can transport mass and heat to greater depths than matrix flow.

We have measured firn properties, including density, stratigraphy, temperature, and compaction rates at eight sites in Greenland. In this paper, we compare these measurements to predictions from numerous firn-densification models. We also use our measurements to derive a new dry-firn-densification equation for Summit, Greenland.

4.3 METHODS

4.3.1 The Firn Compaction Verification and Reconnaissance (FirnCover) project

FirnCover is a network of eight stations in Greenland measuring firn physical properties and compaction rates. The sites are shown in Figure 4.1, and their climatologic properties are listed in Table 4.1. All sites are in the accumulation zone of the ice sheet. They range from high-elevation, cold sites (e.g. Summit) to high-melt sites near the ELA (e.g. KAN-U). The accumulation and melt values in Table 4.1 are values predicted by the regional climate model (RCM) RACMO2.3p2 (Noël and others, 2018) at the grid point closest to the site. Table 4.1 lists four values in the annual temperature column: the first is the skin temperature predicted by RACMO2.3p2, the second is the air temperature (1-2 m) measured by FirnCover instruments, the third is the firn temperature at 10-m depth measured by FirnCover instruments, and the fourth is the 10-m depth temperature predicted by the Community Firn Model (Chapter 4.4.2).

Each FirnCover site has a suite of instruments including numerous firn-compaction instruments (described below), a thermometer measuring air temperature at ~1-2 m, a sonic ranger measuring snow surface height, and a thermistor string installed to ~10-15 m depth. The depth of the thermistor strings varies by site because of challenges encountered while drilling. The data are recorded daily on a data logger and transmitted via satellite modem.

The FirnCover compaction instruments are automated ‘coffee-can’ type (Hulbe and Whillans, 1994b; Hamilton and others, 1998) devices similar to those used by Arthern and others (2010). A cartoon of the instruments is shown in Figure 4.2. A firn-compaction instrument is installed to a particular depth by first drilling a borehole. Then, a string is attached to an anchor frozen into the bottom of the borehole. On the surface above the borehole is a platform (approximately 60 cm x 60 cm) with a string potentiometer attached to it. As the firn compacts, the platform moves towards the anchor, and the potentiometer measures how much string is reeled in. The instruments thus always measure compaction in the same portion of the firn; as the firn advects downward, the instrumentation advects with it and the platform is buried.

Three sites (KAN-U, DYE-2, and EKT; marked in red in Figure 4.1) were instrumented during the 2013 Arctic Circle Traverse. The additional five stations were deployed during the 2015 FirnCover field campaign, and also in 2015 the three original stations were updated with more instruments. By the end of the 2015 field season each site had eight compaction instruments deployed. All eight sites were visited during field campaigns in 2016 and 2017, and additional compaction instruments were deployed. As of writing, there are 50 compaction instruments installed. At the warmer, wetter sites (KAN-U, DYE-2, EKT, Crawford Point) we dug to the previous melt-season surface and installed the platform at that level, except for a single instrument at each of these sites measuring compaction from the surface to ~2 m depth. At the other sites, all the instruments were installed on the surface. The depths of the boreholes varied by site; in general, each site initially had a shallow hole to measure near-surface compaction; a hole to ~8 m, and a hole to ~16 m depth. Several sites (Saddle, NASA-SE, Summit, EastGRIP) had 2 instruments to ~16m depth to test the robustness of the measurements. Instruments installed in 2016 were to

depths from 16 to 18 m, depending on site, and in 2017 instruments were drilled to ~22 m at each site.

We recovered firn cores from each of the boreholes we drilled, and we measured density and stratigraphy on these cores. Stratigraphy was qualitatively recorded as "ice", "percolated firn" (i.e. firn that meltwater had percolated through), or "dry firn". We calculated density as mass divided by volume. During the 2015 and 2016 field campaigns, we cut the cores into 10 cm sections and weighed each section. In 2017 we altered our method slightly and measured each section's length and diameter, and we cut the sections at stratigraphic boundaries rather than at 10 cm increments; on average the sections were still ~10 cm.

4.3.2 Modeling

We ran the Community Firn Model (CFM) for each FirnCover site using output from RACMO2.3p2. RACMO output is available on an 11-km grid and we used the output from the grid point closest to the FirnCover sites. The CFM was forced using daily time steps.

The simulations at the wet-firn sites required the addition of two new modules in the CFM to model meltwater percolation and refreezing. The meltwater transport is handled using a 'bucket scheme' (e.g. Langen and others, 2017; Steger and others, 2017). At each time step when there is surface melt the model first removes the meltwater mass from the upper layer(s) of the model. The water can then freely percolate through the firn. Water is assumed to flow downward homogeneously through the pore space of the firn due to gravity. When liquid water reaches a layer, some volume of water is refrozen unless the layer is already at the melting point. The volume that is frozen is determined by the cold content of the layer: the energy to bring the layer to the melting temperature is provided by refreezing of water. Each layer also retains a small amount of water (the irreducible water saturation), which is the liquid water retained due to capillary forces.

Liquid water that is not refrozen or retained due to capillary forces moves to the layer below. The percolation stops when there is no longer any liquid water to percolate downward.

If the liquid water reaches a layer with a density high enough to be impermeable (in this study we use 800 kg m^{-3} (Gregory and others, 2014)), the water pools and fills the open porosity of that layer. If there is inadequate pore space to accommodate the water, the water fills the all of the available space and then fills the porosity in the layer above, and so on until the entire volume of liquid is accommodated. If the liquid water cannot be accommodated in the pore space, it is considered to be run-off and is removed from the model domain.

The assumption of homogeneous (matrix) flow through the firn is often used for meltwater in firn (e.g. Kuipers Munneke and others, 2015; Langen and others, 2017), though homogenous flow is not what always happens in reality. Numerous studies have shown that water is often transported by preferential flow paths, also known as pipes or conduits (Marsh and Woo, 1984; Pfeffer and Humphrey, 1996), in both seasonal snow and firn. This heterogenous flow is capable of delivering mass and heat to greater depths and on different timescales than homogeneous flow. It is not clear in what regimes an assumption of heterogeneous flow is and is not appropriate. In reality, the liquid transport is likely both by matrix flow and preferential flow.

Incorporating preferential flow into a one-dimensional model presents a challenge because it is a three-dimensional process. The spatial distribution of conduits and the depths they reach in nature is not well constrained, especially on ice sheets where data are sparse, and these details have a significant effect on the redistribution of mass and heat. Recent work has made progress on parameterizing the preferential flow in a one-dimensional model using a dual-domain approach (Wever and others, 2016), but more data are needed to test its applicability to firn on ice sheets. So, for now we do not model preferential flow.

The bucket scheme is commonly used for water transport in firn models (Kuipers Munneke and others, 2014; Wever and others, 2014), but it suffers in that it assumes that all mass transport is immediate. An alternative is to model flow using Darcy's equation, which relates the flux of water to the hydraulic head and the permeability for saturated conditions, or using Richard's equation, which describes flow in unsaturated conditions. In both schemes, percolation is delayed due to the permeability. Langen and others (2017) compared the results of a model using Darcy flow and a model using a bucket scheme. Their results suggested that the Darcy flow gave different results on short time scales but did not yield different results for the temperature or mass balance on seasonal and longer time scales. Wever and others (2014) showed that using Richard's equation for modeling runoff from a seasonal snowpack produced more accurate results than using a bucket scheme. A challenge of using these schemes is that the permeability must be known. Permeability is not well constrained for firn, and it is not necessarily correlated with density (Adolph and Albert, 2014; Sommers and others, 2017).

The second new feature in the CFM for meltwater percolation is an enthalpy diffusion module, based on Aschwanden and others (2012). Because the firn can include both liquid water and ice, a temperature diffusion solution cannot account for the energy transfer associated with the latent heat of refreezing. Using an enthalpy formulation allows us to model the energy transport in the firn, which can either change the temperature or the phase. The current formulation uses a high thermal conductivity to simulate phase changes, but ongoing work will use a source-term formulation to handle the energy transfer associated with phase change (Voller and others, 1987).

4.4 RESULTS AND DISCUSSION

4.4.1 Firn density and stratigraphy

Figure 4.3 shows the depth-density (black lines) and stratigraphy profiles (blue lines indicate observed ice lenses) measured at each FirnCover site during the 2015 field season. It also shows the profiles predicted by the CFM in red. The CFM model results shown here were produced using the firn-densification equations described by Kuipers Munneke and others (2015) using daily time steps. The surface density was held at 350 kg m^{-3} except at Summit, where it was 300 kg m^{-3}. Modeled ice lenses are the spikes in the modeled density. Figure 4.3 also shows the mass of firn derived from the measurements and the corresponding values predicted by the model. Results from KAN-U are excluded because the model runs for that site failed to complete; this is due to too much melt in the forcing data, which effectively turns the modeled site into an ablation site.

Figure 4.3 also lists the depth-integrated mass of the measured and modeled firn to the depth of the cores. The model predicts more mass than we measured in the firn column at five of the seven sites. At the two dry sites (EastGRIP and Summit), the model qualitatively predicts the slope of densification well. It predicts 5% too little mass at Summit and 10% more mass than measured at EastGRIP. The excess mass at EastGRIP is due to numerous spikes in the modeled density, which are likely due to too much melt in RACMO2.3p2 at that site. The bulk of the modeled density is higher than observed, meaning the model is predicting a densification rate that is too fast. At Summit, the densification rate is too slow. The 2012 melt event is visible as a density peak in both modeled cores near 2 m depth, but it is much too thick and has a modeled density of ~600 and 500 kg m^{-3} at EastGrip and Summit, respectively. Field observations at both sites in 2015 showed a horizontally discontinuous ice lens 1-2 cm thick.

At the moderate-melt sites (EKT, NASA-SE, and Saddle), the model shows mixed performance. At NASA-SE, the modeled mass matched the measurements nearly identically. At Saddle and EKT, the modeled mass is 12% and 19% too high, respectively. At each of these sites the low side of the density profile matches the data reasonably well, but the refrozen water creates many density spikes in the model. The model does not capture the stratigraphy well at any of these sites. It does not capture any of the very thin layers that were observed, and it predicts ice layers and high-density layers that are much too thick. The layers in the CFM are thin enough that the model could create thin ice lenses, so this model-data mismatch is likely due to the bucket scheme not transporting and storing water realistically. At NASA-SE we observed a series of thin ice layers at ~6 m depth; the model captures this zone of higher mass as a broad peak in density but at a slightly greater depth. At EKT, the model predicts thick ice lenses at ~3-4 m, which is slightly shallower than the depths at which we observed series of thinner ice layers.

At the sites with the most melt, Crawford Point and DYE-2, the model results do not match observations well. This could be due to the model incorrectly simulating physical processes or due to the boundary conditions (e.g. the surface temperature and amount of melt) not representing reality. The modeled masses at Crawford Point and DYE-2 are much higher than observed (34% and 27%). The model predicts thick ice lenses at each of these sites. We did observe ice lenses at each of these sites, but not as thick or as continuous as the model predicts. Where the model is not predicting ice lenses the densities are also much higher than observed, indicating that the model predicts that water has refrozen in all layers of the firn. Even at these wet sites, we interpreted the grain structures of some layers as dry (i.e. never-been-wetted) firn.

The discrepancies between the measured and modeled firn density and stratigraphy profiles may be due to one or a combination of factors. The first is that the bucket scheme used in the CFM

is doing a poor job of transporting and storing water at the correct depth. This is supported by the thickness and density of the 2012 layer at Summit and EastGRIP predicted by the model as well as by the number of thin ice lenses we observed at the moderate- and high-melt sites. The thick ice lenses modeled at the high-melt sites suggest that instead of freezing meltwater in thin layers, the model allows water to pool and grow thick lenses. This could be related to the choice of density (taken to be 800 kg m^{-3}) at which the firn is considered impermeable in the model; however the higher-density layers at Summit and EastGRIP suggest that the problem could be related to the fact that the bucket scheme percolates water immediately; potentially a Darcy-flow scheme would delay the percolation enough to allow the mass of water to freeze in place rather than percolating and spreading through several layers.

The model also does not have an explicit scheme to allow runoff; runoff occurs only when meltwater cannot be accommodated within the pore space. The model could be predicting too much mass in the firn because the mass is retained, whereas in nature some mass of meltwater may have run off. The question of how much meltwater from the accumulation and wet-firn zones is of critical importance in order to understand the liquid water balance of the Greenland ice sheet; unfortunately, we do not have data to advance our understanding of this question, though the higher-than-observed firn masses at Crawford Point and DYE-2 do suggest that some portion of the melt is running off.

Model-data mismatch is also due to fact that the climate forcing from the RCM have uncertainty. It is beyond the scope of this paper to assess the accuracy of the RCM outputs, but the higher modeled masses suggest that the RCM could predict accumulation that is too high, and the thick ice lenses predicted by the CFM (e.g. at DYE-2) could indicate that the RCM predicts too much melt. One improvement of RACMO2.3p2 was to improve the melt field; RACMO2.3's

predicted melt was too high for much of Greenland (Noël and others, 2018). It does appear that RACMO2.3p2 still predicts too much melt at Summit and EastGRIP. The RCM predicts three melt events at Summit in recent time, when only one has been observed, and 23 days at EastGRIP that have had more than 1 mm of melt. Another uncertainty comes from the fact that the RACMO2.3p2 data are on an 11-km grid, and the CFM was forced with the RACMO data from the grid point nearest to the site. It is possible that the actual climate at the FirnCover site could differ from that at the RACMO grid point. For example, Saddle sits on a divide; the accumulation to the east is generally greater, and to the west generally less.

There is also error associated with the firn-densification models. The model outputs shown in Figure 4.3 were produced using the Kuipers Munneke and others (2015) model. We also ran the CFM forced with other firn-densification physics. No single model performed the best at all locations. For example, at EastGRIP the Herron and Langway (1980) model predicts firn mass closest to our observations, whereas at Summit the Ligtenberg and others (2011) model predicts the mass closest to observations. Interestingly, at DYE-2, the Barnola and others (1991) model, which was developed for interpreting ice-core records, most closely matches our observations.
All of these models (with the exception of CROCUS, which was developed for seasonal snow) were formulated for dry firn. All the firn-densification models have a number of tunable parameters, which represent microphysical processes in a macroscale approach (e.g. see Morris and Wingham, 2014). The fact that the models do not perform well at the wet sites may indicate that the tuned macroscale parameterizations are not applicable at wet sites. We qualitatively observed that the grain size and shape of wetted firn differed from that of dry firn. These differences could cause different microphysical processes to dominate and render dry-firn-densification physics inapplicable.

The surface-density boundary condition presents a modeling challenge. A number of parameterizations for firn surface density (e.g. Kuipers Munneke and others, 2015) have been proposed, but none of these has been shown to be universally applicable. Our value of 350 kg m^{-3} for the surface density works well at EastGRIP, but at Summit it is too high. The CFM does not consider snow at the surface to be different than firn.

Finally, there are uncertainties associated with our measured core densities. In 2015 and 2016 we did not measure the diameter of individual sections of core. In 2017 we employed an improved method and measured each core section's length and diameter. In 2017 we also changed our method to cut core sections at stratigraphic boundaries (previous campaigns cut cores into 10-cm sections regardless of stratigraphy), which improves density-measurement resolution around the stratigraphic boundaries. A 2-mm error in our core diameter adds ~5% error to the density near the surface. A 2-mm error in core section length adds ~2% error to the density measurement. The 2015 and 2016 core-density data is more likely to be biased low than high due to the assumed radii potentially being slightly too high. We estimate the stratigraphy profiles are accurate to 1 cm.

4.4.2 Firn temperature

We subtracted the firn temperatures measured by our RTD strings from the temperatures predicted by the CFM, and the results from DYE-2, NASA-SE, and Summit are shown in Figure 4.4. Blue colors show where the modelled temperatures are colder than the measurements, and reds show where the modelled temperatures are higher than the measurements.

At DYE-2, the model predicts the temperature being slightly too warm in the deeper firn. Throughout much of the year, the model is predicting too cool of temperatures near the surface (upper ~3 m). This behavior suggests that the model is transporting too much heat to the deeper firn. The physics of heat diffusion are well constrained, so we attribute this data-model mismatch

to meltwater being delivered to too great of a depth, which may be related to the bucket scheme in the model. Near the surface, the periods when the model predicts too-warm temperatures (notably summer 2016) are due to the model storing liquid water near the surface, thus keeping the firn at the freezing temperature. The RTDs recorded below-freezing temperatures at these times, suggesting that the RCM output is not predicting the timing of melt correctly. The times that the model is much too cold (darkest blues, e.g. June 2016; August 2016) are due to melt events that occurred and were recorded by the RTD string. The RCM either did not predict these melt periods and/or did not predict enough melt. Alternatively, the model could have prevented meltwater from percolating downward due to an ice layer at ~1m depth in the model (Figure 4.3).

The fact that the firn at depth is colder than the model predicts suggests that the model is not transporting liquid water (which releases latent heat upon refreezing in the firn) properly or that the RCM is predicting too much melt, which would result in the model firn receiving too much latent heat. The latter point corroborates the evidence from the depth-density profiles. Alternatively, preferential flow conduits could be delivering mass and heat to different depths than the homogeneous-flow scheme in the model allows. If these conduits were spaced adequately far apart, this preferential flow could concentrate heat and mass in select areas, which our firn cores and RTD string may not have sampled. We do not have adequate data to do more than speculate, but a 3-m-deep snow pit at DYE-2 revealed numerous thick (>10 cm) ice lenses that were horizontally discontinuous. This observation indicates that lateral meltwater flow is an important process, and it must be incorporated into model simulations.

It is also possible that the RCM outputs predict mean annual temperatures that are too warm at these sites, but the 2016 mean annual temperature measured by the FirnCover station (-17.6°C)

is similar to the long-term RACMO mean annual temperature (-18.1°C) at DYE-2, whereas the measured 10-m temperature is -12.8°C and the modeled 10-m temperature is -12.0°C.

At Crawford Point, the model predicts temperatures that are too cold in the summer and too warm in the summer (>3°C differences from the measurements). The warm modeled summer temperatures are a result of predicting multiple melt events percolating to ~1 m depth in summer 2015 and 2016; the RTDs did not detect either of these events. Again, this could be due to melt being channeled through conduits that were distant from the RTD string. The cold winter temperatures predicted by the model suggest that the amplitude of the seasonal temperature cycle predicted by RACMO could be too large at this location, which could include the prediction of too much melt in the summer. The fact that there is a several-degree difference between the mean annual temperature and the measured 10-m temperature at Crawford Point and at DYE-2 indicates that some amount of latent heat is indeed released in the firn.

At NASA-SE, the modeled firn temperature is close to the RTD data; at depth it is always within 0.75 degrees. The model is too cold near the surface for much of the year; the high accumulation rate at NASA-SE makes it impossible to compare temperatures in the top 2 m during summer 2016. The model's alternating slightly warmer and colder than measured temperatures at depth could indicate that the model is not conducting heat at the correct rate, or the advection of firn downward could be incorrect due to errors in the accumulation forcing.

At Summit and EastGRIP (not shown), the model predicts 10-m temperatures that are too warm compared to the measurements. Because there is no melt at Summit during this period, we can be confident that the discrepancy is due to the RCM output. The modelled and measured 10-m temperatures are within 1°C of each other. Near the surface, in the late summer and early fall

the modeled temperature is colder than the measurements, suggesting that the RCM output is too cold in that period.

There is error in the firn temperature profiles measured with the RTD string because as snow falls the depth of the RTDs increases. To calculate the depths of the RTDs, we added the change in surface elevation measured by the sonic ranger to the initial depths of the RTDs. The sonic ranger data is of varying quality, having periods during which there were no measurements or large spikes (e.g. a spike of 50 cm lasting for several days) in the data that we interpret to be due to instrument error or non-accumulation processes such as rime buildup on the instrument. We also see transient spikes in the data that could be related to blowing snow or rime buildup. We processed the sonic ranger data by removing the spikes and linearly interpolating over the missing data. These uncertainties in our RTD depths are not large enough to change our conclusions about the firn temperature data.

Disturbing the firn to install the RTD string may also add uncertainty to the measurements, especially at the wet sites. After installing the RTD string at each site, we filled in the hole with snow. At Summit, we expect this fill to quickly equilibrate to the ambient temperature and conduct heat similarly to the in situ firn. At the wet sites, it is possible that the permeability of the fill could differ from that of the surrounding firn and locally change the water flow. However, we are confident that the RTD string itself did not act as a conduit because the temperature records do not show the firn to be near the freezing point at depth at any of the sites (firn was always colder); i.e. the RTD strings show that water did not percolate to depths greater than ~1.5 m (except at KAN-U).

The temperature profiles predicted by the different models vary from one another because the conductivity of firn in the model is dependent on the density, which varies by model, but these differences are small and do not change our conclusions.

4.4.3 Firn compaction

Figure 4.5, Figure 4.6, and Figure 4.7 show the compaction rates measured at Summit, EastGRIP and NASA-SE (dashed black lines), respectively, and the compaction rates predicted by the CFM using various firn-densification physics (colored lines). Our instruments measure the shortening of an interval of firn; the interval of firn is the length of the borehole. The compaction rate is the rate of change of the length of the borehole. We focus here on the instruments that were installed in 2015. These three sites each had two instruments installed to ~16 m, an instrument installed to ~8 m, and an instrument to 4 m (Summit and EastGRIP) or 2 m (NASA-SE). We also calculate compaction in intervals of firn spanning the bottom of a shallow hole and the bottom of a deeper hole by differencing the compaction rates of two holes (e.g. subtracting the compaction rate observed in an 8-m hole from that observed in a 16-m hole gives the compaction between 8 and 16 m). We refer to these intervals as 'virtual holes'. At these three sites the pairs of 16-m instruments show very similar results, indicating that the instruments are working as designed. All the data show very high compaction rates at the beginning of the record (first two months), which we assume is due to instrument settling, and we exclude that data from our analyses. The data are smoothed using an 11-point Hanning window. The results from the other sites are not shown here given the focus of the paper but are available upon request.

The compaction-rate data show a clear seasonal cycle. The peak compaction rate is at the end of the summer, when warm temperatures have had adequate time to diffuse downward. At Summit, the minimum compaction rates are observed in March. In the near-surface firn (<4 m) the

highest compaction rates are about four times the minimum rates. The seasonal cycle can still be seen in the virtual hole extending from 4-8 m, but the timing of the minimum and maximum is delayed due to the timescale of heat diffusion. The seasonal cycle cannot be observed around the 8 – 16 m virtual hole.

At NASA-SE, the maximum compaction rate in the shallowest hole (2 m) is approximately twice its minimum. These maxima and minima, in October and April, respectively, occur slightly later in the year than at Summit. In the deepest virtual hole at NASA-SE (8-16 m), the compaction rate decreases through time as the firn densifies.

At EastGRIP, the minimum compaction rates are in March, (around the same time as at Summit), and the maximum compaction rate occurs in August (slightly earlier than at Summit). The maximum is about three times greater than the minimum. Two large spikes are evident at EastGRIP in late summer 2016 in all sensors; we hypothesize that these are caused by activities associated with the EastGRIP ice-core drilling project driving near the station.

The models show mixed and inconsistent performance at the three sites, and their performance varies over the depth intervals. We find the RMS error for the models over the time series of the data and divide the RMS error by the mean compaction rate for the year 2016 to find the percent error. These errors are listed in Table 4.2, Table 4.3, and Table 4.4.

At Summit, in the shallowest interval (0-4 m), most models predict the timing and magnitude of the winter minimum compaction rates well. Most predict the timing of the maximum but fewer of them predict the summer magnitude well. The Simonsen and others (2013) and a new model we propose in Chapter 4.5 show the best performance for the shallow interval, with an RMS error of 0.016 m a^{-1}, or ~13% of the 2016 mean annual compaction rate. In the mid-depth interval (0-8 m), the model performance is similar: the model proposed by Simonsen and others (2013) has

an RMS error of 0.017 m a^{-1}, or 8.5% of the signal. In the deeper holes, our proposed model performs the best by a slight margin (RMS error of 5.7% and 8.3% in the two 16-m holes). In the virtual holes, the Simonsen and others (2015) model performs best. It is notable that most of the models in the deepest virtual hole, from 8-16 m, are off by more than 20%.

At EastGRIP (Figure 4.6), the models do not reproduce observations as well as at Summit. The Arthern and others (2010) transient model reproduces the observations best. For Instruments 26 and 29, which were installed from the surface to ~16m depth, all of the models have over 20% RMS error. The high percent error is due to the fact that the compaction rates at EastGRIP are low. Most of the firn-densification models are predicting compaction rates that are too low in the winter; this is surprising, considering that the CFM's temperature model predicts temperatures that are warmer than observed (Chapter 4.4.2). The models do predict the amplitude of the seasonal cycle well, especially near the surface.

At NASA-SE, the Ligtenberg and others (2011) model reproduces the observations best overall, which is perhaps surprising because it was calibrated with Antarctic conditions (i.e. its output is distributed with RACMO output for Antarctica, whereas the Kuipers Munneke and others (2015) model output is distributed with the Greenland RACMO product). In the shallowest hole (2 m), all of the models have more than 20% error, with most greater than 50%. The Arthern and others (2010) (steady) model predicts the observations best in this interval, but does not reproduce the observations well in the interval extending from 2 to 16 m (Instrument 109); in this interval nearly all of the models predict compaction rates that are too high. In the 8-m and 16-m intervals, the Ligtenberg and others (2011) and CROCUS (Vionnet and others, 2012) models predict the compaction well (6 to 8% error), and the Kuipers Munneke and others (2015) model has 9% and 11% error in those intervals.

At all the sites, the Herron and Langway (1980) model fails to predict the seasonal cycle, suggesting that its temperature sensitivity is poorly calibrated.

The compaction rates measured at Crawford Point also show a clear seasonal cycle as well, though of much smaller amplitude than at the other sites. The models do not predict compaction well there, which could be due to improper handling of meltwater in the CFM, or due to errors in the RCM output (e.g. too much melt). The firn-compaction instruments at DYE-2 and KAN-U show results that are challenging to interpret. For much of the year the instruments show no compaction, and they have periods when there are spikes of high compaction rates. This could indicate that the refrozen meltwater stiffens the firn through much of the year and that there are occasional times when the firn compacts quickly, ostensibly due to warming associated with meltwater percolation. However, it is also possible that the string froze to the borehole wall or had ice freeze around it, temporarily preventing the string from being reeled in, or that the instrument itself has stopped working properly due to the amount of meltwater in the vicinity.

4.5 A NEW CONSTITUTIVE RELATIONSHIP FOR DRY FIRN

Numerous models describing the evolution of firn density have been proposed. Most of these have relied on tuning using measured depth-density profiles, which inherently invokes a steady-state assumption (Sorge's Law; Bader, 1954). Notable exceptions are the models proposed by Arthern and others (2010), who used measurements similar to ours from several sites in Antarctica, and Morris and Wingham (2014), who used neutron-density-probe measurements to derive compaction rates.

Nearly all firn densification models assume an Arrhenius temperature relationship, but the activation energy is still debated. Herron and Langway (1980) found activation energies of 10.16 and 21.4 kJ mol^{-1} for the two zones of firn densification. Li and Zwally (2002, 2004) suggested

that the activation energy is a function of the temperature, which is supported by laboratory work (Scapozza and Bartelt, 2003). Arthern and others (2010) found different optimal activation energies to describe their data at different sites, but their model uses a value of 60 kJ mol^{-1}, consistent with the value commonly used for ice deformation (Cuffey and Paterson, 2010, p. 64) and the value reported for lattice diffusion in laboratory experiments (Petrenko and Whitworth, 1999). The Arthern and others (2010) model also includes a second activation energy, however, associated with grain growth, which yields an effective activation energy close to 20 kJ mol^{-1} in a steady-state. Morris and Wingham (2014) found optimal activation energies near 110 kJ mol^{-1}. This range of reported values corroborates the idea that there are numerous microphysical processes driving firn densification, and these processes can have different activation energies that are additive or subtractive.

We used the FirnCover compaction-rate and core-density data to derive a relationship describing the densification rate of firn. Our data limit us to considering densification in the shallow firn. Following Herron and Langway (1980) and Arthern and others (2010), we assume the relationship has the form

$$\frac{d\rho}{dt} = c(\rho_i - \rho) \tag{4.1}$$

where ρ is the density (units kg m^{-3}), ρ_i is the ice density, and t is time in seconds, and we also assume that the firn behaves as a Newtonian fluid, i.e. the strain rate is linearly proportional to the stress. We assume that c has the form

$$c = \frac{ke^{\left(-\frac{Q}{RT}\right)}}{\tau}\,\sigma \tag{4.2}$$

where k is a tunable constant (Pa-1), Q is the activation energy (kJ mol-1), T is the temperature (K), R is the gas constant, σ is the stress (Pa), and τ is the age of the firn in seconds. We recognize

that numerous microphysical processes operate in densifying the firn, and those processes typically stiffen the firn through time. In the absence of necessary data to inform us of those processes, we use the age of the firn as a proxy for unconstrained microphysics. This is similar to the method employed by Arthern and others (2010), who included time-dependent grain growth into their model, and to Morris and Wingham (2014), who included a 'temperature-history function'. Assuming a steady-state temperature, that function is proportional to the age. Likewise, the simplified Arthern and others (2010) model,

$$\frac{d\rho}{dt} = 0.07\dot{b}g \exp\left(-\frac{E_c}{RT} + \frac{E_g}{RT_{av}}\right)(\rho_i - \rho), \tag{4.3}$$

is of the same form as our model, recognizing that stress $\sigma = \dot{b}g\tau$, and that for a given site $\frac{E_g}{RT_{av}}$ is constant. In the above equations, ρ is the density, $\dot{b}$ is the accumulation rate in kg m^{-3}, g is gravity, E_c is the activation energy for self-diffusion of water molecules through the ice lattice, R is the gas contant, T is the firn temperature, E_g is the activation energy for grain growth, T_{av} is the mean annual temperature, τ is the age of the firn, and ρ_i is the ice density.

We first tuned our model for Summit and found an optimal value $Q = 70$ kJ mol^{-1} and $k = 7.2 \times 10^9$ Pa^{-1}. Assuming that $Q = 70$ kJ mol^{-1} was applicable for all sites, we found best-fit values for *k* for EastGRIP, and NASA-SE. We found that optimal values of *k* varied by site, and we propose $k = -1.387 \times 10^{10} \times \dot{b} + 1.042 \times 10^{10}$ Pa^{-1}, where $\dot{b}$ is the accumulation rate in m a^{-1} (ice equiv.). More details of the tuning are given in Appendix A2. For zone 2 densification, below 550 kg m^{-3}, we use the densification equation proposed by Kuipers Munneke and others (2015).

Our model predicts the observations well at Summit, with RMS errors of 6% and 8% in the 8-m holes, but it does not outperform all of the other models (e.g., the Simonsen and others (2013) model shows similar performance). It should also not be expected to be the best model at Summit because it is formulated using the FirnCover data but then forced with RACMO data to produce results, and the RACMO climate has uncertainties associated with it. Our model does not perform as well at EGRIP; in the holes extending from the surface it performs on par with the other models, but it is worse in the deeper virtual holes. Similarly, At NASA-SE it predicts compaction rates in certain holes as well as or better than the other models (e.g. Instrument 109) but much poorer in others (e.g. the 2-m hole; Instrument 14).

We emphasize that this formulation is tuned for shallow firn at Summit and extended to EastGRIP and NASA-SE. The model's imperfect performance at NASA-SE and EastGRIP shows its limited applicability. The tuning of k is based on only three sites; NASA-SE has a very high accumulation rate, and thus the slope of the line is largely dependent on its optimal value of k. The model also relies on a depth-age scale inferred from the Herron and Langway (1980) model, which may be a poor assumption. There is additional uncertainty from assuming that the stress and density does not change through time. For the deeper holes, this assumption is reasonable, but for the shallowest holes (e.g. the 2-m hole at NASA-SE) the stress at the bottom of the hole increases greatly through the year.

4.6 DISCUSSION AND IMPLICATIONS

The firn model that best predicts the compaction rate varies by site, and for a particular site one model may perform best over some depth intervals, where as another model may perform better over a different depth interval. This result corroborates other work (e.g. Lundin and others, 2017) suggesting that our understanding of the physics of firn densification is incomplete. The RMS

errors of the best-performing models are greater than 5% of the mean annual compaction rates in the best cases (e.g. our proposed model at Summit) but can be greater than 20%.

Unfortunately, it is not possible to pick a universal 'best' model, nor can we assert a universal uncertainty in firn models. For example, the application of Crocus to NASA-SE gives an RMS error of ~6% in a 16-m hole, but at EastGRIP it produces an RMS error of 28%. The mean RMS error of the Kuipers Munneke and others (2015) model, which is frequently used for Greenland, for the 16-m holes at the three sites is 16%.

All of the models perform poorly in the shallowest firn, suggesting that physical mechanisms not represented in the models are important at those depths. We suggest that these mechanisms are likely related to temperature-gradient metamorphism. Our data do not include measurements of compaction in deep firn, though the interannual variability due to temperature and accumulation variability are not present at that depth. It is interesting that the models have large errors for the deep 'virtual' holes. At Summit (Figure 4.5, Instrument 102), this may be due to the model predicting warmer-than-observed firn, but at NASA-SE (Figure 4.7, Instrument 108) there is no obvious cause for the data-model mismatch.

It is clear from our results that there is still significant uncertainty in our understanding of the physics of firn densification. Each model represents those physics through various parameterizations and tunable parameters. Our measurements do corroborate Arthern and others' (2010) work showing that the effective activation energy is 60,000 kJ mol^{-1}. For our model we find a slightly higher value. Our model tuning showed that a higher activation, as suggested by Morris and others (2014) predicts too large of a seasonal cycle in compaction rates. Our model and the models based on the Arthern and others (2010) model (Ligtenberg and others, 2011; Simonsen and others, 2013; Kuipers Munneke and others, 2015) all predict seasonal cycles that are of

comparable amplitude to the data. This effective activation points to lattice diffusion as a dominant sintering mechanism, but it may also be the sum of a number of competing processes with different activation energies.

The three sites that we are considering here are relatively dry. At Crawford Point, where there is more melt, the models fail to predict compaction rates well, which is likely due to the amount of melt. The model predicts ice lenses that are thicker than observed, which produce modeled compaction rates much lower than observed. This stresses the importance of capturing the physics of percolation, refreezing and runoff correctly in the model; this problem at Crawford Point may be specific to the CFM's bucket scheme, or it may plague bucket models in general. Unfortunately, this model failure prevents us from assessing the applicability of dry-firn physics to wet firn. We did run the CFM for Crawford Point using our proposed model with no melt; the model predicts the depth-density profile reasonably well, but in that case it also predicts compaction rates that are much too high. This is not surprising; the ice layers are expected to stiffen the firn in a bulk sense; additionally, preferential-flow conduits have the potential to alter the compaction rate over a large spatial area; the heat they deliver to deeper firn could soften it, but the refrozen conduits could also act a rebar and stiffen the firn in a bulk sense.

It is also important to note that the modeled compaction rates are produced by forcing the model with RCM outputs. If a model is tuned to fit firn data using RCM climate outputs, as we have partially done, the firn model may be calibrated to predict firn data well with biases inherent to that RCM. The results may be different if we forced the model with outputs from different RCMs (e.g. MAR (Fettweis and others, 2017) or HIRHAM (Lucas-Picher and others, 2012)) or with in situ meteorological data. The use of the latter is prohibitive because of the dearth of observations on the ice sheet; modeling firn compaction over the ice-sheet for a correction to

altimetry products requires an ice-sheet wide climate product, which can only be provided by an RCM.

4.7 CONCLUSIONS

We observed firn density and stratigraphy, temperature, and compaction rates at a network of eight sites in the Greenland ice sheet's accumulation zone. The network includes sites in the dry-firn, percolation, and wet-firn zones. We compared the measurements outputs produced by nine different firn-densification models coupled to a meltwater-percolation model within the framework of the Community Firn Model.

We found that no single model predicts compaction rates or depth-density profiles best at each site. The uncertainty in modeled compaction rates is near or greater than 10% in most cases for the top 16 m of firn. The inconsistent performance of the models at the dry sites suggests that we still have an incomplete understanding of the physics of dry firn compaction. Our findings corroborate research by Arthern and others (2010) on the temperature sensitivity of firn: that study found that an activation energy of 60 kJ mol^{-1}, where we found an optimal value of 70 kJ mol^{-1}.

The CFM showed mixed performance predicting temperature, which points to uncertainty in the forcing data from RCMs. Likewise, some model-data mismatch in the depth-density profiles and compaction rates is likely attributable to RCM-data error. In order to reduce the uncertainty in firn-model outputs, it is essential to both improve the RCM products and to know the uncertainties and biases implicit to the RCM output.

Simulating wet firn is an important challenge for the firn-modelling community, especially as the area of Greenland that undergoes annual melt increases. It is not necessarily true that the physics of dry firn densification apply to wet firn; certainly, some of the same physics are at play, but we cannot rule out the possibility that other mechanisms are important in wet firn that alter the

equations we use to describe densification. The existence of preferential-flow conduits also makes this a two-dimensional problem, where most firn models are one dimensional. Schemes that parameterize preferential flow in a one-dimensional framework hold promise, but we are still challenged by lack of data about the spatial distribution and depth of conduits, which has implications for the redistribution of heat and mass.

In order to improve firn models, we need to strive to better understand the microphysical processes that are driving macroscale firn densification. Targeted field campaigns in dry-firn zones should measure microstructural parameters in addition to bulk density and compaction rates, and new instruments such as phase-sensitive radar hold promise for measuring compaction rates on much finer spatial (depth) scales. In wet-firn zones, field work is needed to understand the distribution of preferential flow conduits and the fate of meltwater.

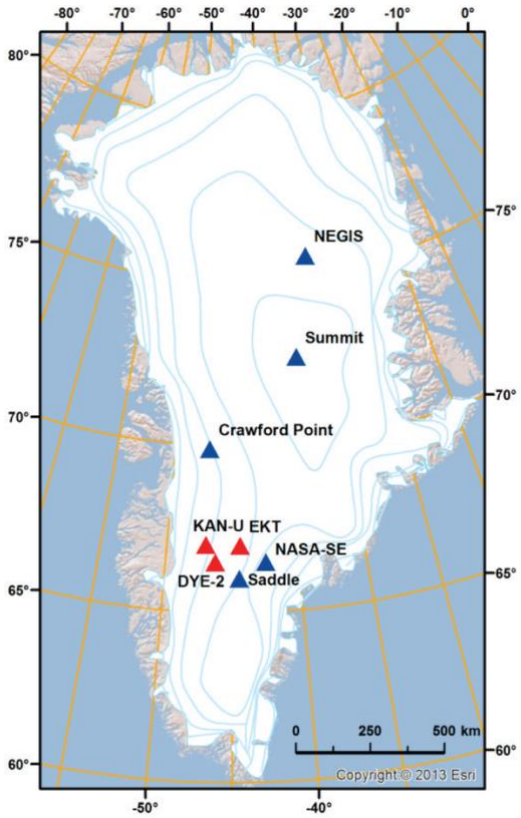

Figure 4.1. Locations of the FirnCover sites. Red sites were first instrumented in 2013; blue in 2015.

Table 4.1. FirnCover site characteristics. The annual accumulation and melt rates are the values predicted by the regional climate model RACMO2.3p2 at the grid point nearest the site. The 4 values in the annual temperature column are the FirnCover 2016 mean annual air temperature, RACMO2.3p2 mean annual temperature, the mean temperature at ~10 m depth measured by the FirnCover RTD strings since installation, and the mean 10-m temperature predicted by the CFM since 2015.

Site Name	**Latitude**	**Longitude**	**Elevation (m)**	**Annual Temperature (°C)**	**Annual Accum. (m i.e. a^{-1})**	**Annual Melt (m i.e. a^{-1})**
KAN-U	67.0004	47.0247	1840	-14.0 / -16.4 / -9.1 / NA	0.59	0.58
Crawford Point	69.8765	47.0289	1942	-16.2 / -18.9 / NA / -15.4	0.50	0.23
DYE-2	66.4777	46.2861	2126	-17.6 / -18.1 / -12.8 / -12.0	0.53	0.28
EKT	66.9941	44.3854	2355	-18.7 / -20.3 / -17.6 / -16.4	0.49	0.11
NASA-SE	66.4779	42.4964	2375	-18.1 / -20.1 / -17.0 / -17.1	0.68	0.048
Saddle	65.9993	44.5023	2455	-18.1 / -20.3 / -17.9 / -18.9	0.47	0.095
EastGRIP	75.6251	35.9794	2661	-27.3 / -28.3 / -29.0 / -26.9	0.14	0.004
Summit	72.5774	38.4692	3203	-26.2 / -28.2 / -29.0 / -27.6	0.23	0.0

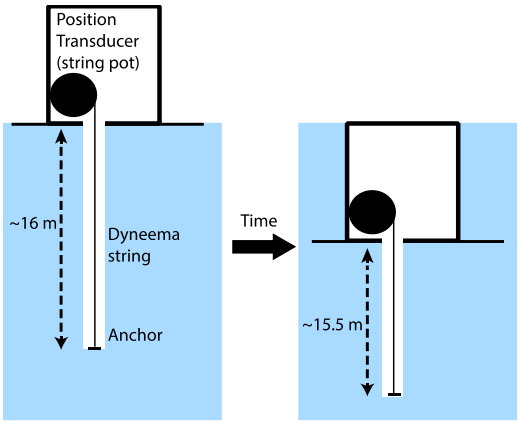

Figure 4.2. Cartoon of the ‘coffee-can’ firn compaction instruments. An anchor is secured at the bottom of a borehole. A string is attached to the anchor and a potentiometer at the surface. As the firn compacts, the potentiometer measures the length of string that it reels in.

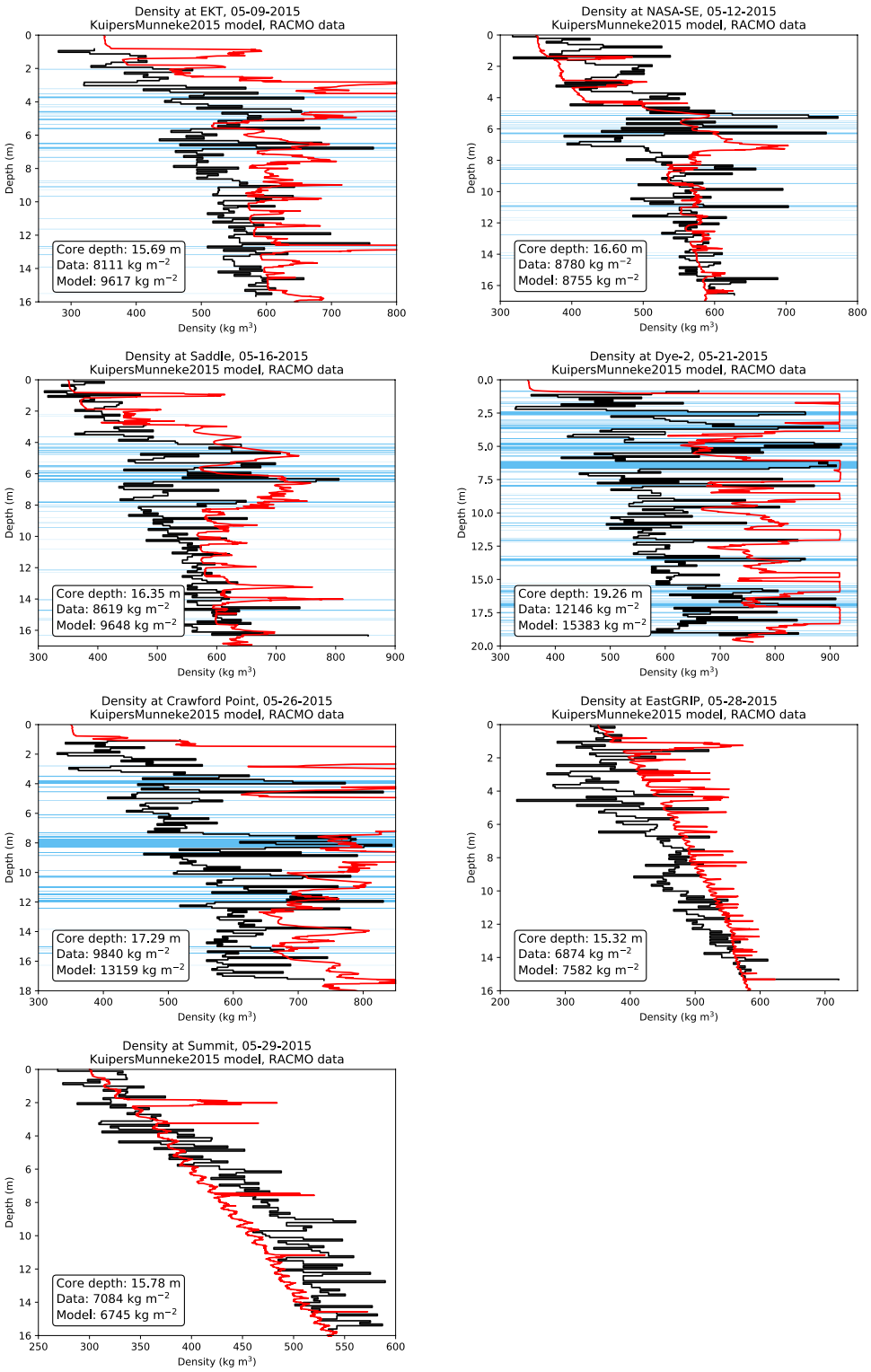

Figure 4.3. Depth-density profiles at the eight FirnCover sites in 2015: (black) measured and (red) predicted by the Kuipers Munneke and others (2015) model. Horizontal blue lines show observed ice lenses. Note different scales on each panel.

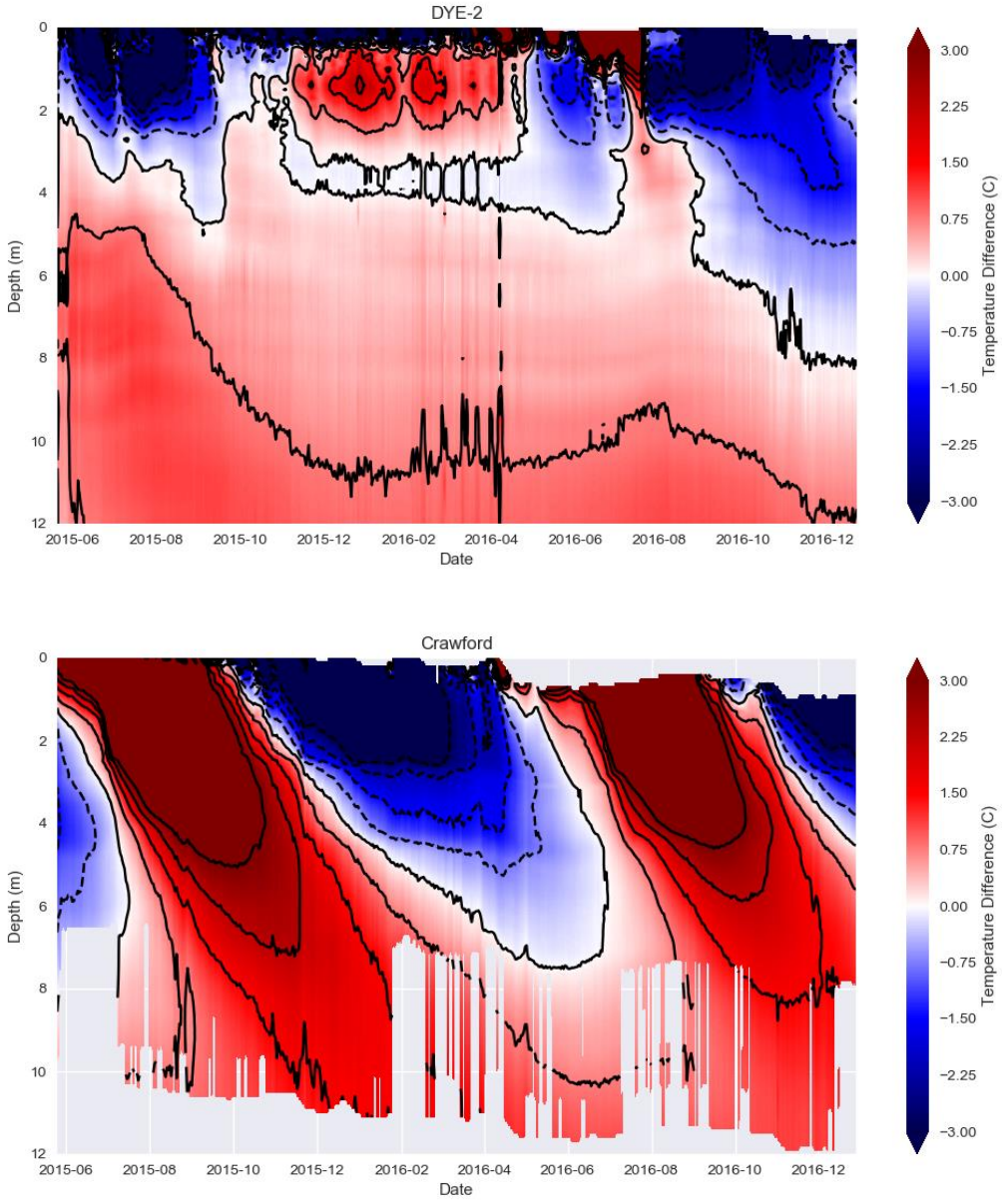

Figure 4.4. Modeled minus measured temperature profiles for DYE-2 and Crawford Point. Blue colors show when and where the model is colder than the measurements, reds indicate that the model is warmer.

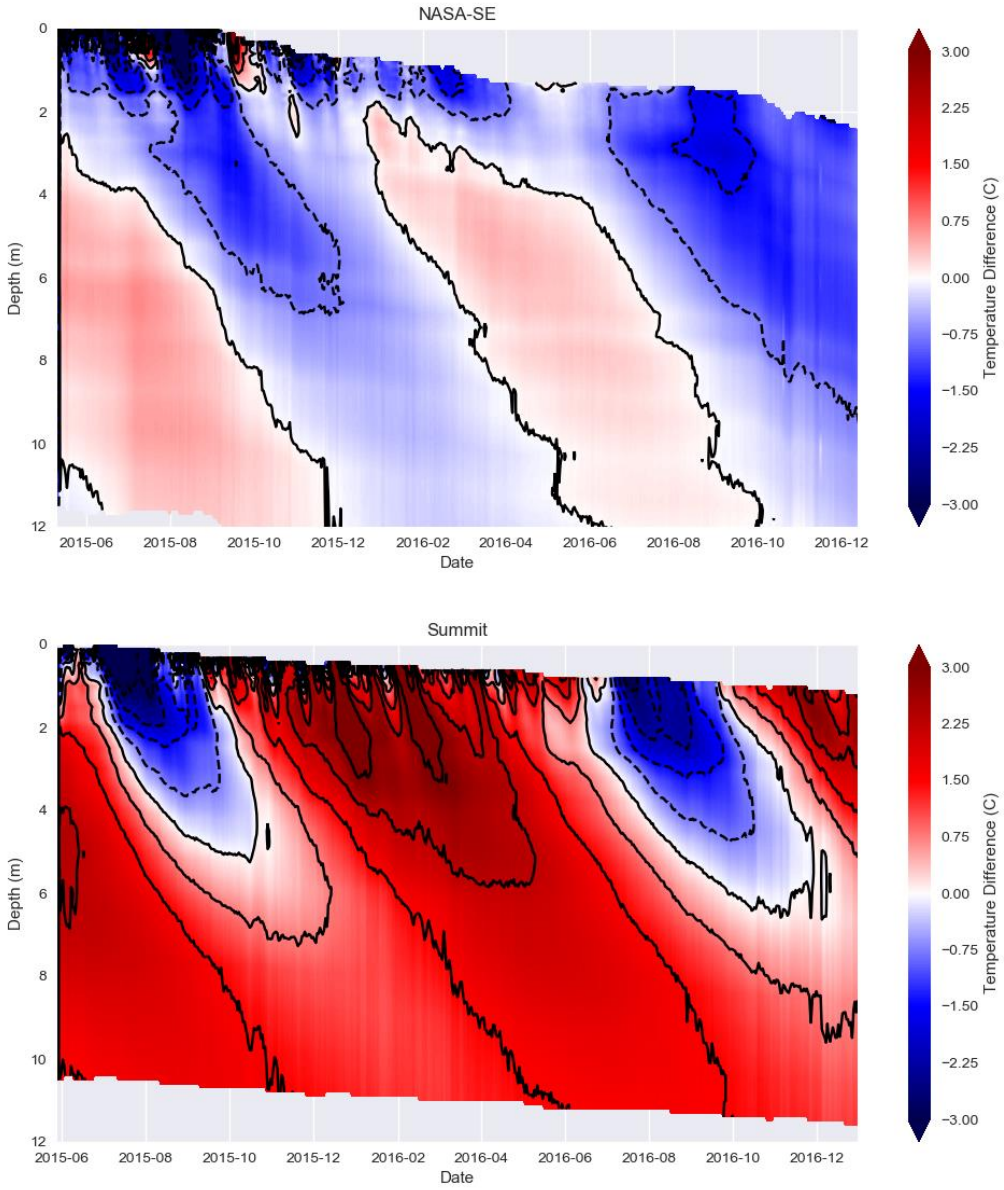

Figure 4.4, continued. Modeled minus measured temperature profiles for NASA-SE and Summit. Blue colors show when and where the model is colder than the measurements, reds indicate that the model is warmer.

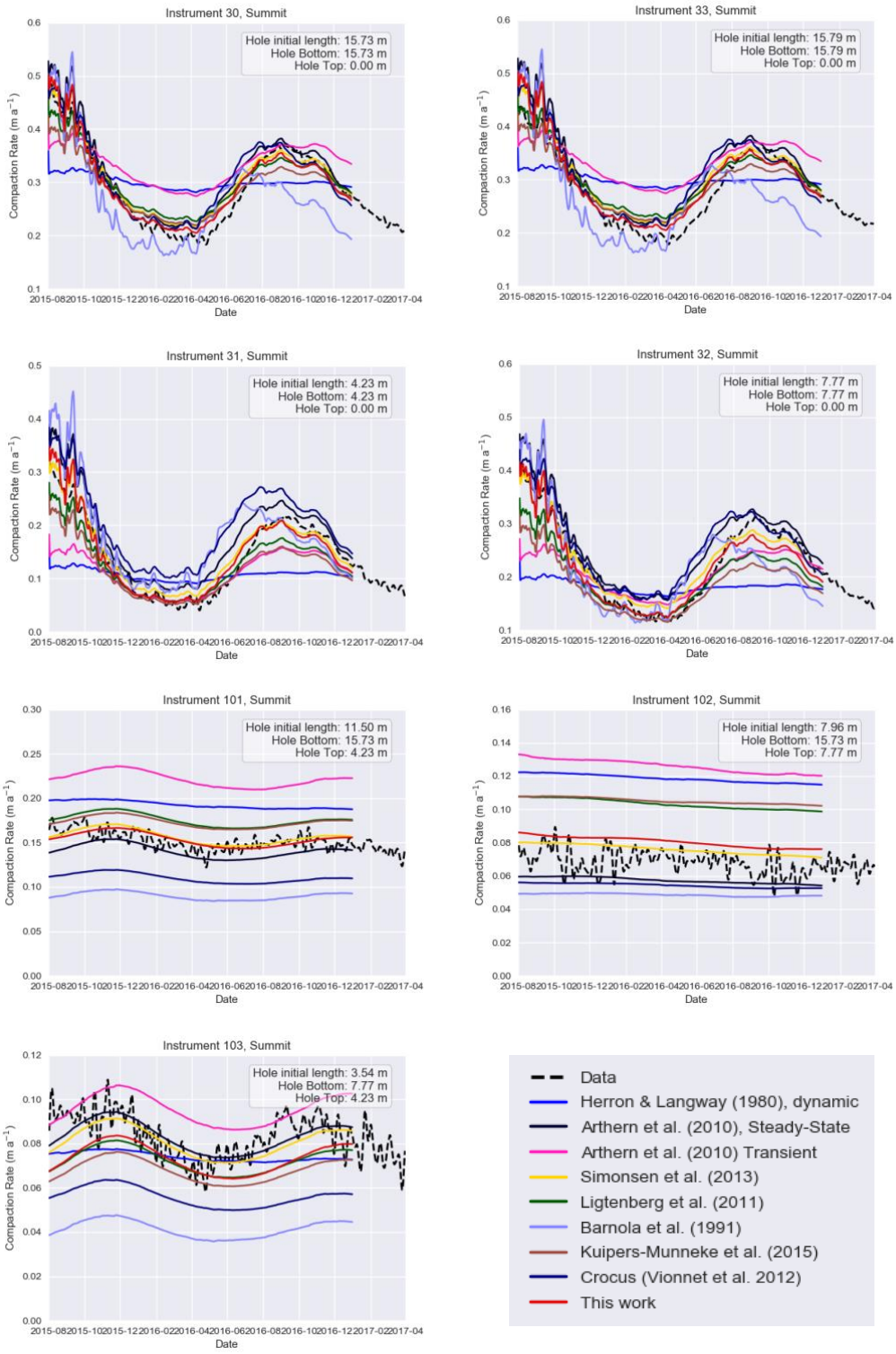

Figure 4.5. Measured and modeled firn compaction rates at Summit.

Table 4.2. RMS errors (%) for the models at Summit.

	30	**31**	**32**	**33**	**101**	**102**	**103**
Arthern2010S	9.45	28.91	17.19	13.81	8.88	17.67	8.46
Arthern2010T	19.24	35.92	21.6	20.49	43.82	79.91	16.55
Barnola1991	19.11	43.41	23.26	19.74	39.36	28.65	49.93
Crocus	9.84	45.05	17.68	13.18	26.86	21.41	33.61
HLdynamic	22.57	52.43	36.8	21.5	25.84	69.79	15.5
KuipersMunneke2015	10.15	27.61	24.13	8.57	14.1	51.58	20.68
Ligtenberg2011	8.56	19.86	17.35	9.28	15.54	48.88	16.05
Max2018	5.77	13.15	9.56	8.33	5.47	18.97	15.25
Simonsen2013	6.9	13.09	8.56	9.76	5.81	13.97	9.35

Table 4.3. RMS errors (%) for the models at EastGRIP.

	26	**27**	**28**	**29**	**104**	**105**	**106**
Arthern2010S	25.07	46.18	25.06	24.91	39.73	39.19	46.06
Arthern2010T	21.75	47.46	26.25	19.94	28.92	10.77	19.98
Barnola1991	27.97	45.58	29.73	28.56	37.12	39.47	49.29
Crocus	28.28	44.26	28.81	28.28	40.06	38.44	44.63
HLdynamic	35.24	75.06	49.14	34.52	18.98	14.62	33.04
KuipersMunneke2015	29.72	51.78	36.01	29.61	23.17	22.99	35.46
Ligtenberg2011	26.42	46.59	29.83	26.14	27.74	23.77	31.38
Max2018	31.07	45.37	28.32	31.35	50.06	47.81	51.8
Simonsen2013	24.19	44.03	25.74	23.74	33.26	27.19	31.63

Table 4.4. RMS errors (%) for the models at NASA-SE.

	13	**14**	**15**	**16**	**107**	**108**	**109**
Arthern2010S	29.77	20.33	41.24	29.66	42.21	10.72	69.86
Arthern2010T	39.51	65.06	43.05	38.4	75.95	31.92	108.7
Barnola1991	16.9	67.03	19.65	17.25	7.43	14.82	18.77
Crocus	6.62	68.66	6.98	6.89	19.66	16.54	44.08
HLdynamic	15.43	70.82	20.18	14.81	12.3	21.75	35.83
KuipersMunneke2015	11.29	63.98	9.01	11.31	11.09	20.18	29.96
Ligtenberg2011	8.18	62.31	7.06	8.6	14.84	15.28	33.08
Max2018	17.46	83.64	32.52	18.25	11.51	21.23	10.61
Simonsen2013	11.72	26.67	24.68	11.83	23.27	22.66	53.86

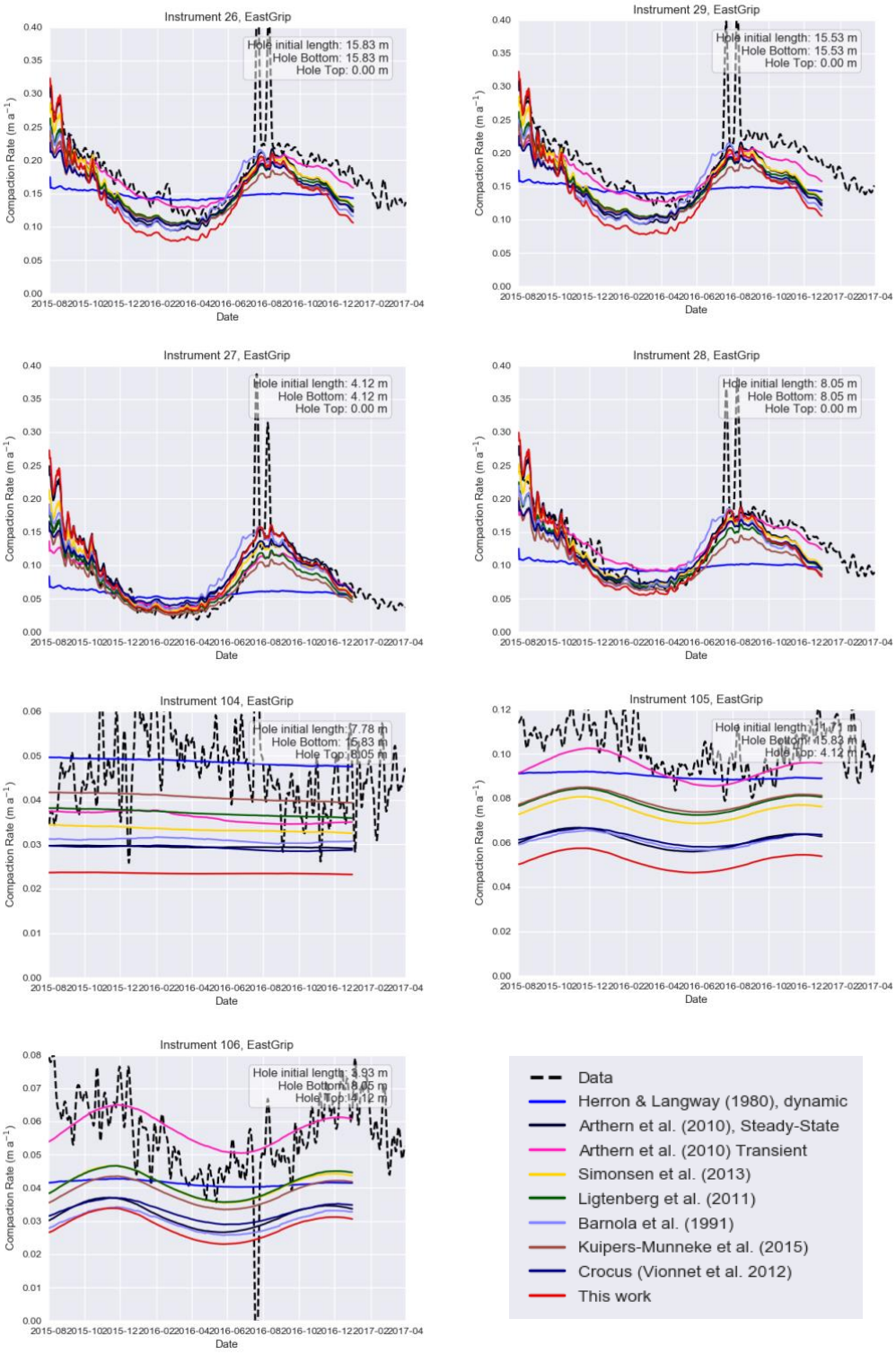

Figure 4.6. Measured and modeled firn compaction rates at EastGRIP.

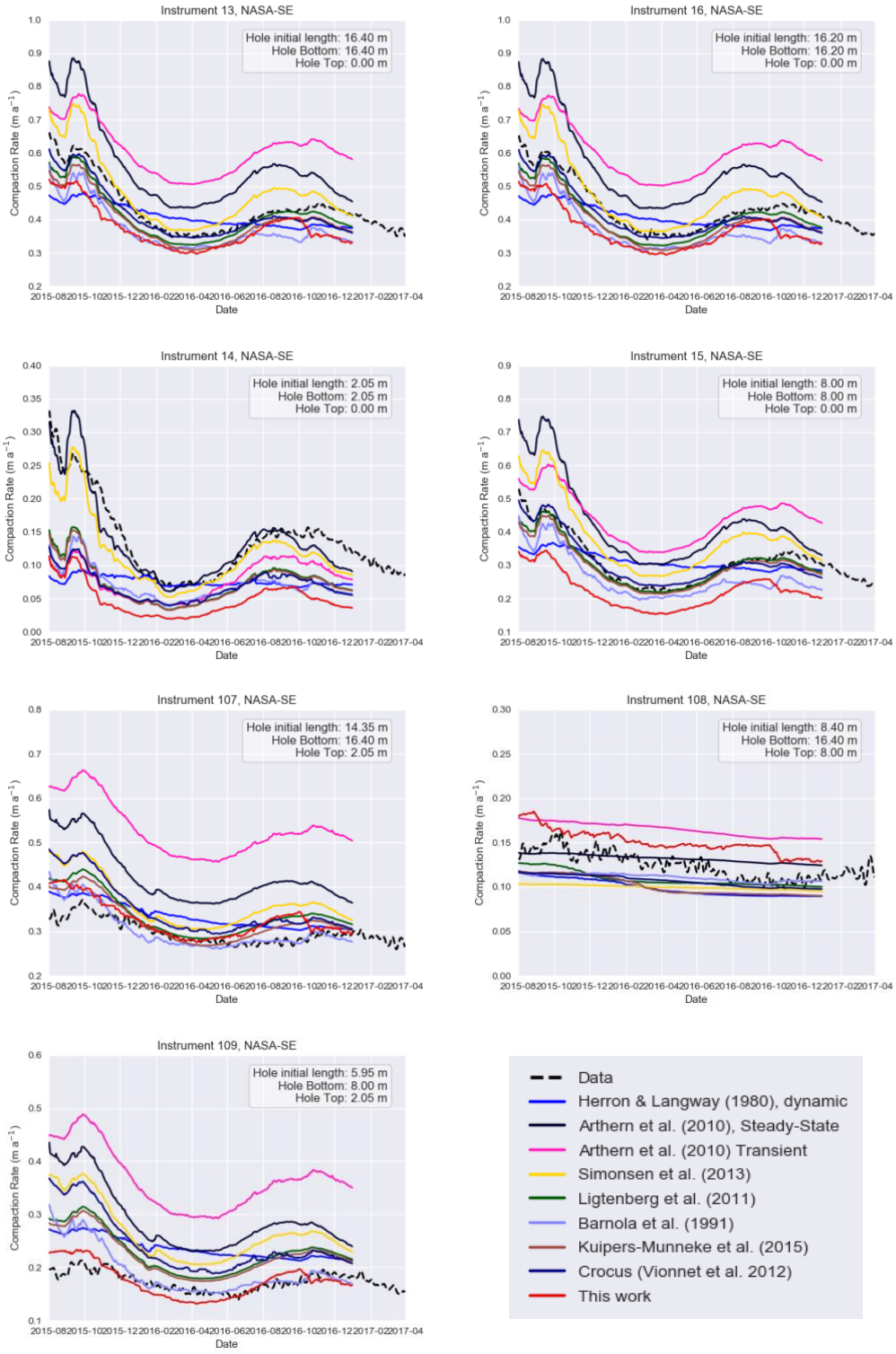

Figure 4.7. Measured and modeled firn compaction rates at NASA-SE.

Chapter 5. SYNTHESIS AND CONCLUSIONS

5.1 SUMMARY

The work presented in this dissertation has addressed a number of questions about physical processes in polar firn, including gas transport and densification. Modeling these physical processes has important applications in ice-core science and for ice-sheet mass-balance calculations. Central to the work is the Community Firn Model (CFM), of which I led the development. The CFM's modular structure allowed me to explain δ^{15}N data from the GISP2 ice core had not been previously explained, to intercompare firn-densification models, and compare those models to data.

In Chapter 2, I coupled a firn-air model to a firn densification model; this is the first time that has been done. I used the coupled system to investigate the processes that create the lock-in zone and concluded that it is likely that a combination of small-scale layering and diffusion/advection timescales contribute. I also showed that firn thickening during warming events in Greenland could explain δ^{15}N and δ^{40}Ar data observed in the GISP2 ice-core. Finally, I showed how a surface-melt layer (i.e. ice lens) would affect δ^{15}N and CO_2 records in an ice core. Broadly, this work showed that including non-steady-state firn processes improves models of firn-air transport.

In Chapter 3, I compared output from 11 published firn-densification models for Summit, Greenland and tested the models' sensitivity to the initial and boundary conditions. This work corroborated and extended our work in Lundin and others (2017), showing that the existing models do not agree well: they do not satisfactorily predict the firn-air content at Summit well, nor do they agree how much the air content in the firn has changed in the last several decades. The model

predictions also vary depending on the climate forcing, suggesting that a significant amount of uncertainty in firn-model predictions results from uncertainties in regional climate models.

In Chapter 4, I used the data from the FirnCover project to test how well firn models predict observations when forced by output from a regional climate model. The complete suite of FirnCover measurements allowed us to make a more-complete examination of firn-model performance than previous studies, which often considered matching models to only depth-density profiles.

We found that our bucket schemes for meltwater percolation did not work well at wet-firn sites, which may be related to how the model transports the meltwater, the firn-densification equation not being calibrated for wet firn, or the amount of melt predicted by the Regional Climate Model (RCM) being incorrect. We also found that existing firn-densification models are inconsistent in their ability to predict firn compaction rates; no model predicted the compaction best at all of our sites, and at any given site, different models performed best at different depths in the firn. These results suggest that firn models are not yet representing physical processes correctly. In attempt to improve model fits to our new data I derived a new firn-densification model for Summit. The activation energy that I found for our model is close to the value previously reported by Arthern and others (2010).

5.2 CONTRIBUTIONS

The work I have presented in this dissertation makes a number of meaningful contributions to the glaciological community, which I outline here.

The Community Firn Model (CFM)

The CFM was motivated by the ice-core community's desire for a 'community firn model'. Although we never came up with a cleverer name, the name 'Community Firn Model' is an

accurate portrayal. Our goal was to produce an open-source model framework that would be be useful. This was a non-trivial task, but I am proud of the end result, and our efforts paid off: several research groups worldwide have used it and, in the community spirit, added to the CFM. Other groups have asked me to provide model output for them.

Air transport in non-steady-state firn

I am the first person to couple a firn-air model to a firn-densification model. This feature has allowed me to address questions that previously could not be investigated with prior models. Previous work (Severinghaus and Brook, 1999) hypothesized that data-model mismatch in the δ^{15}N and δ^{40}Ar data in the GISP2 ice core was due to the use of a steady-state firn model; my work was able to confirm that hypothesis. This model will be especially useful to groups investigating anomalous data from ice cores that could be explained by firn processes.

Identifying weaknesses and uncertainty in firn models

Much of the work I have presented involves assessing firn-model uncertainties. In Chapter 3 I intercompared models, and in Chapter 4 I used the data from the FirnCover project to test how well firn models can predict observations. The conclusions in these two chapters were similar and corroborated our findings in Lundin and others (2017): no single model is universally the best. My analyses provide those using firn model outputs with a robust estimate of the uncertainties.

Measured firn-compaction rates in Greenland

The firn-compaction-rate data that we collected with the FirnCover project, presented in Chapter 4, are spatially and temporally extensive. Very few measurements of firn compaction in polar regions exist yet knowing the firn compaction rate at high temporal resolution is essential for correcting surface-elevation measurements derived from altimetry. This data set is a valuable contribution to all groups developing and using firn-densification models.

A new firn-densification equation for Summit, Greenland

In Chapter 4 we used the FirnCover data to derive a new firn-densification equation for Summit. The equation gives slightly better results than other models at Summit, but it does not do as well at other sites. The broad contribution of this is that we found a model form similar to previously published models. The effective activation energy we found, 70 kJ mol^{-1}, is similar to that reported by Arthern and others (2010) (60 kJ mol^{-1}), and we also found that including an age term improves the fit to data. This paves the way for future model improvement.

5.3 FUTURE RESEARCH DIRECTIONS

Much of the work that I have done for this dissertation has focused on assessing uncertainty associated with firn models. Ice cores are being sampled at higher resolution, ice-sheet surface elevations are being measured more accurately, and the areal melt extent of Greenland is growing. Firn models are essential to interpreting these data, and there is much firn research still to be done.

The work that I have done during my graduate tenure has very much followed in the footsteps of others, which is of course inevitable in science and is a good thing. In learning to be a scientist, my tack was to follow what others have done and put my own spin on it, e.g. using the same technique as Arthern and others (2010) to derive my firn model and explaining the stable isotope data from Severinghaus and Brook (1999). Now, at the end of my PhD studies, I can think more creatively as a scientist (which perhaps is a good sign that I am deserving of a PhD), and I can think of a number of research questions that would make for more interesting work.

Here, I outline several research directions that stem from the work I have presented in this dissertation. Some are specific problems that I will address as a post-doc, and some are broader problems that the firn community should address. A common theme is that we need to understand

what firn is doing at a smaller scale than we have previously, which requires better knowledge of firn microstructure and its evolution.

A constitutive relationship for firn at the South Pole

I have been fortunate to participate in a project measuring firn compaction at the South Pole. These data are similar to those collected with the FirnCover project in Greenland, but they are unique in that (1) they are the first continuous measurements of firn compaction on the East Antarctic plateau, (2) they are measuring firn compaction over the full depth of the firn, and (3) they are complemented by microstructure measurements by micro-CT scans. This suite of measurements will allow us to test firn-model performance in East Antarctica; this has not been done previously. Additionally, we will be able to formulate a model describing compaction at that site in both firn-densification zones, addressing open questions about the activation energy. The microstructure measurements will be incorporated into the model, avoiding the generic age parameter that we have used in this work.

Firn compaction along a flow line

The South Pole ice core was drilled along a flow line, rather than at a divide or on a dome. Lilien and others (2018) showed that annual-layer-thickness variability in Holocene ice in the core could be explained by accumulation variability upstream along the flow line. A clear next step is to use the CFM to model firn densification and gas transport along the flow line; we hypothesize that the $\delta^{15}\mathrm{N}$ variations in the ice core can be explained by firn-thickness changes resulting from accumulation-rate variability along flow.

Siple Dome ice-core interpretation

The Siple Dome ice core shows a number of anomalous, difficult-to-interpret features. One possible explanation is that a melt event could have altered the isotopes in the firn. The CFM could be used to explore this hypothesis by coupling the meltwater and water-isotope diffusion modules.

A physically-based firn-densification model

It is likely that firn-densification models will always be somewhat empirical. However, measurements similar to those we are doing at South Pole may help us better understand the microphysics of firn densification, i.e. what mechanisms are dominating densification in different temperature and density realms. Understanding these microphysical mechanisms may allow us to model firn densification at the grain scale. Scaling such a model to operate over an entire ice sheet may not be practical, but such a model will also help create more universal parameterizations to be included in a macroscale firn-densification model, rather than relying on tuning to depth-density profiles.

Snow models and firn

The top meter of ice sheets is more accurately described as snow rather than as firn, and likely different physical processes are important for its densification and metamorphism than in firn; likewise, we showed in Lundin and others (2017) that snow models do not work well for firn. Coupling a snow model to the upper part of the CFM's domain may help reduce uncertainty in that zone.

A 3-dimensional firn model for meltwater

I have demonstrated that modeling meltwater percolation in a 1-dimensional model is a challenge. Future work needs to approach this problem in a 2- or 3-dimensional framework that allows for both heterogeneous and homogenous flow.

Field campaigns in the wet-firn zones of Greenland and Antarctica

In addition to models capturing 3-D meltwater percolation, field campaigns are needed to actually measure the meltwater flow through firn, especially the spatial distribution of preferential-flow conduits, how much heat and mass those conduits transport, and where they deliver it. These studies are needed both to improve firn-meltwater models and to help improve RCM outputs.

BIBLIOGRAPHY

Abdalati W and Steffen K (2001) Greenland Ice Sheet melt extent: 1979-1999. *J. Geophys. Res. Atmos.* **106**(D24), 33983–33988 (doi:10.1029/2001JD900181)

Adolph AC and Albert MR (2014) Gas diffusivity and permeability through the firn column at Summit, Greenland: Measurements and comparison to microstructural properties. *Cryosphere* **8**(1), 319–328 (doi:10.5194/tc-8-319-2014)

Alley RB (1987) Firn densification by grain-boundary sliding : a first model. *Le J. Phys. Colloq.* **48**(C1), C1-249-C1-256 (doi:10.1051/jphyscol:1987135)

Alley RB (1999) GISP2 Stratigraphy. *PANGAEA* (doi:10.1594/PANGAEA.56103)

Alley RB (2004) GISP2 ice core temperature and accumulation data. *IGBP PAGES/World Data Cent. Paleoclimatology Data Contrib. Ser.* **13**, 2004

Alley RB, Meese DA, Shuman CA, Gow AJ, Taylor KC, Grootes PM, White JWC, Ram M, Waddington ED, Mayewski PA and Zielinski GA (1993) Abrupt increase in Greenland snow accumulation at the end of the Younger Dryas event. *Nature* **362**(6420), 527–529 (doi:10.1038/362527a0)

Arlt E (1982) The influence of an increasing particle coordination on the densification of spherical polders. *Acta Metall.* **30**(10), 1883–1890 (doi:10.1016/0001-6160(82)90028-1)

Arnaud L, Barnola J-M and Duval P (2000) Physical modeling of the densification of snow/firn and ice in the upper part of polar ice sheets. *Physics of Ice Core Records*. 285–305 http://eprints2008.lib.hokudai.ac.jp/dspace/handle/2115/32472

Arthern RJ, Vaughan DG, Rankin AM, Mulvaney R and Thomas ER (2010) In situ measurements of Antarctic snow compaction compared with predictions of models. *J. Geophys. Res.* **115**(F3) (doi:10.1029/2009JF001306)

Van As D, Mikkelsen AB, Nielsen MH, Box JE, Liljedahl LC, Lindbäck K, Pitcher L and Hasholt B (2017) Hypsometric amplification and routing moderation of Greenland ice sheet meltwater release. *Cryosphere* **11**(3), 1371–1386 (doi:10.5194/tc-11-1371-2017)

Aschwanden A, Bueler E, Khroulev C and Blatter H (2012) An enthalpy formulation for glaciers and ice sheets. *J. Glaciol.* **58**(209), 441–457 (doi:10.3189/2012JoG11J088)

Bader H (1954) Sorge's law of densification of snow on high polar glaciers. *J. Glaciol.* **2**(15), 319–323 (doi:10.3198/1954JoG2-15-319-323)

Barnola J-M, Pimienta P, Raynaud D and Korotkevich YS (1991) CO2-climate relationship as deduced from the Vostok ice core: a re-examination based on new measurements and on a re-evaluation of the air dating. *Tellus* **43B**(2), 83–90 (doi:10.1034/j.1600-0889.1991.t01-1-00002.x)

Battle MO, Bender M, Sowers T, Tans PP, Butler JH, Elkins JW, Ellis JT, Conway T, Zhang N, Lang P and Clarke AD (1996) Atmospheric gas concentrations over the past century measured in air from firn at the South Pole. *Nature* **383**(6597), 231–235 (doi:10.1038/383231a0)

Benson CS (1961) Stratigraphic studies in the snow and firn of the Greenland Ice Sheet. *Folia Geogr. Danica* **70**(August), 13–37

Berkelhammer M, Noone DC, Steen-Larsen HC, Bailey A, Cox CJ, O'Neill MS, Schneider D, Steffen K and White JWC (2016) Surface-atmosphere decoupling limits accumulation at Summit, Greenland. *Sci. Adv.* **2**(4), e1501704 (doi:10.1126/sciadv.1501704)

Birner B, Buizert C, Wagner TJW and Severinghaus JP (2017) The influence of layering and barometric pumping on firn air transport in a 2D model. *Cryosph. Discuss.* **2017**, 1–29 (doi:10.5194/tc-2017-233)

Blackford JR (2007) Sintering and microstructure of ice: a review. *J. Phys. D. Appl. Phys.* **40**(21), R355–R385 (doi:10.1088/0022-3727/40/21/R02)

Blunier T and Schwander J (2000) Gas enclosure in ice: age difference and fractionation. *Phys. Ice Core Rec.*, 307–326 http://eprints.lib.hokudai.ac.jp/dspace/handle/2115/32473

Buizert C (2011) The influence of firn air transport processes and radiocarbon production on gas records from polar firn and ice. University of Copenhagen.

Buizert C, Cuffey KM, Severinghaus JP, Baggenstos D, Fudge TJ, Steig EJ, Markle BR, Winstrup M, Rhodes RH, Brook EJ, Sowers T, Clow GD, Cheng H, Edwards RL, Sigl M, McConnell JR and Taylor KC (2015) The WAIS Divide deep ice core WD2014 chronology – Part 1: Methane synchronization (68-31 ka BP) and the gas age-ice age difference. *Clim. Past* **11**(2), 153–173 (doi:10.5194/cp-11-153-2015)

Buizert C, Martinerie P, Petrenko V V., Severinghaus JP, Trudinger CM, Witrant E, Rosen JL, Orsi AJ, Rubino M, Etheridge DM, Steele LP, Hogan C, Laube JC, Sturges WT, Levchenko VA, Smith AM, Levin I, Conway TJ, Dlugokencky EJ, Lang PM, Kawamura K, Jenk TM, White JWC, Sowers T, Schwander J and Blunier T (2012) Gas transport in firn: Multiple-tracer characterisation and model intercomparison for NEEM, Northern Greenland. *Atmos. Chem. Phys.* **12**(9), 4259–4277 (doi:10.5194/acp-12-4259-2012)

Buizert C and Severinghaus JP (2016) Dispersion in deep polar firn driven by synoptic-scale surface pressure variability. *Cryosphere* **10**(5), 2099–2111 (doi:10.5194/tc-10-2099-2016)

Christensen OB, Drews M, Christensen JH, Dethloff K, Ketelsen K, Hebestadt I and Rinke A (2007) The HIRHAM Regional Climate Model Version 5 (beta). *Tech. Rep. 06-17;*, 1–22 http://orbit.dtu.dk/fedora/objects/orbit:118724/datastreams/file_8c69af6e-acfb-4d1a-aa53-73188c001d36/content

Coble RL (1970) Diffusion Models for Hot Pressing with Surface Energy and Pressure Effects as Driving Forces. *J. Appl. Phys.* **41**, 4798 (doi:10.1063/1.1658543)

Cuffey KM and Paterson WSB (2010) *The physics of glaciers.*, 4th edn. Butterworth-Heinemann/Elsevier, Burlington, MA

Dahl-Jensen D, Albert MR, Aldahan A, Azuma N, Balslev-Clausen D, Baumgartner M, Berggren AM, Bigler M, Binder T, Blunier T, Bourgeois JC, Brook EJ, Buchardt SL, Buizert C, Capron E, Chappellaz J, Chung J, Clausen HB, Cvijanovic I, Davies SM, Ditlevsen P, Eicher O, Fischer H, Fisher DA, Fleet LG, Gfeller G, Gkinis V, Gogineni S, Goto-Azuma K, Grinsted A, Gudlaugsdottir H, Guillevic M, Hansen SB, Hansson M, Hirabayashi M, Hong S, Hur SD, Huybrechts P, Hvidberg CS, Iizuka Y, Jenk T, Johnsen SJ, Jones TR, Jouzel J, Karlsson NB, Kawamura K, Keegan K, Kettner E, Kipfstuhl S, Kjær HA, Koutnik M, Kuramoto T, Köhler P, Laepple T, Landais A, Langen PL, Larsen LB, Leuenberger D, Leuenberger M, Leuschen C, Li J, Lipenkov V, Martinerie P, Maselli OJ, Masson-Delmotte V, McConnell JR, Miller H, Mini O, Miyamoto A, Montagnat-Rentier M, Mulvaney R, Muscheler R, Orsi AJ, Paden J, Panton C, Pattyn F, Petit JR, Pol K, Popp T, Possnert G, Prié F, Prokopiou M, Quiquet A, Rasmussen SO, Raynaud D, Ren J, Reutenauer C, Ritz C, Röckmann T, Rosen JL, Rubino M, Rybak O, Samyn D, Sapart CJ, Schilt A, Schmidt AMZ, Schwander J, Schüpbach S, Seierstad I, Severinghaus JP, Sheldon S, Simonsen SB, Sjolte J, Solgaard AM, Sowers T, Sperlich P, Steen-Larsen HC, Steffen K, Steffensen JP, Steinhage D, Stocker TF, Stowasser C, Sturevik AS, Sturges WT, Sveinbjörnsdottir A, Svensson A, Tison JL, Uetake J, Vallelonga P, Van De Wal RSW, Van Der Wel G, Vaughn BH, Vinther B, Waddington E, Wegner A, Weikusat I, White JWC, Wilhelms F, Winstrup M, Witrant E, Wolff EW, Xiao C and Zheng J (2013) Eemian interglacial reconstructed from a Greenland folded ice core. *Nature* **493**(7433), 489–494 (doi:10.1038/nature11789)

EPICA members (2004) Eight glacial cycles from an {Antarctic} ice core. *Nature* **429**(6992), 623–628 (doi:10.1038/nature02599)

Fettweis X, Box JE, Agosta C, Amory C, Kittel C, Lang C, van As D, Machguth H and Gallée H (2017) Reconstructions of the 1900–2015 Greenland ice sheet surface mass balance using the regional climate MAR model. *Cryosph.* **11**(2), 1015–1033 (doi:10.5194/tc-11-1015-2017)

Forster RR, Box JE, Van Den Broeke MR, Miège C, Burgess EW, Van Angelen JH, Lenaerts JTM, Koenig LS, Paden J, Lewis C, Gogineni SP, Leuschen C and McConnell JR (2014) Extensive liquid meltwater storage in firn within the Greenland ice sheet. *Nat. Geosci.* **7**(2), 95–98 (doi:10.1038/ngeo2043)

Freitag J, Dobrindt U and Kipfstuhl J (2002) A new method for predicting transport properties of polar firn with respect to gases on the pore-space scale. *Ann. Glaciol.* **35**(1), 538–544 (doi:10.3189/172756402781816582)

Goujon C, Barnola J-M and Ritz C (2003) Modeling the densification of polar firn including heat diffusion: application to close-off characteristics and gas isotopic fractionation for Antarctica and Greenland sites. *J. Geophys. Res.* **108**(D24) (doi:10.1029/2002JD003319)

Gregory SA, Albert MR and Baker I (2014) Impact of physical properties and accumulation rate

on pore close-off in layered firn. *Cryosphere* **8**(1), 91–105 (doi:10.5194/tc-8-91-2014)

Hamilton GS, Whillans IM and Morgan PJ (1998) First point measurements of ice-sheet thickness change in Antarctica. *Ann. Glaciol.* **27**, 125–129

Harper JT, Humphrey N, Pfeffer WT, Brown J and Fettweis X (2012) Greenland ice-sheet contribution to sea-level rise buffered by meltwater storage in firn. *Nature* **491**(7423), 240–243 (doi:10.1038/nature11566)

Helsen MM, van den Broeke MR, van de Wal RSW, van de Berg WJ, van Meijgaard E, Davis CH, Li Y and Goodwin I (2008) Elevation changes in Antarctica mainly determined by accumulation variability. *Science* **320**(5883), 1626–9 (doi:10.1126/science.1153894)

Helsen MM, Van Den Broeke MR, Van De Wal RSW, Van De Berg WJ, Van Meijgaard E, Davis CH, Li Y and Goodwin I (2008) Elevation changes in antarctica mainly determined by accumulation variability. *Science (80-.).* **320**(5883), 1626–1629 (doi:10.1126/science.1153894)

Herron M and Langway C (1980) Firn densification: an empirical model. *J. Glaciol.* **25**(93), 373–385 (doi:10.1017/S0022143000015239)

Hörhold MW, Kipfstuhl S, Wilhelms F, Freitag J and Frenzel A (2011) The densification of layered polar firn. *J. Geophys. Res.* **116**(F1) (doi:10.1029/2009JF001630)

Hulbe CL and Whillans IM (1994a) A method for determining ice-thickness change at remote locations using GPS. *Ann. Glaciol.* **20**, 263–268 (doi:doi:10.3189/172756494794587348)

Hulbe CL and Whillans IM (1994b) A method for determining ice-thickness change at remote locations using GPS. *Annals of Glaciology* **20**, 263–268 (doi:doi:10.3189/172756494794587348)

Kawamura K, Severinghaus JP, Ishidoya S, Sugawara S, Hashida G, Motoyama H, Fujii Y, Aoki S and Nakazawa T (2006) Convective mixing of air in firn at four polar sites. *Earth Planet. Sci. Lett.* **244**(3–4), 672–682 (doi:10.1016/j.epsl.2006.02.017)

Kobashi T, Severinghaus JP and Kawamura K (2008) Argon and nitrogen isotopes of trapped air in the GISP2 ice core during the Holocene epoch (0–11,500 B.P.): Methodology and implications for gas loss processes. *Geochim. Cosmochim. Acta* **72**(19), 4675–4686 (doi:10.1016/j.gca.2008.07.006)

Krabill WB, Abdalati W, Frederick EB, Manizade SS, Martin CF, Sonntag JG, Swift RN, Thomas RH and Yungel JG (2002) Aircraft laser altimetry measurement of elevation changes of the greenland ice sheet: Technique and accuracy assessment. *J. Geodyn.* **34**(3–4), 357–376 (doi:10.1016/S0264-3707(02)00040-6)

Kuipers Munneke P, Ligtenberg SRM, Van Den Broeke MR, Van Angelen JH and Forster RR (2014) Explaining the presence of perennial liquid water bodies in the firn of the Greenland Ice Sheet. *Geophys. Res. Lett.* **41**(2), 476–483 (doi:10.1002/2013GL058389)

Kuipers Munneke P, Ligtenberg SRM, Noël BPY, Howat IM, Box JE, Mosley-Thompson E, McConnell JR, Steffen K, Harper JT, Das SB and van den Broeke MR (2015) Elevation change of the Greenland Ice Sheet due to surface mass balance and firn processes, 1960–2014. *Cryosphere* **9**(6), 2009–2025 (doi:10.5194/tc-9-2009-2015)

Kuipers Munneke P, Ligtenberg SRM, Suder EA and Van Den Broeke MR (2015) A model study of the response of dry and wet firn to climate change. *Ann. Glaciol.* **56**(70), 1–8 (doi:10.3189/2015AoG70A994)

De La Peña S, Howat IM, Nienow PW, Van Den Broeke MR, Mosley-Thompson E, Price SF, Mair D, Noël B and Sole AJ (2015) Changes in the firn structure of the western Greenland Ice Sheet caused by recent warming. *Cryosphere* **9**(3), 1203–1211 (doi:10.5194/tc-9-1203-2015)

Landais A, Barnola JM, Kawamura K, Caillon N, Delmotte M, Van Ommen T, Dreyfus G, Jouzel J, Masson-Delmotte V, Minster B, Freitag J, Leuenberger M, Schwander J, Huber C, Etheridge D and Morgan V (2006) Firn-air δ15N in modern polar sites and glacial-interglacial ice: A model-data mismatch during glacial periods in Antarctica? *Quat. Sci. Rev.* **25**(1–2), 49–62 (doi:10.1016/j.quascirev.2005.06.007)

Langen PL, Fausto RS, Vandecrux B, Mottram RH and Box JE (2017) Liquid Water Flow and Retention on the Greenland Ice Sheet in the Regional Climate Model HIRHAM5: Local and Large-Scale Impacts. *Front. Earth Sci.* **4**(January), 110 (doi:10.3389/feart.2016.00110)

Li J and Zwally HJ (2002) Modeled seasonal variations of firn density induced by steady-state surface air-temperature cycle. *Ann. Glaciol.* **34**(1), 299–302 (doi:10.3189/172756402781817707)

Li J and Zwally HJ (2004) Modeling the density variation in the shallow firn layer. *Ann. Glaciol.* **38**(1), 309–313 (doi:10.3189/172756404781814988)

Li J and Zwally HJ (2011) Modeling of firn compaction for estimating ice-sheet mass change from observed ice-sheet elevation change. *Ann. Glaciol.* **52**(59), 1–7 (doi:10.3189/172756411799096321)

Ligtenberg SRM, Helsen MM and van den Broeke MR (2011) An improved semi-empirical model for the densification of Antarctic firn. *Cryosph.* **5**(4), 809–819 (doi:10.5194/tc-5-809-2011)

Lilien DA, Fudge TJ, Koutnik MR, Conway H, Osterberg EC, Ferris DG, Waddington ED and Stevens CM (2018) Holocene Ice-Flow Speedup in the Vicinity of the South Pole. *Geophys. Res. Lett.* **45**(13), 6557–6565 (doi:10.1029/2018GL078253)

Linow S, Hörhold MW and Freitag J (2012) Grain-size evolution of polar firn: A new empirical grain growth parameterization based on X-ray microcomputer tomography measurements. *J. Glaciol.* **58**(212), 1245–1252 (doi:10.3189/2012JoG11J256)

Lomonaco R, Albert MR and Baker I (2011) Microstructural evolution of fine-grained layers

through the firn column at Summit, Greenland. *J. Glaciol.* **57**(204), 755–762 (doi:10.3189/002214311797409730)

Lucas-Picher P, Wulff-Nielsen M, Christensen JH, Aðalgeirsdóttir G, Mottram R and Simonsen SB (2012) Very high resolution regional climate model simulations over Greenland: Identifying added value. *J. Geophys. Res.* (doi:10.1029/2011JD016267)

Lundin JMD, Stevens CM, Arthern RJ, Buizert C, Orsi A, Ligtenberg SRM, Simonsen SB, Cummings E, Essery R, Leahy W, Harris P, Helsen MM and Waddington ED (2017) Firn Model Intercomparison Experiment (FirnMICE). *J. Glaciol.* **63**(239), 401–422 (doi:10.1017/jog.2016.114)

Machguth H, Macferrin M, Van As D, Box JE, Charalampidis C, Colgan W, Fausto RS, Meijer HAJ, Mosley-Thompson E and Van De Wal RSW (2016) Greenland meltwater storage in firn limited by near-surface ice formation. *Nat. Clim. Chang.* **6**(4), 390–393 (doi:10.1038/nclimate2899)

Maeno N and Ebinuma T (1983) Pressure sintering of ice and its implication to the densification of snow at polar glaciers and ice sheets. *J. Phys. Chem.* **87**(21), 4103–4110 (doi:10.1021/j100244a023)

Marsh P and Woo M -K (1984) Wetting front advance and freezing of meltwater within a snow cover: 1. Observations in the Canadian Arctic. *Water Resour. Res.* **20**(12), 1853–1864 (doi:10.1029/WR020i012p01853)

Martinerie P, Raynaud D, Etheridge DM, Barnola JM and Mazaudier D (1992) Physical and climatic parameters which influence the air content in polar ice. *Earth Planet. Sci. Lett.* **112**(1–4), 1–13 (doi:10.1016/0012-821X(92)90002-D)

McMillan M, Leeson A, Shepherd A, Briggs K, Armitage TWK, Hogg A, Munneke PK, Broeke MVD, Noël B, Berg WJVD, Ligtenberg SRM, Horwath M, Groh A, Muir A and Gilbert L (2016) A high-resolution of Greenland mass balance. *Geophys. Res. Lett.* **43**, 7002–7010 (doi:10.1002/2016GL069666.Received)

Meese DA (1999) GISP2 Meese/Sowers Timescale. (doi:10.1594/PANGAEA.56083)

Mernild SH, Mote TL and Liston GE (2011) Greenland ice sheet surface melt extent and trends: 1960-2010. *J. Glaciol.* **57**(204), 621–628 (doi:10.3189/002214311797409712)

Mitchell LE, Buizert C, Brook EJ, Breton DJ, Fegyveresi J, Baggenstos D, Orsi A, Severinghaus J, Alley RB, Albert M, Rhodes RH, McConnell JR, Sigl M, Maselli O, Gregory S and Ahn J (2015) Observing and modeling the influence of layering on bubble trapping in polar firn. *J. Geophys. Res.* **120**(6), 2558–2574 (doi:10.1002/2014JD022766)

Morris EM and Wingham DJ (2014) Densification of polar snow: Measurements, modeling, and implications for altimetry. *J. Geophys. Res. Earth Surf.* **119**(2), 349–365 (doi:10.1002/2013JF002898)

Nghiem S V., Hall DK, Mote TL, Tedesco M, Albert MR, Keegan K, Shuman CA, DiGirolamo NE and Neumann G (2012) The extreme melt across the Greenland ice sheet in 2012. *Geophys. Res. Lett.* **39**(20), 6–11 (doi:10.1029/2012GL053611)

Noël B, Van De Berg WJ, Van Meijgaard E, Kuipers Munneke P, Van De Wal RSW and Van Den Broeke MR (2015) Evaluation of the updated regional climate model RACMO2.3: Summer snowfall impact on the Greenland Ice Sheet. *Cryosphere* **9**(5), 1831–1844 (doi:10.5194/tc-9-1831-2015)

Noël B, Van De Berg WJ, Van Wessem JM, Van Meijgaard E, Van As Di, Lenaerts JTM, Lhermitte S, Munneke PK, Smeets CJPP, Van Ulft LH, Van De Wal RSW and Van Den Broeke MR (2018) Modelling the climate and surface mass balance of polar ice sheets using RACMO2 - Part 1: Greenland (1958-2016). *Cryosphere* **12**(3), 811–831 (doi:10.5194/tc-12-811-2018)

Petrenko VF and Whitworth RW (1999) *Physics of Ice.* Oxford University Press, New York

Pfeffer WT and Humphrey NF (1996) Determination of timing and location of water movement and ice layer formation by temperature measurements in sub freezing snow. *J. Glaciol.* **42**(141), 292–305

Proksch M, Löwe H and Schneebeli M (2015) Density, specific surface area, and correlation length of snow measured by high-resolution penetrometry. *J. Geophys. Res. Earth Surf.* **120**(2), 346–362 (doi:10.1002/2014JF003266)

Rasmussen SO, Abbott PM, Blunier T, Bourne a. J, Brook E, Buchardt SL, Buizert C, Chappellaz J, Clausen HB, Cook E, Dahl-Jensen D, Davies SM, Guillevic M, Kipfstuhl S, Laepple T, Seierstad IK, Severinghaus JP, Steffensen JP, Stowasser C, Svensson a., Vallelonga P, Vinther BM, Wilhelms F and Winstrup M (2013) A first chronology for the north greenland eemian ice drilling (NEEM) ice core. *Clim. Past* **9**(6), 2713–2730 (doi:10.5194/cp-9-2713-2013)

Rasmussen SO, Bigler M, Blockley SP, Blunier T, Buchardt SL, Clausen HB, Cvijanovic I, Dahl-Jensen D, Johnsen SJ, Fischer H, Gkinis V, Guillevic M, Hoek WZ, Lowe JJ, Pedro JB, Popp T, Seierstad IK, Steffensen JP, Svensson AM, Vallelonga P, Vinther BM, Walker MJC, Wheatley JJ and Winstrup M (2014) A stratigraphic framework for abrupt climatic changes during the Last Glacial period based on three synchronized Greenland ice-core records: Refining and extending the INTIMATE event stratigraphy. *Quat. Sci. Rev.* **106**, 14–28 (doi:10.1016/j.quascirev.2014.09.007)

Reeh N (2008) A nonsteady-state firn-densification model for the percolation zone of a glacier. *J. Geophys. Res.* **113**(F3), F03023 (doi:10.1029/2007JF000746)

Scapozza C and Bartelt PA (2003) The influence of temperature on the small-strain viscous deformation mechanics of snow: A comparison with polycrystalline ice. *Ann. Glaciol.* **37**, 90–96 (doi:10.3189/172756403781815410)

Schaller CF, Freitag J and Eisen O (2017) Critical porosity of gas enclosure in polar firn

independent of climate. *Clim. Past* **13**(11), 1685–1693 (doi:10.5194/cp-13-1685-2017)

Schwander J, Sowers T, Barnola J-M, Blunier T, Fuchs A and Malaizé B (1997) Age scale of the air in the summit ice: Implication for glacial-interglacial temperature change. *J. Geophys. Res. Atmos.* **102**(D16), 19483–19493 (doi:10.1029/97JD01309)

Schwander J, Stauffer B and Sigg A (1988) Air mixing in firn and the age of the air at pore close-off. *Ann. Glaciol.* **10**, 141–145 (doi:10.1017/S0260305500004328)

Seierstad IK, Abbott PM, Bigler M, Blunier T, Bourne AJ, Brook E, Buchardt SL, Buizert C, Clausen HB, Cook E, Dahl-Jensen D, Davies SM, Guillevic M, Johnsen SJ, Pedersen DS, Popp TJ, Rasmussen SO, Severinghaus JP, Svensson A and Vinther BM (2014) Consistently dated records from the Greenland GRIP, GISP2 and NGRIP ice cores for the past 104ka reveal regional millennial-scale δ18O gradients with possible Heinrich event imprint. *Quat. Sci. Rev.* **106**, 29–46 (doi:10.1016/j.quascirev.2014.10.032)

Severinghaus JP and Battle MO (2006) Fractionation of gases in polar ice during bubble close-off: New constraints from firn air Ne, Kr and Xe observations. *Earth Planet. Sci. Lett.* **244**(1–2), 474–500 (doi:10.1016/j.epsl.2006.01.032)

Severinghaus JP and Brook EJ (1999) Abrupt climate change at the end of the last glacial period inferred from trapped air in polar ice. *Science (80-.).* **286**(5441), 930–934 (doi:10.1126/science.286.5441.930)

Severinghaus JP, Grachev AM and Battle MO (2001) Thermal fractionation of air in polar firn by seasonal temperature gradients. *Geochemistry, Geophys. Geosystems* **2** http://onlinelibrary.wiley.com/doi/10.1029/2000GC000146/full

Severinghaus JP, Sowers T, Brook EJ, Alley RB and Bender ML (1998) Timing of abrupt climate change at the end of the younger dryas interval from thermally fractionated gases in polar ice. *Nature* **391**(6663), 141–146 (doi:10.1038/34346)

Shepherd A, Ivins ER, A G, Barletta VR, Bentley MJ, Bettadpur S, Briggs KH, Bromwich DH, Forsberg R, Galin N, Horwath M, Jacobs S, Joughin I, King MA, Lenaerts JTM, Li J, Ligtenberg SRM, Luckman A, Luthcke SB, McMillan M, Meister R, Milne G, Mouginot J, Muir A, Nicolas JP, Paden J, Payne AJ, Pritchard H, Rignot E, Rott H, Sorensen LS, Scambos TA, Scheuchl B, Schrama EJO, Smith B, Sundal A V., van Angelen JH, van de Berg WJ, van den Broeke MR, Vaughan DG, Velicogna I, Wahr J, Whitehouse PL, Wingham DJ, Yi D, Young DA and Zwally HJ (2012) A Reconciled Estimate of Ice-Sheet Mass Balance. *Science (80-.).* **338**(6111), 1183–1189 (doi:10.1126/science.1228102)

Shepherd A, Ivins E, Rignot E, Smith B, Van Den Broeke M, Velicogna I, Whitehouse P, Briggs K, Joughin I, Krinner G, Nowicki S, Payne T, Scambos T, Schlegel N, Geruo A, Agosta C, Ahlstrøm A, Babonis G, Barletta V, Blazquez A, Bonin J, Csatho B, Cullather R, Felikson D, Fettweis X, Forsberg R, Gallee H, Gardner A, Gilbert L, Groh A, Gunter B, Hanna E, Harig C, Helm V, Horvath A, Horwath M, Khan S, Kjeldsen KK, Konrad H, Langen P, Lecavalier B, Loomis B, Luthcke S, McMillan M, Melini D, Mernild S, Mohajerani Y, Moore P, Mouginot J, Moyano G, Muir A, Nagler T, Nield G, Nilsson J, Noel B, Otosaka I,

Pattle ME, Peltier WR, Pie N, Rietbroek R, Rott H, Sandberg-Sørensen L, Sasgen I, Save H, Scheuchl B, Schrama E, Schröder L, Seo KW, Simonsen S, Slater T, Spada G, Sutterley T, Talpe M, Tarasov L, Van De Berg WJ, Van Der Wal W, Van Wessem M, Vishwakarma BD, Wiese D and Wouters B (2018) Mass balance of the Antarctic Ice Sheet from 1992 to 2017. *Nature* **558**(7709), 219–222 (doi:10.1038/s41586-018-0179-y)

Simonsen SB, Stenseng L, Adalgeirsdóttir G, Fausto RS, Hvidberg CS and Lucas-Picher P (2013) Assessing a multilayered dynamic firn-compaction model for Greenland with ASIRAS radar measurements. *J. Glaciol.* **59**(215), 545–558 (doi:10.3189/2013JoG12J158)

Sommers AN, Rajaram H, Weber EP, MacFerrin MJ, Colgan WT and Stevens CM (2017) Inferring Firn Permeability from Pneumatic Testing: A Case Study on the Greenland Ice Sheet. *Front. Earth Sci.* **5**(March), 1–12 (doi:10.3389/feart.2017.00020)

Sorge E (1935) Glaziologische Untersuchungen in Eismitte. *Wissenschaftliche Ergebnisse der Deutschen Groenland-Expedition Alfred Wegener 1920 und 1930/1931, Bd. 3*. F.A. Brockhaus, Leipzig, 62–270

Steffen K and Box J (2001) Surface climatology of the Greenland Ice Sheet: Greenland Climate Network 1995-1999. *J. Geophys. Res. Atmos.* **106**(D24), 33951–33964 (doi:10.1029/2001JD900161)

Steger CR, Reijmer CH, van den Broeke MR, Wever N, Forster RR, Koenig LS, Kuipers Munneke P, Lehning M, Lhermitte S, Ligtenberg SRM, Miège C and Noël BPY (2017) Firn Meltwater Retention on the Greenland Ice Sheet: A Model Comparison. *Front. Earth Sci.* **5**(January), 3 (doi:10.3389/feart.2017.00003)

Stocker TF, Dahe Q, Plattner G-K, Alexander L V., Allen SK, Bindoff NL, Bréon F-M, Church JA, Cubash U, Emori S, Forster P, Friedlingstein P, Talley LD, Vaughan DG and Xie S-P (2013) Technical Summary. *Clim. Chang. 2013 Phys. Sci. Basis. Contrib. Work. Gr. I to Fifth Assess. Rep. Intergov. Panel Clim. Chang.*, 33–115 (doi:10.1017/CBO9781107415324.005)

Tange O (2011) GNU Parallel: the command-line power tool. *;login USENIX Mag.* **36**(1), 42–47 (doi:10.5281/zenodo.16303)

Thompson DC (1969) The coreless winter at Scott Base, Antarctica. *Q. J. R. Meteorol. Soc.* **95**(404), 404–407 (doi:10.1002/qj.49709540413)

Trudinger CM, Enting IG, Etheridge DM, Francey RJ, Levchenco VA and Steele LP (1997) Modeling air movement and bubble trapping in firn. *J. Geophys. Res.* **102**(96), 6747–6763 http://onlinelibrary.wiley.com/doi/10.1029/96JD03382/full

Vaughan DG, Comiso JC, Allison I, Carrasco J, Kaser G, Kwok R, Mote P, Murray T, Paul F, Ren J, Rignot E, Solomina O, Steffen K and Zhang T (2013) Observations: Cryosphere. *Clim. Chang. 2013 Phys. Sci. Basis. Contrib. Work. Gr. I to Fifth Assess. Rep. Intergov. Panel Clim. Chang.*, 317–382 (doi:10.1017/CBO9781107415324.012)

Vernon CL, Bamber JL, Box JE, van den Broeke MR, Fettweis X, Hanna E and Huybrechts P (2013) Surface mass balance model intercomparison for the Greenland ice sheet. *Cryosph.* **7**(2), 599–614 (doi:10.5194/tc-7-599-2013)

Vionnet V, Brun E, Morin S, Boone A, Faroux S, Le Moigne P, Martin E and Willemet JM (2012) The detailed snowpack scheme Crocus and its implementation in SURFEX v7.2. *Geosci. Model Dev.* **5**(3), 773–791 (doi:10.5194/gmd-5-773-2012)

Voller VR, Cross M and Markatos NC (1987) An enthalpy method for convection/diffusion phase change. *Int. J. Numer. Methods Eng.* (doi:10.1002/nme.1620240119)

Wever N, Fierz C, Mitterer C, Hirashima H and Lehning M (2014) Solving Richards Equation for snow improves snowpack meltwater runoff estimations in detailed multi-layer snowpack model. *Cryosphere* **8**(1), 257–274 (doi:10.5194/tc-8-257-2014)

Wever N, Würzer S, Fierz C and Lehning M (2016) Simulating ice layer formation under the presence of preferential flow in layered snowpacks. *Cryosphere* **10**(6), 2731–2744 (doi:10.5194/tc-10-2731-2016)

Wilkinson D (1988) A pressure-sintering model for the densification of polar firn and glacier ice. *J. Glaciol.* **34**(116), 40–45 http://www.igsoc.org:8080/journal/34/116/igs_journal_vol34_issue116_pg40-45.pdf

Witrant E, Martinerie P, Hogan C, Laube JC, Kawamura K, Capron E, Montzka SA, Dlugokencky EJ, Etheridge D, Blunier T and Sturges WT (2012) A new multi-gas constrained model of trace gas non-homogeneous transport in firn: Evaluation and behaviour at eleven polar sites. *Atmos. Chem. Phys.* **12**(23), 11465–11483 (doi:10.5194/acp-12-11465-2012)

Zwally HJ and Li J (2002) Seasonal and interannual variations of firn densification and ice-sheet surface elevation at the Greenland summit. *J. Glaciol.* **48**(161), 199–207 (doi:10.3189/172756502781831403)

APPENDIX A: THE COMMUNITY FIRN MODEL

The Community Firn Model (CFM) is a modular firn-evolution model framework. Its most basic function is to predict the depth/density and depth/age profiles of firn (i.e. functioning as a firn-densification model), but it also includes modules to simulate heat transfer, meltwater percolation and refreezing, water isotope diffusion, firn-air diffusion and advection, and grain growth.

The modular nature of the CFM means that the user can easily choose to run the model using a firn-densification equation from any of a suite of published firn-densification equations (Table A1). The user can also choose which of the optional physics modules (e.g. grain growth) to include with the model run. The model is designed so that different firn-densification equations or modules simulating different physics can be easily integrated into the model.

The CFM is one dimensional and uses a Lagrangian (material-following) grid. The evolution of the density is calculated explicitly (e.g. $\rho_{new} = \rho_{old} + \frac{d\rho}{dt} * dt$). Heat and other (e.g. water isotope, firn air, enthalpy) diffusion is solved using a fully-implicit finite-volume method (Patankar, 1980).

The CFM is coded in Python 3 and can be run on Windows, Linux, and OSX platforms. In addition to the packages included in the Python standard library, the model requires the numpy, scipy, and h5py Python packages to be installed. Additionally, plotting CFM results using Python requires the matplotlib package. Installing Python 3 and the necessary packages is most easily done using a packaged Python distribution such as Anaconda or Enthought Canopy. Explicit instructions on a scientific Python installation are beyond the scope of this document, but tutorials can be readily found online.

A1.1 Running the CFM

The CFM is mostly easily run from the command line, though it can alternatively be run from an integrated development environment (IDE) such as Spyder (included with the Anaconda Python distribution). To run the model, the user must set up a .json-formatted configuration file that specifies the settings for a particular model run. Here, we generically use *config.json* as the name of that configuration file.

The model is run by calling *main.py* and specifying the name of the configuration file:

>>> python main.py config.json -n

If the results folder (specified in config.json) already exists and contains the results of a spin-up run (the spin-up file name is typically *CFMspin.hdf5*), the model will not run the spin-up routine again. If the user wishes to include the spin-up run, he/she should add the –n at the end of the above command to force the spin-up to run; if he/she wished to omit the spin up run, the –n should be omitted.

A1.2 Model Inputs

The CFM is forced by surface-temperature and accumulation-rate boundary conditions. Additionally, the user can specify the surface-melt, surface-density and water-isotope values. These files are .csv formatted. The first row of these files is time (decimal date, i.e. 2015.3487) and the second row is the corresponding temperature/accumulation rate/boundary condition value at that time. Time must be going forward, i.e. the first column is a date some time ago and the last column is the most recent. (If the model is being forced with ice-core data, the user must be careful to ensure this is the case as ice-core data are often presented as years before present.) The times in the various input files do not need to be the same; they are interpolated onto a common axis. The units for temperature can be K or C. The CFM uses K, but it will change the temperature to K if

you use C. The units for accumulation rate/surface mass balance are m ice equivalent per year (see note in Appendix A1.3)

A1.3 The .json configuration file

JSON (JavaScript Object Notation) is a data-interchange file format. It consists of a number of names, each associated with a value. Values can be strings, Booleans, integers, floats, or arrays. Comments are not allowed but can be added by considering the comment as a name/value pair. For the CFM, it provides a file format that is both easy to read and easy to alter in order to specify parameters for a particular model run. The configuration file is passed to the CFM, and the name/value pairs are read by the model and incorporated into the model run. The file format is editable in any text editor, and the name/value pairs are given by *name: value*, and different name/value pairs are separated by commas:

```
{
“Name1”: “string”,
“Name2”: true,
“Name3”: 3,
“Name4”: 6.7,
“Name5”: [“one”, “two”, “three”],
“Comment”: “Name5 is an array of three strings”,
}
```

The specific names that are in the configuration .json file for the CFM are as follows. If any of the name/value pairs are missing, the model will generally give an error and the model run will not complete. Note that in the .json file true/false are lowercase, but in the .py files they are True/False (first letter capitalized). The model automatically converts this.

"InputFileFolder": *string.* directory where the input csv files are located (usually a subdirectory of the directory that contains main.py. If not, the user must change code in firn_density_spin.py). Use "" if the input files are in the same directory as main.py.

"InputFileNameTemp": *string.* Name of the temperature input file, which is a .csv file (see section 5.2).

"InputFileNamebdot": Name of the accumulation-rate input file. It is a .csv. Units are m ice equivalent *per year*, not for that particular time step. So, if you are using monthly time steps, perhaps it snows 0.05 m (ice) in January 2015. That column of the csv would be:

2015.0
0.6

Because annual rate would be $0.05 \times 12 = 0.6$ m i.e. a^{-1}.

"InputFileNameIso": Same as input bdot and temp, except the time history of isotope values (per mil) at the surface.

"InputFileNamerho": Time series of the surface density. The units are kg m^{-3}.

"InputFileNamemelt": Time series of the melt. Units are m per year ice equivalent (same as accumulation rate)

"resultsFolder": folder that will be created and where results will be stored.

"physRho": The physics that will be used for the model run.

"_physRhoOptions": A list of all the physics that are available to run. This is a effectively a comment in the code. The list is currently (August 2018):

"HLdynamic","HLSigfus","Li2004","Li2011","Helsen2008","Arthern2010S","Arthern2010T","Spencer2001","Goujon2003","Barnola1991","Morris2013","KuipersMunneke2015","Crocus"

"MELT": true/false; whether or not to run melt physics.

"FirnAir": true/false; whether or not to run firn air physics (i.e. the gas model)

"AirConfigName": Name of the .json file that is the configuration file for the gas model, e.g. FirnAir.json. If 'FirnAir' is true, the CFM will open this file and use its values for the firn-air model run.

"TWriteInt": Time write interval – how often to save model output. 1 saves every time step; 2 saves every other time step, 3 saves every 3rd, etc. This is a clunky part of the model that will be improved in the future. The time steps at which writing occurs should be changed by changing the variable "TWrite" in the file firn_density_nospin.py.

"SeasonalTcycle": true/false; whether to implement the seasonal temperature cycle. The details of this feature should be checked in firn_density_nospin.py. It includes a formulation for a coreless winter (Thompson, 1969).

"TAmp": Amplitude of the seasonal temperature cycle, if that option is used (Kelvin).

"physGrain": true/false; whether or not to track grain size.

"calcGrainSize": true/false (physGrain must be true as well for this to be true); true uses a parameterization to get a surface value and false uses a set grain size at the surface. It is not clear where the current parameterization (which is temperature-based) comes from (code was written by a previous research group member and no documentation exists); therefore it is currently not recommended to use this option. The default initial grain size is 0.1 mm if 'calcGrainSize' is false.

"**heatDiff":** true/false; whether to run heat diffusion.

"variable_srho": true/false; variable surface density (true) or not.

"srho_type": There are different options for the surface density if variable_srho is true. "userinput" loads the csv file specified by InputFileNamerho. "param" uses a parameterization for surface density from Kuipers Munneke and others (2015). "noise" creates a random time

series of surface density. Each value is drawn from a normal distribution with mean “rhos0” and standard deviation of 25 kg m^{-3}. This value can be changed in the file firn_density_nospin.py

"_srho_type_options": The options for “srho_type”. See above.

"rhos0": surface density if variable_srho is false or if “srho_type” is ‘noise’.

"r2s0": initial condition for grain size; used only in firn_density_spin.

"AutoSpinUpTime": true/false. If true, model will attempt to spin up the model for as long as it takes to refresh the entire firn column to the depth where density is 850 kg m^{-3}. Use caution if you need the spin up to refresh the firn column to the full depth.

"yearSpin": how many years to spin up for. Does not do anything if ‘AutoSpinUpTime’

"stpsPerYearSpin": how many time steps per year during the spin up (e.g. 12 is monthly)

"H": Thickness of the ice sheet in meters. This is a bit confusing. Probably keep it at 3000 or so. That would mean the surface of the firn is 3000 m above the bed.

"HbaseSpin": The elevation of the bottom of the model domain above the bed (confusing bit part 2!). So, if you want to model to 250 m depth, and H is 3000, HbaseSpin will be 2750. Likewise, if you wanted to model just the top 50 m of firn, HbaseSpin will be 2950 (assuming H is 3000). This is an initial value at the start of the spin up. The base of the model domain will change due to the fact the model is Lagrangian with a fixed number of nodes; e.g. if the accumulation rate increases, each node will be thicker, and the base of the domain will be deeper.

"stpsPerYear": steps per year for the model run (it probably should always just be the same as stpsPerYearSpin).

"D_surf": The surface boundary value of the layer tracking routine. Default is 0.

"bdot_type": The type of accumulation rate to use for the densification physics. ‘Instant’ is the instantaneous value (i.e. at that time step) of accumulation, ‘mean’ is the mean accumulation over the lifetime of a parcel of firn. (‘Stress’ is in progress, 11/17/18, and will use the stress directly).

"bdot_options": ["instant","mean","stress"] See above.

"isoDiff": true/false; whether to run water isotope diffusion.

"iso": string. Which water isotope you are modeling. (Different isotopes have different diffusivities).

"_isoOptions": ["18","D","NoDiffusion"]; no diffusion means that the isotopes are tracked but do not diffuse (it is something of a baseline case).

"spacewriteint": interger. interval of the spatial nodes to write; 1 is every node; 2 is every other, etc.

"strain": true/false; whether to consider longitudinal strain

"du_dx": float. strain rate if “strain” is true; a value around 1e-5 is a good guess if you want to play. Currently (1/23/17) it is a fixed value, but a future release will allow variance with depth.

"outputs": which outputs you want the model to save, e.g.: ["density", "depth", "compaction ","DIP","BCO","temperature","LWC"]

"output_options": all of the options for outputs. ["density", "depth", "temperature", "age", "dcon", "bdot_mean", "climate", "compaction_rate", "grainsize", "temp_Hx", "isotopes", "BCO", "LIZ", "DIP", "LWC", "gasses"]

"resultsFileName": name of the results file; default: "CFMresults.hdf5",

"spinFileName": name of the spin-up results file; default: "CFMspin.hdf5"

"doublegrid": true/false; whether to use the regrid feature, which allows for a grid with varying resolution.

"nodestocombine": integer. How many nodes should be combined into a single node if using double grid.

"grid1bottom": Float. Depth (m) at which the model transitions from the high-resolution grid to the lower-resolution grid if doublegrid is used.

A1.4 Model outputs

The CFM writes its outputs to a single .hdf5-format file. By default, all nodes are written to file. The output is only saved at the time steps specified by the user with the variable TWrite. Most of the outputs should be self-explanatory. Many of them are big 2D matrices; the first column is time, and the values throughout are the particular values at the depth found in the corresponding cell in the depth output. Set the outputs you want in the .json file. The available outputs are:

depth: (m) The depth of each model node.

density: (kg m^{-3}) The density at the depths in 'depth

temperature: (K) Temperature at the depths in 'depth'

age: (years) Firn Age at the depths in 'depth'

dcon: Dcon is a layer-tracking routine; to use it you need to dig into the code a bit and program it how you want, but for example you could set it up so that each model node that has liquid water gets a 1 and all others get a zero. Corresponds to depth.

bdot_mean: (m a^{-1} ice equivalent) the mean accumulation rate over the lifetime of each parcel of firn, corresponds with 'depth'

climate: The temperature (K) and accumulation rate (m a^{-1} ice equivalent) at each time step – useful if using interpolation to find determine the climate.

compaction: (m) Total compaction of each node since the previous time step; corresponds to 'depth'. To get compaction rate you need to divide by the time-step size. To get compaction over an interval you need to sum numerous boxes.

grainsize: (mm^2) the grain size of the firn, corresponds to 'depth'

temp_Hx: the temperature history of the firn (See Morris and Wingham, 2014)

isotopes: (per mil) water isotope values, corresponds to 'depth'

LWC: (m^3) volume of liquid present in that node, corresponds to 'depth'

DIP: the depth-integrated porosity and change in surface elevation. 4 columns: The first is time, second is DIP to the bottom of the model domain (m), third is change in domain thickness since last time step (m), fourth is change in domain thickness since start of model run (m).

DIP also saves a variable called DIPc, which is a matrix of the cumulative porosity to the depth in 'depth'

BCO: bubble close-off properties. 10 columns: time, Martinerie close-off age, Marinerie close-off depth, age of 830 kg m^{-3} density horizon, depth of 830 kg m^{-3} density horizon, Martinerie lock-in age, Marinerie lock-in depth, age of 815 kg m^{-3} density horizon, depth of 815 kg m^{-3} density horizon, depth of zero porosity.

FirnAir: only works if FirnAir is true in the config.json. Saves gas concentrations, diffusivity profile, gas age, and advection rates of air and firn, all corresponding to 'depth'.

A1.5 Model files, modules, and model features.

main.py

This is the file that is (generally) called if you are running the CFM. It calls firn_density_spin and firn_density_nospin.

firn_density_spin.py

This 'spins up' the model to a steady state. It only uses a single value for temperature and accumulation rate at every time step (good for ice cores when you are doing a 40,000-year model run; bad for altimetry runs when the daily/monthly variability makes a difference for spin up. This module may be removed in future versions and integrated into firn_density_spin. It is set up as a class.

firn_density_nospin.py (class)

This is the file in which everything happens. It sets up the model grid and the initial and boundary conditions. Then it time steps through the model run, calling the different modules throughout. Set up as a class.

constants.py

All of the universal/global constants in one handy file. Hopefully all of the units are in there…

diffusion.py

As the name suggests, this file handles all of the diffusive processes: heat, enthalpy, and isotopes. It sets up the finite volumes and diffusivity and calls solver. All of these are set up as methods.

firn_air.py

Runs the firn-air module, including setting up boundary and intial conditions, handles the fir-air diffusion. This is a class.

hl_analytic.py

An implementation of the Herron and Langway analytic solution. Method.

melt.py

Functions defining the physics of the meltwater percolation, keeping track of how much liquid water there is and where it goes.

physics.py

Included all of the different densification physics (e.g. Herron and Langway, Ligtenberg, etc.) and also the grain-growth physics. This would also be an appropriate place to put other physics, such as evolution of microstructural properties. Set up as a class, though I am not sure that is the best way of doing this.

reader.py

Functions that read in the input files and the results from the spin up.

regrid.py

In order to run daily (or some high-resolution) time steps, it becomes prohibitively expensive due to the fact that the model domain gets a new box for each time step (that is, the grid spacing is dependent on the time step size). The regrid.py module solves this by re-gridding the model domain below a user-specified depth. **Use caution with this module! I think that it is more or less correct; however, it does not work with monthly (or larger) time steps. I have not yet sorted out at what time-step size it breaks down. Also: the way that liquid water is handled will remove any ice lenses that are present when nodes are combined (it conserves mass, so firn + ice = denser firn). So, ensure that the depth of grid 1 to grid 2 transition is adequately deep that you do not expect water to percolate that deep.**

The fields in the .json file need to be updated; there are three of them:

Regrid is true/false; it specifies that the regridding routine should be implemented. **grid1bottom** is the depth where you want to transition between the high and lower resolution

grid. “Grid 1” is the upper, high-resolution grid, and “grid 2” is the deeper, lower resolution grid. **Nodestocombine** is the number of volumes that get combined into one single volume from the bottom of grid 1. Call this n for the rest of the document.

The regrid module retains the Lagrangian grid. Layers are tracked as being in grid 1, 2, or 3. Grid 3 is the very bottom, where the last volume will be split up into high-resoution layers (each keeping the properties of the previous, large volume that was split up).

During spin-up, the model initializes with a full high-resolution grid, but then takes all volumes below ‘grid1bottom’ and combines every ‘nodestocombine’ nodes into a single node. This is all using just z and dz – there is no need to change density and age at this point. Each node is assigned a value of 1, 2, or 3 based on which grid portion it is in, which is tracked in the variable ‘gridtrack’.

When time stepping begins, the layers are advected downward as usual. A layer is added on top at each time step, and one is taken away from the bottom. So, for some number of time steps (n) the index of the first layer in grid 2 is increasing, and the number of layers in grid 3 is decreasing. Once all of the grid 3 layers are gone (n time steps have passed), it is time to regrid. The last n layers from grid 1 are combined into one single layer, which becomes the new top of grid 2. Since n layers have been consolidated into one (n to 1), the very last layer (which is the last layer of grid 2) is split into n layers (1 to n). The upshot is that the number of volumes stays constant. The updated grid is made by concatenating the remaining grid 1 layers, the new consolidated layer, the remaining grid 2 layers, and the new split-into-n layers.

The ‘grid1bottom’ does not actually end up being the depth bottom of grid 1, but it does reach a steady state that is deeper than the user-specified depth. The reason has to do with the thickness of the layers at the bottom that are being removed versus the thickness of the layers

that are being added. Once the regridding is initialized in the spin up, the model does not consider the user-specified depth; it only considers the number of layers being consolidated. It does make sense that if you are adding a thick layer and removing a thin layer, the depth of the grid1-grid2 transition is going to go downward. So, a to-do is to perhaps figure out how to better predict where the 1-2 transition will occur once a steady state is reached. One thing to think about is how thick you want the lower-resolution layers to be. If you are taking daily time steps and your annual accumulation is ~0.2 m i.e., the high resolution layers will be ~5.5e-4 m i.e. thick. If you combine 30 layers, those layers will be something like 0.016 m i.e. thick.

solver.py

This script solves the diffusion equation. It is based on Patankar (1980).

writer.py

This script writes the model output to an output file in hdf5 format. It is formatted to write just the outputs that are specified in the configuration (.json) file. Writer.py also writes the results of the model spin up.

A1.6 Model hosting/access

The CFM is on github: https://github.com/UWGlaciology/CommunityFirnModel

A1.7 Parallelization

The CFM is not very parallelizable because processes happen in a time-stepping loop, and there are not many things to solve within the time-stepping loop. I have extensively used GNU Parallel (Tange, 2011) to batch model runs; i.e. I set up a script that takes different arguments and calls the CFM. GNU parallel will leverage all of your cores to run those different model runs simultaneously.

APPENDIX B: DERIVING THE FIRN-DENSIFICATION MODEL PRESENTED IN CHAPTER 4

To find the parameters for Equation 4.1 and 4.2, we considered the hole shortening measured in the four 2015 boreholes at Summit as well as the shortening of the 'virtual' holes found by differencing the compaction of neighboring holes of different lengths. We convert these measurements to strain and resample them to 2-week intervals. We take the time derivative to find the strain rate, giving us strain rate measurements for each 2-week period. We find the stress from the depth-density data, and we assume that the stress does not change significantly through our period of measurement: the annual accumulation rate at Summit is ~200 kg m^{-2} a^{-1}, or about 2% of the mass of the 16-m firn column. For each 2-week period we take the mean temperature for each borehole from the RTD data. We did not date the FirnCover cores, so we use a depth-age relationship from the Herron and Langway (1980) analytic model to estimate the age of the firn.

Recognizing that $\dot{\epsilon} = -\frac{1}{\rho}\frac{D\rho}{Dt}$, we can find values for *k* and *Q* in Equation 4.2. With two free parameters, the problem is poorly constrained. We iterated through possible values of *Q* ranging from 20 kJ mol^{-1} to 100 kJ mol^{-1} in increments of 10 kJ mol^{-1}. For each value of *Q*, we find *k* that minimizes the RMS deviation of the predicted strain from the observed strain rate for each observation. We choose *k* from the center of the distribution of the best-fit values of *k*.

For each *Q*-*k* pair, we ran the CFM at Summit with the RACMO forcing data and compared the modeled compaction-rate time series to the observations. Though the modeled rates did not necessarily fit the timing of seasonal compaction, we used the magnitude of modeled seasonal cycle to choose the best *Q*. Using Q = 20 kJ mol^{-1} gave nearly no seasonal cycle in compaction rate, whereas using Q=100 kJ mol^{-1} produced a seasonal cycle of much

greater magnitude than observed. For Summit, our best fit was achieved with Q = 70 kJ mol^{-1}, and the corresponding k was $8.5x10^{9}$ Pa^{-1}.

VITA

Christopher (Max) Stevens is a post-doctoral researcher at the University of Washington.